1-1-2012

Interferometric, Astrometric, and Photometric Studies of Epsilon Aurigae: Seeing the Disk Around a Distant Star

Brian Keith Kloppenborg
University of Denver

INTERFEROMETRIC, ASTROMETRIC, AND PHOTOMETRIC STUDIES OF EPSILON AURIGAE: SEEING THE DISK AROUND A DISTANT STAR.

A Dissertation

Presented to

the Faculty of Natural Sciences and Mathematics

University of Denver

---

in Partial Fulfillment

of the Requirements for the Degree

of Doctor of Philosophy

---

by

Brian Kloppenborg

June, 2012

Advisor: Dr. Robert E. Stencel

Author: Brian Kloppenborg
Title: INTERFEROMETRIC, ASTROMETRIC, AND PHOTOMETRIC STUDIES OF EPSILON AURIGAE: SEEING THE DISK AROUND A DISTANT STAR.
Advisor: Dr. Robert E. Stencel
Degree Date: June, 2012

Abstract

Epsilon (ϵ) Aurigae is a binary star system that has baffled astronomers for 170 years. In 1821 it was first noticed that the star system had dimmed by nearly 50%. After many decades of photometric monitoring, the 27.1 year period was finally established in 1903. A few years later, in 1912, Henry Norris Russell published the first analytic methods for binary star analysis. Later application of these formulae came to an interesting conclusion; the system was composed of two stars: the visible F-type supergiant, and an equally massive, but yet photometrically and spectroscopically invisible, companion.

Several theories were advanced to explain this low-light to high-mass conundrum, eventually settling on the notion that the companion object is obscured from view by a disk of opaque material. With this topic solved, the debate shifted the evolutionary state of the system. Two scenarios became dominant: the system is either relativity young, and composed of a massive, 15 $M_\odot$ (solar mass), F-type supergiant and a nearly equally massive main sequence companion inside of the disk; or a much older and significantly less massive, 4 $M_\odot$, F-type post-asymptotic giant branch object with a more massive, 6 $M_\odot$, companion surrounded by a debris disk.

In this dissertation I disentangle the two evolutionary states by comparing the photometric behavior of the F-type star to known supergiant and post-asymptotic giant branch objects; and deriving a dynamical mass for the two components using astrometric, radial velocity, and interferometric data. Along with this, I provide the first interferometric images during the eclipse which prove the 50% dimming is indeed caused by an opaque disk.

The first chapter presents the reader with the status quo of ϵ Aurigae research and the topics I wish to address in this dissertation. Chapter two presents an analysis of nearly 30 years of photometry on the system, concluding the star periodically exhibits stable pulsation on 1/3 orbital timescales. The next two chapters are complementary in many ways. Chapter three presents the first interferometric images of ϵ Aurigae during eclipse and models the star and eclipsing body in unprecedented detail. Chapter four presents new combined astrometric and radial velocity orbital solutions using a myriad of historical data sources and modern analysis techniques. Lastly in Chapter five I conclude that the system is in the high-mass evolutionary state and provide estimates of the system component masses and distance.

Acknowledgements

A document such as this could not have been completed without considerable support from others. I would like to express my deepest gratitude to my advisor, Robert Stencel. His expertise and breadth of knowledge have significantly strengthened my understanding of astrophysics. I also find his dedicated work with local astronomy clubs, amateur astronomers, and astronomical preservation efforts truly inspirational and something which I wish to emulate in my own career

This work has benefited from discussions with Gail Schaefer, Fabien Baron, Paul Hemenway, and William Mitchell. Their guidance and thoughtful comments were much appreciated. I am also grateful for the participants in Citizen Sky, whose inquiries hastened my deep understanding of epsilon Auriage.

I am grateful for access to Georgia State University's Center for High Angular Resolution Astronomy (CHARA) on Mount Wilson, CA and the Sproul Observatory archives. I also wish commend Jeffrey Hopkins and Louis Boyd for their long-term photometric monitoring projects. Without data from these four sources, none of the research contained herein would have been possible.

While completing my dissertation I was fortunate to have my efforts supported in part by the bequest of William Herschel Womble in support of astronomy at the University of Denver and the National Science Foundation through ISE grant DRL-0840188 to the American Association of Variable Star Observers and AST grant 10-16678 to the University of Denver.

Much of my work would not have been possible without access to free and open source software including: Linux, gcc, Python, gnuPlot, LaTeX, Valgrind and many others. This research has benefited significantly from access to databases and digital libraries including SIMBAD, ADS, and ArXiV.

Finally, I would like to thank my family and friends –in particular my wife, Jessica– for their continued support throughout my graduate career.

Contents

List of Tables

List of Figures

Chapter 1

Introduction

The topic of this dissertation is to investigate the nature of the classic eclipsing binary, epsilon (ϵ) Aurigae. In this chapter a brief history of the system will be presented, culminating in the realization that the system can only be in one of two, mutually exclusive, evolutionary states. The remainder of this chapter discusses the three principal issues I address in this work and outlines the methods which I apply to disentangle the mystery of ϵ Aurigae.

1.1 The (abridged) history of ϵ Aurigae

Few objects in astrophysics are as well studied, but so poorly understood as ϵ Aurigae (HD 31964). As new observational techniques and theories were developed, they have been applied to this system, with often inconclusive or otherwise distressing results. Because of this, studying ϵ Aurigae is, in many respects, an overview of 20^{th} century astrophysics! In this section I present a significantly abridged overview of the literature on this system, focusing on theoretical and observational developments.

Our modern perspective affords us the knowledge that this system is a single-line spectroscopic eclipsing binary, but this was not always the case. As far as the author is aware, the first documented case of ϵ Aurigae's dimming was made in 1821 when High Minister Fritsch of Quedlinburg, Germany published an inquisitive remark:

> Den Stern ϵ in der Ziege des Fuhrmanns sahe ich oft gegen ζ und η so schwach, dafs er kaum zu erkennen war. Hat man dies schon beobachtet?
>
> [I often see the star ϵ in the goat of Aurigae so faint compared to ζ and η, that it is barely recognizable. Have you observed this?]
>
> -Fritsch (1824)

After this initial observation by Fritsch (1824), and rediscovery by Schmidt, several additional observers (i.e. Argelander, Heis, Oudemans, Schoenfeld, Schawb, Plassmann, Sawyer, Porro, Luizet, Frau von Prittwitz, Kopff, and Goet) systematically monitored the star. Their work revealed periodic dimming, similar to that seen in the present-day eclipse (see Figure 2.2 on page 45). Using reports of their efforts, Ludendorff (1903) established the 27.1-year periodic nature of the dimming. A few years later, the first analytic method for determining the orbital elements of eclipsing binary systems was published (Russell 1912b;a). Later application of these formulae came to an interesting conclusion: the system was composed of two stars, the visible F-supergiant, and an equally massive, but yet photometrically and spectroscopically invisible companion. Such a striking conclusion led some to doubt that eclipses were even the root of the photometric variation:

> The difficulty at present seems to be the lack of harmony between photometric and spectroscopic data. Ludendorff's unpublished spectroscopic observations of the system apparently indicate the existence of but one spectrum, and further the spectrum visible during supposed totality is evidently the same one as seen outside of eclipse. Definite acceptance or rejection of the eclipse hypothesis may rest upon the study of the next minimum.
>
> -Shapley (1915; note 18)

1.1.1 Photometric interpretations

The earliest spectroscopic data established the F-type ($T \sim 7500$ K) nature of the visible supergiant (hereafter the "F-star"), but no information was known about the secondary. This situation caused much speculation about the nature of the companion by some of the biggest names in astrophysics.

The earliest explanation for the eclipse was quite simple and, amazingly, in line with modern interpretations. Ludendorff (1912) stated that an eclipse with similar characteristics could be caused by a "swarm of meteorites" passing in front of the F-star. Perhaps not so surprisingly, Ludendorff did not give much regard to his remark, as his own spectroscopic orbital solution implied the meteorites would amount to nearly 23 $M_{\odot}$ (solar masses) of material.

A few years later Kuiper et al. (1937) proposed that the eclipse was actually caused when the observable F-star passed behind the atmosphere of a giant "infrared star." In this scenario the flat-bottomed nature of the eclipse is due to the primary's light being scattered/refracted by the infrared star's atmosphere. Although interesting, this theory was later shown to be impossible. The model demanded a minimum electron pressure of 0.1 dyne/cm^2, but Kraft (1954) used in-eclipse spectroscopic data to show the eclipsing object had an electron pressure three orders of magnitude lower. At this low pressure, electron scattering cannot account for the eclipse.

To partially address the failures of the Kuiper et al. model, Schoenberg and Jung (1938) proposed a model where the companion was instead a sufficiently cool star that permitted the formation of solid particles during the convective process. The particles, once formed, will lack the necessary hydrostatic support to remain aloft in the star's atmosphere. Therefore they fall, are re-heated, and break apart. Although solid particles explain the "gray" nature of the eclipse, a nearly spherical shell of material around the companion will not give rise to the flat-bottomed light curve during totality. This, and the difficulty explaining why a stochastic process

like convection would exhibit a 27-year period, caused this model to quickly lose favor in the astronomical community.

Somewhat serendipitously during a detailed refutation of the Kuiper et al. model, Kopal (1954) proposed properties of an object similar to modern-day interpretations. He postulated that the companion to the F-star is a flat, semi-transparent *ring* of material with a radius of ~ 6 AU. This object should be inclined with respect to the plane of the eclipsing body's orbit and be composed of sold dust particles of $10 - 100\mu$m, rather than excited gas, to explain the grayness of the eclipse. The ring's proximity to the F-star made it unlikely that hydrogen would be the dominant element. Instead, he argued that the ring is probably formed of crystals of water or light hydrocarbons. It appears he regarded the ring to have a total mass of ~ 1 $M_{\odot}$, although his choice of language could imply the whole secondary component has that mass. This model is later refined in Kopal (1971) in response to the work of Huang and Wilson (discussed below).

Following the 1955 eclipse, interests were renewed in ϵ Aurigae. Huang (1965) created the first analytical model for the eclipsing object. The model was composed of a disk of material, seen nearly edge on, that was both physically and optically thick. By moving the disk across the face of the F-star, the resulting photometry qualitatively agreed with the observed light curve. In his work, Huang also alluded to observational data that indicates the disk is asymmetric, with residual gas trailing behind the disk.

The success of the Huang disk model has endured, and it is now largely agreed that the companion is a disk-like object. Wilson (1971) offered improvements to the Huang model by creating a computer simulation of the resulting light curve from Huang's thick disk. Wilson's main criticism was that a thick disk would result in a flat-bottomed light curve whereas the 1955 eclipse shows a central brightening as well as "lobes" on either side of mid-eclipse. As will be discussed in Chapter 2, the

"lobes" were most likely manifestations of the F-star's intrinsic variability. Using the 1955 eclipse data as a guide, Wilson proposed a physically thin, but optically thick disk with a central opening. Huang disagreed with Wilson's interpretations (see Huang 1974), but eventually indicated that the true solution is probably between the Wilson and Huang models.

The last modification to the Huang model came from Ferluga (1990) in which he investigated the main structural features, not the physical composition, present in the disk. He argued that the disk was not a continuous aggregate of dust, but instead a series of concentric rings with Cassini-like divisions and a large central opening to explain the mid-eclipse brightening observed during the 1983 eclipse (Hopkins 1985). By simulating the appearance of the star in 10-day intervals, he used the data from the 1929, 1956 and 1983 eclipses to show there is no systematic trend (including disk precession) that could account for changes in totality brightness. Instead he suggested that the opaque regions in the disk are becoming more transparent.

Even though the disk model did a good job explaining the eclipse qualitatively, the disk had not been directly detected. The success of Einstein's General Theory of Relativity and the prediction and later observations of gravitational lenses in 1979, prompted Schmidtke (1985) to consider if the mid-eclipse brightening could be explained in this context. Given an estimated distance to the system and assumed masses for the components, it was concluded that a gravitational lens is not a plausible explanation for the mid-eclipse brightening.

As with many events in the history of ϵ Aurigae, advancements in technology yielded new discoveries in this system. With the exception of some "radiometric magnitudes" in the late 1930s, infrared detectors were not extensively applied to the system until the 1960s. This resulted in the claim of an infrared excess consistent with a 500 K source (Mitchell 1964), which was later retracted (Low and Mitchell 1965) when subsequent data were acquired. During the 1983 eclipse, Backman et al.

(1984) studied the system in $JHKL'MN$ and Q photometric filters. These data proved that a 500 $\pm$ 150 K source existed in the system. This "infrared excess" was interpreted to be the first direct detection of the disk.

1.1.2 Dynamical considerations

While most authors concentrated on interpreting the light curve, others considered the nature of the eclipsing object directly. How could the flux from a $\sim$ 15 $M_{\odot}$ (solar mass) star be hidden by a disk?

One author, in particular, speculated that the low light-to-mass ratio of the secondary could be explained by placing a black hole at the center of the disk (Cameron 1971a;b). This theory was eventually disproved, but only after sufficiently accurate X-ray observations could be acquired. These data constrained the X-ray flux from the system to be comparable to background radiation, thereby undermining the black hole hypothesis (Wolk et al. 2010).

Others invoked a simpler solution: instead of one star, let there be two. Eggleton and Pringle (1985) proposed that the light-to-mass ratio could be explained by having a pair of equally massive stars inside of the disk. This scenario had the added benefit that an exchange of orbital angular momentum between the binary and the disk particles would maintain the disk shape between eclipses, even in the presence of the nearby F-star.

1.1.3 Evolutionary considerations

With the disk theory for the nature of the secondary garnering significant support, the debate shifted to the origin and evolutionary scenario for this system. Until 1985, the F-star was regarded as a F0Ia supergiant of about 15 $M_{\odot}$. The nearly equally massive 14 $M_{\odot}$ companion was thought to be a young stellar object (YSO, a star in its earliest stages of evolution). Eggleton and Pringle (1985) coined this

interpretation as the "high mass" scenario and presented a case for a new "low mass" explanation. They argued the F-star is a post-asymptotic giant branch (post-AGB) star which has already lived most of its life. In this case, the F-star would be $2 - 5\ M_{\odot}$, whereas the unseen companion was *more massive*, $4 - 6\ M_{\odot}$. In this scenario, the disk would be composed of mass lost from the F-star during Roche lobe overflow or traditional mass loss.

1.2 A stellar evolution interlude

Now that I have introduced the two possible evolutionary scenarios for the system, I wish to spend a few paragraphs discussing the differences between these two cases. The full details of stellar evolution are extensively discussed in Iben (1967; 1991), Iben and Livio (1993), Iben (1995) and in modern astronomical textbooks (i.e. Hansen et al. 2004), therefore I will only highlight the cases which are relevant to this work, egregiously ignoring the finest details.

All stars start out as clouds of gas and dust[1] that gravitationally contract to form a proto-star. If there is enough mass ($M > 0.085\ M_{\odot}$), temperatures and pressures in the core become high enough to start converting hydrogen (H hereafter) into helium (He hereafter) via. fusion. When this occurs, stars are said to be *on the main sequence*. Stars spend a majority of their lifetime in this state.

Stars with an *initial* mass $0.085 < M < 0.85\ M_{\odot}$ will eventually consume the H in their cores; however, this process is extremely long and therefore not of interest to this discussion. Stars with an *initial* mass $M > 0.85\ M_{\odot}$ consume their H faster, therefore their evolution is observable. When the stars leave the main sequence, H fusion in a shell causes an expansion of the outer envelope which results in higher luminosities, lower temperatures, and greater radii. These stars are said to be

[1]For astronomers, dust is an aggregation of any material. Silicates and Carbonates are common examples. Note that dust did not exist for the earliest stars. So-called "Population III" objects are thought to have formed from only gas.

ascending into the red giant branch (RGB).

For stars with $M < 0.4\ M_{\odot}$ the He core becomes degenerate, prohibiting temperatures from rising any further. Theoretically, we predict these stars will eventually evolve into He white dwarfs. For stars with $M > 1.5\ M_{\odot}$ temperatures in the core rise faster than densities, therefore He fusion begins quite peacefully. For stars in the intermediate mass range, $0.4 < M < 1.5\ M_{\odot}$, He fusion begins when the core is partially degenerate. Once the thermal pressure exceeds the degeneracy pressure the gas suddenly expands during an event astronomers call the *helium flash*. When this occurs, stars descend from the RGB and onto the horizontal branch.

During the horizontal branch stars undergo He fusion, producing carbon (C), nitrogen (N), and oxygen (O). The CNO process is very slow as it depends on the core being both hot and dense enough to fuse three He nuclei together. Stars in this stage of evolution feature H fusion in a shell, thereby providing additional energy to support hydrostatic equilibrium. Once enough He is converted stars begin to develop a C/O core.

1.2.1 Post-AGB stars

Objects with $M < 6 - 8\ M_{\odot}$ lack enough mass to fuse any further material beyond He. Because hydrostatic equilibrium must be maintained, the C/O core contracts and liberates gravitational potential energy. After the core sufficiently shrinks, a thin layer of He fusion begins in a shell causing the star to expand again. The star now asymptotically approaches the RGB. This stage of stellar evolution is called the asymptotic giant branch (AGB). This phase is typified by unstable pulsation caused by alternating H and He shell fusion. This results in large pulses that propagate through the stellar atmosphere. These pulses, combined with high luminosity, low surface gravity, and low temperatures that permit the formation of molecules, cause the star to undergo tremendous mass loss. The end of the AGB phase comes with

significantly enhanced winds. These strip away a majority of the star's envelope, effectively terminating the AGB phase.

The copious quantities of material lost along the AGB phase make observations of the earliest phases of post-AGB evolution difficult because as the constituent star is enshrouded in a veil of dust and gas. Eventually the surrounding material becomes optically thin and the central star can be directly observed. From here, the star evolves at a nearly constant luminosity, but increases in temperature. When the central object reaches $\sim 50,000$K, photons have enough energy to ionize the surrounding material which fluoresces as a planetary nebulae. The remaining carbon-oxygen core eventually cools down and yields a white dwarf.

Post-AGB stars make up a very inhomogeneous group of objects. Many, but not all, post-AGB stars have circmumstellar material and/or disks. This results in a spectral energy distribution with two peaks. Often, post-AGB stars exhibit elevated levels of *s*-process [2] materials and molecular absorption lines, yet a lack of these features does not mean a star is not a post-AGB. For example, supposed post-AGB objects, HR 6144, HD 133656, and SAO 239853 all have low metallicity[3] and slight C enhancements (Van Winckel 2003), but otherwise normal spectra. Van Winckel also discuss the case of HD 179821. This system exhibits all of the classic signs of post-AGB evolution (spectrally rich in O; strong infrared emission, a resolved circumstellar envelope in the near-IR, mid-IR, CO; and OH masers), whereas spectral abundance studies of the principal component attest that the object is a normal supergiant.

[2]The *s*-process is slow neutron capture that occurs in the cores of stars with intermediate temperatures and low neutron density.

[3]Metallicity is the fraction of a star's material that is made up of elements that are not H or He.

1.2.2 Supergiants

Unlike post-AGBs, supergiants are stars with an initial mass $M > 6-10\ M_{\odot}$. These behemoths have sufficient mass pass through the He fusion phase and proceed to fuse the resulting C in the core. Unfortunately, it is also at this point that interpreting the star's evolution in terms of the Hertzsprung-Russell (HR) diagram becomes mostly useless as fuels are consumed so rapidly that there is little time for the material to be transported to the star's outer layers. C is converted to Neon (Ne) and Sodium (Na) in $10^3 - 10^4$ years. Ne is converted to Magnesium (Mg) and some O in $10^2 - 10^3$ years. O is fused into Silicon (Si) and Sulfur (S) within a year, and finally Si to ^{56}Nickel (^{56}Ni) within days (Hansen et al. 2004).

The result of this process is a star that could be regarded as onion-like, with multiple shells consuming nuclear fuel and depositing the by-products on the deeper layers. ^{56}Ni radioactively decays into Iron (Fe). Fe has the most tightly bound nucleus and is the last element that may be produced by an exothermic nuclear reaction. With a loss of energy in the core, hydrostatic equilibrium cannot be maintained. Fusing of heavier elements takes energy from the core which causes the core to collapse and the star to explode as a core-collapse supernova.

Supergiants, like post-AGB stars, span the entire upper region of the HR diagram. These bright stars are recognized by their spectral characteristics, namely narrow H absorption lines in their spectra. Population I supergiants[4] tend to show C deficiency, N enrichment and almost no change to O over solar levels. Additionally, supergiants tend to show an enhancement of Na that is correlated with surface gravity, $\log g$ (El Eid and Champagne 1995).

[4]Population I stars are luminous, young stars that often occur in spiral arms. The Sun is a member of this group.

1.3 The quandary of interpreting ϵ Aurigae

From its location in the HR diagram, we can say definitvely that ϵ Aurigae is either a post-AGB or a traditional supergiant. A principle difficulty in distinguishing these two cases is that the photosphere of either type of object obeys the same physics largely regardless of the object contained therein. This fact cannot be stressed enough when ϵ Aurigae has been found to have a spectrum similar to not only post-AGB and supergiant stars, but even novae (Saselov 1986)!

Modern spectroscopy has not been very helpful in resolving the dichotomous state of ϵ Aurigae. A spectroscopic study by Sadakane et al. (2010) indicated a slight overabundance of *s*-process materials, a slight depletion of C and O, but an otherwise "normal supergiant" spectrum when compared to abundances found in five supergiants and four *s*-process enriched post-AGB stars. The authors used the "usual spectroscopic method" for evaluating the abundances of the F-star. When working with post-AGB objects, one must exercise extreme caution because many elements used as spectral references may have been depleted. For instance, the traditional [X/Fe] reference[5] is no longer reliable for the purpose of discussing chemical peculiarity, as Fe is often depleted! With post-AGB stars, one should first inspect the [Zn/Fe] ratio to see if dust-gas separation has occurred prior to detailed spectral analysis (Takeda et al. 2007). Even with this effect taken into consideration, the [C/Zn], [N/Zn], and [O/Zn] ratios do not always appear different from those seen in the first dredge-up[6] of normal population I supergiants (C deficiency, N enrichment, O barely changed). So, the typical markers for post-AGB evolution (see Bond 1991) may not be applicable to all post-AGB stars.

[5]The bracket notation, [X/Y], indicates the logarithmic ratio with respect to solar values, $[A/B] \equiv \log(A/B)_* - \log(A/B)_\odot$.

[6]A period in stellar evolution where the convective layers of the star extend further inward and bring nuclear processed material to the surface. This results in an enrichment of processed materials being detected in the star's spectrum.

Contrary to the latest spectroscopic work, historical work has indicated that *something* is evolved in the ϵ Aurigae system. Hinkle and Simon (1987) reported the appearance of CO with an isotopic ratio of $^{12}CO/^{13}CO = 10 \pm 4$ during the eclipse. Likewise, Stencel et al. (2011) reported CO shows up only during eclipse, therefore it may be associated with the disk. What is intriguing is the reported extreme abundance of ^{13}CO! The measured isotopic ratio in the solar neighborhood, and most YSOs is ~ 89 (Smith et al. 2010). The ratio in ϵ Aurigae implies that ^{13}CO has been *created* in the system and then *deposited* in the disk. If confirmed, this is the strongest evidence to date in favor of the F-star being a post-AGB.

A final vote in favor of the post-AGB interpretation comes from Hoard et al. (2010). In this work the authors argued for the detection of a B5$\pm$1 star inside of the disk based upon SED fitting to a small portion of the UV spectrum (0.1 - 0.15 μm) where the F-star is no longer the dominant source. Using the corresponding mass for this star and the spectroscopically observed mass function, they determined the F-star's mass is $\sim 2.2\ M_{\odot}$, excluding the supergiant interpretation.

1.4 Hypothesis, proposed solution method, and outline

Now that the reader has garnered a deeper understanding of the history and issues with interpreting ϵ Aurigae, it is appropriate to discuss the focus of this dissertation.

The aforementioned $^{12}CO/^{13}CO$ ratio and recent results from Hoard et al. (2010) provide compelling evidence that led to my choice in research topic. My hypothesis is that the F-star is not a massive supergiant as classically assumed, but instead a lower-mass post-AGB star that has recently (in the evolutionary sense) lost a few solar masses of material. Most of this material has coalesced in a disk surrounding the hidden companion.

To test my hypothesis I will investigate three fundamental questions:

1. What is the nature of the photometric variability observed outside of eclipse and how does it relate to supergiant and post-AGB behavior?

2. Is there really a disk in the system and, if so, what are its geometric and optical properties? Is the disk typical of YSO or other disk objects?

3. Can the masses of the individual components be determined by dynamical means? If so, what do the observed masses imply about the evolutionary state of the system?

In the following chapters I explore each of these topics in greater detail. In Chapter 2, I explore the hitherto indeterminate photometric variations of the F-star using 27 years of photometric data. In Chapter 3, I present interferometric observations of the system before, during, and after the $2009 - 2011$ eclipse. Here I discuss the first resolved images and models of the eclipsing object. In Chapter 4, I revisit prior orbital solutions, astrometric observations, and radial velocity data to drive a new distance estimate for the system as well as the first observationally determined mass ratio and component masses. Lastly, in Chapter 5, I summarize the work and discuss the evolutionary state implied by the prior three chapters.

Chapter 2

Long term photometry of ϵ Aurigae

The lure of a 50% reduction in light has brought a multitude of observers and researchers to ϵ Aurigae every 27 years, but few pay attention to the system outside of eclipse. As early as the late 1800s, it was clear that the system undergoes some form of quasi-periodic variation outside of eclipse, but few regarded this effect in their research until the mid-1950s. In this chapter, I analyze 27 years of inter-eclipse UBV photometry using modern period analysis methods and find a hitherto undiscussed trend that may be crucial to future researchers. I compare the behavior seen in ϵ Aurigae with bona-fide supergiants and post-AGB stars of similar spectral type, and briefly discuss which of these two classes of objects posses variational patterns that most closely match what is seen in the F-star.

2.1 Introduction

The earliest discussion of the out-of-eclipse (OOE) variations of ϵ Aurigae were from a nearly parenthetical remark by Shapley (1915; p. 20). He comments on

variations in visual photometry with an amplitude of ΔVis. = 0.3 magnitudes. Because observational errors were not fully characterized, Shapley treated these results with caution. Later, Güssow (1928) spotted a ΔVis. = 0.15 mag variation outside of eclipse that was corroborated by two photoelectric photometers (Shapley 1928), thereby confirming the presence of the OOE variations. Shapley concluded that these variations arose from a $\sim$ 355 day quasi-periodic variation; however, the exact period was poorly constrained by the data.

2.1.1 Prior work

Since the early 1900s, several works have attempted to identify the nature of the OOE using different data sources. With the exception of the early work by Güssow, the first detailed period analysis was undertaken by Arellano Ferro (1985). In this work, the author used a combination of photometric and radial velocity data to establish the periods listed in their Table 5. Photometrically determined periods were 123 and 159 days, whereas the radial velocity data tended to predict longer periods of 112, 161, 168, 188 and 556 days.

After the 1984-1986 eclipse, Kemp et al. (1986) proposed a $\sim$ 100 day period may exist in polarimetry data. Later, Henson (1989) showed there was little to no wavelength dependence in the variations, implying that the source of polarization is Thompson scattering from free electrons. In his dissertation, Henson found intervals where there were variations in Stokes Q, but little to nothing in Stokes U. This was interpreted to be caused by the F-star having two major axes for polarization, inclined at an angle of 45 degrees with respect to each other. Like many of the other studies, a visual inspection of Henson's data shows that some long trends may indeed exist, but nothing is strictly periodic. From the post-eclipse polarimetry, Henson concluded that the photometric and polarimetric variations might be caused by non-radial pulsation in low-order $\ell = 1, 2$ $m = \pm 1$ modes. This notion is supported by

the recent automated classification of ϵ Aurigae as an α Cyg variable (Dubath et al. 2011) which are a bright class of supergiants that undergo non-radial pulsation.

After the 1985 eclipse, many authors sought to determine periods of the OOE variation. Using data from the first five years after the eclipse, Nha et al. (1993) found occasional stable variational patterns would set in (in particular around JD 2447085 - 2447163) with $\Delta U = 0.27$, $\Delta B = 0.17$ and $\Delta V = 0.08$ and a characteristic period of 95.5 days.

Later, Hopkins and Stencel (2008) analyzed their inter-eclipse V-band photometric data using the Peranso software package (Husar 2006). They found two dominant peaks in the Fourier power spectra with 65 and 90-day periods.

Perhaps the most comprehensive period analysis effort was made by Kim (2008). They used the CLEANest Fourier transform algorithm and the Weighted Wavelet Z-transform (WWZ Foster 1996) on nearly 160 years of photometry of ϵ Aurigae. Using these two algorithms they identified several periods which led them to conclude ϵ Aurigae may be a double or multi-periodic pulsator. We have summarized the periods they discovered in Tables 2.1 and 2.2.

Table 2.1: Period analysis by Kim (2008) ϵ Aurigae, periods $50 - 149$ days

			Periods (days)									
JD Start	JD End	Years	50-59	60-69	70-79	80-89	90-99	100-109	110-119	120-129	130-139	140-149
2396294	2399403	1848-1857		63, 66						125		
2406614	2407420	1876-1879		66					112115			152
2414288	2416245	1897-1903	57							121,124,128		
2417436	2419306	1906-1911		69				106		121		149
2424808	2427154	1926-1933	58	68				100,105	112	123,125	137	
2427369	2428525	1933-1936				83			116			
2435060	2435290	1954-1955		61				105		123		
2436053	2437023	1957-1960	57	69	76	86			110	120	139	
2445952	2447627	1984-1989		61,68	75		95			125		
2452978	2453845	2003-2006		66,68				100,108				

Table 2.2: Period analysis by Kim (2008) ϵ Aurigae, periods $150 - 600$ days

			Periods (days)									
JD Start	JD End	Years	150-159	160-169	170-179	180-189	190-199	200-249	250-299	300-399	400-499	500-599
2396294	2399403	1848-1857		166	171							
2406614	2407420	1876-1879	150	165							463	
2414288	2416245	1897-1903		162							434	
2417436	2419306	1906-1911		169		182			292	312		
2424808	2427154	1926-1933	151,'153,156			188						526
2427369	2428525	1933-1936	158	167			192	200				556
2435060	2435290	1954-1955		161							454,463,476	
2436053	2437023	1957-1960	159	161,167		185		234	270			556
2445952	2447627	1984-1989	155					220				539
2452978	2453845	2003-2006	150							310		555

2.1.2 Variational patterns: eclipses, wiggles, and flares

The eclipse events of ϵ Aurigae have been thoroughly discussed in prior literature (e.g. Ludendorff 1903; 1912, Güssow 1936, Stencel 1985; and references therein). Even though the photometric systems have changed, the $\sim 50\%$ reduction in light and time of the eclipse are well established. Figure 2.1 (pg. 44) displays 27 years of inter-eclipse photometry from two different observatories (discussed below). A visual inspection of these data reveals that the system is variable outside of eclipse. At times there appear to be stable, sawtooth-like wave patterns with characteristic timescales of months, whereas at other times the star is not variable for similarly long periods of times.

In addition to these month-long wiggles in the light curve, there are several reported instances of short-term (i.e. few-day long) flares. An exceptional brightening lasting a mere 5-days with $\Delta U = 0.2$, $\Delta B = 0.1$ and $\Delta V = 0.06$ was observed by Albo and Sorgsepp (1974) around JD 2439968. We have been unable to locate a second photometric source around this date to corroborate this claim. On JD 2445356 a flare was reported by Nha and Lee (1983) who noted a rapid (few hour) 0.4 mag rise in the blue filter and 0.2 mag in the yellow filter. Observations of a check star, η Aurigae, showed no significant deviations, therefore it would appear this event is indeed real. As we will discuss below, it also appears that there was a two-night flare event in 1986 that resulted in similar changes in magnitude.

In addition to photometric variations, Castelli (1976) has reported spectroscopic variations in optical wavelengths ($3600 - 6750$ Å) with $\sim$ 15-minute timescales. Recent rapid-cadence U-band photometric monitoring by Billings (2010) found no significant variations on similar timescales.

2.2 Historical data sources

In this work our primary concern is with data from 1980 and thereafter; when the most consistent set of UBV photometric data is available. However, in addition to using this data, we have also conducted a comprehensive literature review and found 27 sources of historical photometry from 81 different observers. We have digitized all of these data and intend to publish them, in electronic form, in a future publication. In the next several paragraphs we describe the historic sources including information about the observatory, instrumentation, comparison and check stars, and estimated uncertainties when possible. All sources of photometric data (historic and new) are summarized in Table 2.3.

The first major publication of photometry was work done by Ludendorff (1903), who summarized data from 12 separate observers (Argelander, Heis, Oudemans, Schoenfeld, Schwab, Plassman, Sawyer, Porro, Luizet, Frau von Prittwitz, Kopff, and Goetz). The earliest data were by Argelander in 1842. A majority of these data originate in German observatories and unpublished sources; however, one source comes from the Osservatorio Astronomico di Torino in Italy. Although sometimes mechanically assisted, the photometry is all visual (i.e. by eye). The earliest data predate the establishment of the Pogson photometric system, therefore care must be taken when working with these data sets. In a later work Ludendorff (1912) presented a series of visual magnitude estimates by Schmidt at the Bonn observatory. These data were averaged into twice-per-month bins. English translations of these seminal works by Ludendorff were provided by Roger Mansfield and are available from Robert Stencel or Brian Kloppenborg.

Wendell (1913) reported mechanically-assisted (see Wendell 1909; and references therein) visual observations taken with the 15" East Equatorial at Harvard College from 1904-1912. We have copied the nominal photometric values directly from the manuscript. Our uncertainties were calculated from the quadratic sum of the

published residuals divided by the number of observations (four). Note that Shapley (1928) used these data in their work, therefore these data were excluded from our digitization of Shapley (1928).

Between 1928 January and 1931 May, Huffer (1932) used the telescope at the Washburn Observatory to monitor the eclipse. Using a photoelectric photometer and a series of neutral-shade glasses, the brightness of ϵ Aurigae was diminished to approximate equality with HR 1599 (5 Aur) and HR 1688. The same procedure was conducted to dim ϵ Aurigae to the same brightness as HR 1729 (λ Aur). Allowances for differential extinction have been made. The authors reported the mean magnitude and residuals with respect to the three comparison stars. In our reduction, we have adopted the mean magnitudes and computed an uncertainty from the quadratic sum of the residuals divided by the number of observations (three). In the case that the residuals are zero, we have adopted the mean residuals ($\pm$ 0.008 for 4 Aurigae, $\pm$ 0.007 from HR 1668, and $\pm$ 0.010 from λ Aurigae) which result in an average error of $\pm$ 0.006 mag. A visual inspection of these data shows the presence of the 0.1 mag variability outside of eclipse.

Ivanov and Scharbe (1934) reported 83 observations made by Professor S. B. Scharbe between 1907 September 2 to 1907 December 31 and 1927 December 22 and 1930 May 7. The authors used a mechanically-assisted visual photometer. They compared ϵ Aurigae against 10 comparison stars. The authors note that their results compare favorably to those in Güssow (1928). No estimates for the uncertainties are provided in the article, therefore we have assumed an error of $\pm$ 1 in the least significant digit (i.e. $\pm$ 0.01 mag).

98 Observations from the Observatoire de Marseille taken between 1927 September 6 and 1938 December 5 were reported by Danjon (1936). Two, much fainter, comparison stars, BD +43°1177 (HD 32328) and BD +44°1077 (HD 31866), were used in reducing the data. No uncertainties were reported, therefore we have as-

sumed an error of ± 1 in the least significant digit (i.e. ± 0.01 mag).

Güssow (1936) converted the work of 28 separate observers into the Potsdam photometric system. Her work was thorough and discusseed the techniques, comparison stars, and reduction methods used by each observer. Common comparison stars were θ Aur, ι Aur, ϵ Per, η Aur, and ζ Aur. The observers whose work was included are Nijland, Plassmann, Enebo, Wendell, Schiller, Lohnert, Scharbe, Mundler, Lau, Hornig, Menze, Guthnick, Johansson, Guthnick & Pavel, Gadomski, Graff, Kordylewski, Gussow, Kukarkin, Beyer, Danjon, Jacchia, Pagaczewski, Stebbins & Huffer, Tschernov, Mrazek, Dziewulski, and Kopal.

This paper includes a significant quantity of out-of-eclipse data, constituting the earliest long-term photometric monitoring of ϵ Aurigae. Visual inspection of the figures in Güssow (1936) showed the presence of some variability outside of eclipse. Interestingly, the magnitude of the variations appeared to increase in the vicinity of primary eclipse. This does not occur in modern photometry, therefore we suspect this is an observational bias in which knowledge of the upcoming eclipse caused the observers to be more attentive to small photometric changes in the system. As our work is primarily interested in the timescale of these variations, and not their amplitude, this observational bias is of little consequence; however, we caution future researchers to be aware of these affects when this data set is used. As briefly mentioned above, Güssow's data revealed small, ΔVis = 0.15, fluctuations outside of eclipse.

The earliest infrared observations of which we are aware were presented by Emberson et al. (1938) in which seven "radiometric magnitudes" were discussed. The instrument used had a broadband sensitivity covering $0.1 - 12\mu$m. The earliest data point was acquired in 1938 January 03 and the last 17 days later on 1938 January 20. If the residuals are taken as a proxy for uncertainties, no variations are seen outside of 1-σ limit. We are not aware of any follow-up observations with this instrument, therefore we have not included it in our analysis. We mention it only for completeness.

Between the 1930 and 1957 eclipse, several advancements in observing techniques and technology were made. Indeed, among the first photometric observations with filters was Thiessen (1957) who made a few Yellow, Blue, and Violet differential observations during the ingress phase of the 1957 eclipse. Although the authors clearly state the effective wavelengths of their filters and the reference stars, they neglect to mention the inherent magnitude of the reference stars in these filters. These 10 observations are not recoverable with the information provided and are therefore not included in our reduction.

Larsson-Leander (1959) observed ϵ Aurigae with an EMI type 5060 photometer attached to the 60 cm Stockholm Observatory refractor during the 1955-1957 eclipse. Blue observations were taken through a Corning 5030 plus Schott GG13 filters whereas yellow observations were taken through a Corning 3384 filter. The comparison star was HR 1644 and λ Aur was used as a check star. η Aur was used as a comparison star early in the campaign, but was later discarded as it appeared to be slightly variable. Linear corrections for airmass were applied and the data were transformed to the standard photo-visual (PV) system. Following the discussion in the manuscript, we have assumed an uncertainty of 0.012 mag in P for all points whose $sec(z) < 1.50$ and double that value otherwise. We have also assumed this value is representative of the error in P-V and V.

The author's 1962 publication, Larsson-Leander (1962), includeed an additional 26 observations taken with the same equipment and reduced using the same method as their 1959 work. We have made the same assumptions about data quality and uncertainties.

Widorn (1959) presents 219 blue and yellow observations taken between 1955 January 17 and 1958 March 17. Data were acquired using a EMJ 5659 photometer mounted to a 40 cm "Cassegrain-Spiegel" telescope. The yellow band is a Schott GG7 $2mm$ thick glass ($\lambda_{eff} = 380\mu m$) filter whereas the blue band is a 1-mm thick Schott BG 3 ($\lambda_{eff} = 520\mu m$) filter. Comparison stars were η Aur, λ Aur, and μ Aur. HD 32188 served as a check star for η Aur. Extinction correction were applied and a mean error of $\pm$ 0.016 magnitude was obtained. The authors did not attempt to apply color corrections to transform these data into a standard photometric system, but they did provide the color index of η Aur in their Table 6. As of this writing, we have not transformed these data into a standard filters system. Therefore we have not included it in our present efforts.

The Flower and Cook observatory also contributed data during the 1955 eclipse. The 15" siderostat was used with a 1P21 photomultiplier and four filters. Fredrick (1960) presented their 65 observations which start on 1954 January 17 and end in 1957 March. One filter is a Corning 5860 1.75 mm which covers the ultraviolet. The remaining filters are Schott interference filters. Two of them are centered at 4250 Å and 5250 Å with a 90 Å bandwidth. The remaining filter has a maximum transmission at 4880 Å with a 130 Å bandwidth Wood and Blitzstein (1957). We have yet to identify a method to transform these data into a standard photometric system, therefore they are not included in our present effort.

An interesting paper from Kopylov and Kumaigorodskaya (1963) examined the spectroscopic properties of the F-star while attempting to identify the properties of the disk by comparing pre-, in-, and post-eclipse spectra taken at the Crimean

Astrophysical Observatory in the Ukraine. In addition to their spectroscopic data, a series of photometric data points in the photovisual (PV) system were acquired between 1955 January 03 and ending on 1959 May 06. Unfortunately we were unable to talk with the original authors and our contact at the observatory was not able to locate the original photometric records. Therefore, we extracted and digitized their Figure 1. We have assumed the uncertainties are similar to other PV records of the time, with $\sigma P \sim 0.01$ mag.

A series of $UBVRIJHKLN$ photometric data points were taken by Mitchell (1964) and Low and Mitchell (1965) using a 1P21, a 7102, and a PbS detector. In the former work, the authors claim to have detected an infrared excess corresponding to a blackbody at 500 K; however, in the latter work, the authors retract this claim based upon new N-band photometry. Although both magnitudes and uncertainties were included in both publications, dates were not. Therefore these data are only noted for historical importance.

Stub (1972) presented a series of narrow-band photometric data points taken at the Copenhagen University Observatory at Brorfelde with the 10, 16, and 20-inch reflecting telescopes. Data were taken differentially with HR 1729 serving as the comparison star. HR 1494 and HR 1551 were check stars. Stub used 10 narrow-band photometric filters that, to the best of the author's knowledge, do not correspond to any "standard" filter set used in astronomical photometry. We have assumed the stability of the reference stars, $\Delta = 0.02$, is a suitable proxy for the internal uncertainties. These records have been digitized, but are not used within this study.

Albo and Sorgsepp (1974) and Albo (1977) report on a total of 62 V, $(B-V)$, and $(U-B)$ observations taken between 1968 Apr. 21 and 1968 May 11; and 1969 August 26 and 1969 November 22 in the respective publications. They have transformed their data into the standard UBV photometric system and applied extinction correction. In their earlier publication they used δ Per and HR 1644 as

comparison stars, and λ Aur as a check star. Here we have assumed an uncertainty of ± 0.005 for all photometry. As mentioned above, they reported a flare near JD 2439968 whose amplitude was $\Delta V = 0.06$, $\Delta B = 0.1$, and $\Delta U = 0.2$ which lasted for less than five days.

Japan Amateur Photoelectric Observers Association (1983) provided 46 differential UBV observations between 1982 September 24 and 1983 March 14 collected by Abe, Ohmori, Ohki, and Yoshinari. λ Aur was used as the comparison star and Johnson standard stars were used to convert the data to the standard UBV photometric system. The authors do not explicitly mention airmass corrections in their publication. However, reducing data to the standard system necessitates that one consider this affect, therefore we believe it has been applied. The authors do not discuss their uncertainties, therefore we have assumed ± 0.005 uncertainties for all data points.

Backman et al. (1984) presents the first large set of infrared observations in $JHKL'MNQ$ filters taken at NASA's Infrared Telescope Facility (IRTF), the Kitt Peak National Observatory (KPNO), and the University of Hawaii observatories. These in-eclipse data were used to establish the temperature of the disk, 500 ± 150 K, and provide an estimate for the size of the disk in steradians. These data, with their uncertainties, are imported as-is.

Bhatt et al. (1984) reports a total of 8 $BVRI$ observations taken with a 14" Celestron Telescope using a solid state photometer and 3 JHK observations made with the 40" telescope of the Uttar Pradesh State Observatory at Nainital, India using a Liquid N_2 cooled InSb photometer. The author stated the errors are of order 0.05 magnitude so we have adopted this as representative for all errors in this work.

Flin et al. (1985) took data during the 1983 eclipse in UBV. The differential photometry was done with respect to λ Aur. Three different telescopes and pho-

tometers were used in this data set. A 5 cm Cassegrain reflector was used with an single channel EMI 9789 QB photomultipler at the Jagiellonian University observatory in Caracow, Poland. The other two telescopes were a 3.5 cm Maksutov reflector and a 2.03 cm refractor, both used with a Russian made FEU 92 photomultiplier at a station in the Bieszczady Mountains. Data were transformed into the standard UBV photometric system and extinction correction was done to first order. Internal standard errors are reported as the standard deviation of the mean. In total, 130 BV observations and four U observations were reported by the authors.

197 VBI observations, and 98 *ubvy* observations were collected from by the 76 cm reflector telescope at the McDonald observatory by Parthasarathy and Frueh (1986) during ingress and early totality of the 1983 eclipse. These differential measurements were taken with respect to λ Aur. The authors indicated standard stars were observed and monthly extinction coefficients were determined for the observatories. Therefore we believe both extinction and color transformations were applied to the data prior to publication. The authors do not include a discussion of the uncertainty estimates for their data, therefore we have assumed an error of $\pm$ 0.005 mag in all filters.

Chochol and Žižovský (1987) reports on 69 UBV observations from 1982 March 14 to 1983 November 24 with the 0.6 m photometric telescopes at the Skelnaté Pleso Observatory near Tatranská Lomnica, Slovakia. HR 1644 and 59 Per were used as comparison stars and λ Aur was used as a check star. Each entry in their data table represents the mean from 5-10 observations that were reduced to the standard UBV system accounting for extinction. Because these values were averaged, we have assumed the uncertainties are $\pm$ 0.005 mag.

Strassmeier et al. (1999) presented differential Strömgren *by* photometry around the theorized secondary minimum between 1996 and 1997. Data were taken by an EMI-9124QB photomultiplier mounted on a 0.75 m telescope. Integration time was

10 seconds. Nightly extinction correction was applied. The text indicates standard errors of $\pm$ 0.004 mag was routinely achieved in both filters. HD 33167 was used as a comparison star. The 108 observations are already available in digital form from CDS (catalog J/A+AS/140/29/wolfgang under HD 31964) so they are not included in the digital form of this document. The authors note that there is an irregular, short term variation of 0.01 mag in y, but otherwise no evidence for a secondary eclipse.

Taranova and Shenavrin (2001) reported $UBVRJHKLM$ photometry both in and out of eclipse. The out of eclipse observations were taken near the theorized date of secondary minimum in 1991. Data were corrected for both extinction and interstellar absorption when applicable. These data were available for download from CDS (catalog J/PAZh/27/393). From the text we have assumed $\pm$0.03 mag uncertainties in all filters.

In addition to the aforementioned sources, we were recently informed of a series of observations between $1906-1911$, $1933-1936$, and $1984-1985$ conducted by the Variable Star Observers League of Japan (VSOLJ). We now have electronic copies of these records, but have yet to access their quality or establish uncertainties. These data will be discussed in a future publication.

Table 2.3: All sources of photometry (historic and new). † Identified only if from a compilation source. † The photometric system used or one of the following: Pe = photoelectric, Mech = mechanically assisted, vis = visual, +vis = potentially mechanically assisted.

Source	Observer†	JD Start	JD End	N Obs.	Type‡	Notes
Ludendorff (1903)	Argelander	2393950	2404492	56	+Vis	
Ludendorff (1903)	Heis	2394511	2400252	78	+Vis	
Ludendorff (1903)	Oudemans	2398490	2399058	16	+Vis	
Ludendorff (1903)	Argelander	2403950	2404492	56	+Vis	
Ludendorff (1903)	Schoenfeld	2404049	2405988	29	+Vis	
Ludendorff (1903)	Schwab	2406614	2416245	65	+Vis	
Ludendorff (1903)	Plassman	2408093	2414961	85	+Vis	
Ludendorff (1903)	Sawyer	2409147	2413645	50	+Vis	

continued on next page

Source	Observer[†]	JD Start	JD End	N Obs.	Type[‡]	Notes
Ludendorff (1903)	Porro	2411360	2411391	3	+Vis	
Ludendorff (1903)	Luitzet	2414288	2416217	55	+Vis	
Ludendorff (1903)	von Prittwitz	2414584	2416080	18	+Vis	
Ludendorff (1903)	Plassman	2415259	2416223	29	+Vis	
Ludendorff (1903)	Kopff	2415709	2415825	6	+Vis	
Ludendorff (1903)	Goetz	2416107	2416196	6	+Vis	
Ludendorff (1912)		2395304	2406567	109	+Vis	
Wendell (1913)		2416574	2419706	41	Mech+Vis	
Shapley (1928)		2416574	2419691	26	Pe+Vis	
Huffer (1932)		2425267	2426467	98	Pe+Vis	
Ivanov and Scharbe (1934)		2417821	2426104	84	Mech+Vis	
Danjon (1936)		2425130	2429238	97	Vis	

continued on next page

Source	Observer[†]	JD Start	JD End	N Obs.	Type[‡]	Notes
Güssow (1936)	Nijland	2413488	2414280	22	+Vis	
Güssow (1936)	Plassman	2416380	2427785	430	+Vis	
Güssow (1936)	Enebo	2416425	2417326	31	+Vis	
Güssow (1936)	Wendell	2416574	2419691	25	+Vis	
Güssow (1936)	Schiller	2416848	2416973	12	+Vis	
Güssow (1936)	Lohnert	2417326	2417498	5	+Vis	
Güssow (1936)	Scharbe (1)	2417824	2418653	12	+Vis	
Güssow (1936)	Horning	2418192	2420589	51	+Vis	
Güssow (1936)	Mundler	2418323	2418657	13	+Vis	
Güssow (1936)	Lau	2419275	2429779	16	+Vis	
Güssow (1936)	Menze	2420031	2420958	39	+Vis	
Güssow (1936)	Guthnick	2420147	2420175	10	+Vis	

continued on next page

Source	Observer[†]	JD Start	JD End	N Obs.	Type[‡]	Notes
Güssow (1936)	Johasson	2422687	2423374	12	+Vis	
Güssow (1936)	GuthnickAndPavel	2422940	2423361	27	+Vis	
Güssow (1936)	Gadomski	2423016	2427060	31	+Vis	
Güssow (1936)	Graff	2424251	2425957	13	+Vis	
Güssow (1936)	Kordylewski	2424647	2425953	29	+Vis	
Güssow (1936)	Gussow	2424808	2427762	145	+Vis	
Güssow (1936)	Kukarkin	2425100	2426242	34	+Vis	
Güssow (1936)	Beyer	2425126	2426196	44	+Vis	
Güssow (1936)	Danjon	2425139	2426636	34	+Vis	
Güssow (1936)	Jacchia	2425177	2426210	41	+Vis	
Güssow (1936)	Pagaczewski	2425185	2426034	13	+Vis	
Güssow (1936)	Scharbe (2)	2425237	2426104	15	+Vis	

continued on next page

Source	Observer[†]	JD Start	JD End	N Obs.	Type[‡]	Notes
Güssow (1936)	StebbinsAndHuffer	2425267	2426467	98	+Vis	
Güssow (1936)	Tschernov	2425296	2426090	25	+Vis	
Güssow (1936)	Mrazek	2425322	2425857	4	+Vis	
Güssow (1936)	Nijland (2)	2425322	2426436	40	+Vis	
Güssow (1936)	Dziewulski	2425364	2426096	22	+Vis	
Güssow (1936)	Menze2	2425529	2426065	23	+Vis	
Güssow (1936)	Kopal	2425925	2426465	18	+Vis	
Emberson et al. (1938)		2428903	2428920	7	Broadband-IR	Not used
Thiessen (1957)		2435374	2435942	10	yellow,blue,violet	
Larsson-Leander (1959)		2435428	2436334	121	PV	
Widorn (1959)		2435128	2436295	122	yellow,blue	Not used
Fredrick (1960)		2434761	2435903	143	Pe, 4 color	Not transformed

continued on next page

Source	Observer[†]	JD Start	JD End	N Obs.	Type[‡]	Notes
Larsson-Leander (1962)		2436457	2437023	52	PV	
Kopylov and Kumaigorodskaya (1963)		2435111	2436695	251	PV	
Mitchell (1964)					UBVRIJHKLN	Not used
Low and Mitchell (1965)					UBVRIJHKLN	Not used
Stub (1972)		2438755	2439925	220	Pe, 10 color	
Albo and Sorgsepp (1974)		2439947	2439988	144	UBV	
Albo (1977)		2440460	2440548	42	UBV	
Breger (1982; 1985; 1988)		2445646	2445972	453	UBV	Boyd, IAU
JAPOA 1983		2445239	2445409	123	UBV	
Backman et al. (1984)		2444269	2445382	107	JHKL'MNQ	
Bhatt et al. (1984)		2445044	2445798	84	BVRIJHK	
Hopkins UBV (1)		2445222	2447520	1140	UBV	

continued on next page

Source	Observer[†]	JD Start	JD End	N Obs.	Type[‡]	Notes
Flin et al. (1985)		2445065	2445937	330	UBV	
Parthasarathy and Frueh (1986)		2445208	2445426	983	UBV,ubvy	
Boyd UBV		2447066	2453457	4746	UBV	Unpublished
Chochol and Žižovský (1987)		2445043	2445664	207	UBV	
Strassmeier et al. (1999)		2450396	2450427	216	by	
Taranova and Shenavrin (2001)		2445032	2451652	243	UBVRJHKLM	Download from CDS
Hopkins UBV (2)		2452979	2455678	1836	UBV	
AAVSO BSM		2455122	present	960	BVRI	

2.3 New, modern, or unpublished data sources

2.3.1 Phoenix-10

A total of 1570 U, 1581 B, and 1595 V-band observations were collected between 1983 and 2005 by the Phoenix-10 Automated Photoelectric Telescope (APT) designed by Louis Boyd. The instrument consisted of a 10" f/6 Newtonian with a 1P21 photomultipler permanently mounted at focus. The photometer with diaphragm, filter wheels, and flip mirror were all under computer control. Detailed description of the instrumentation and software can be found in Boyd et al. (1984b). The telescope was operated from downtown Phoenix, AZ starting in 1983 and later moved to Mount Hopkins during the summer of 1986. The system was moved a second time to Washington Camp in Patagonia, AZ in 1996 where it operated until 2005.

The earliest data on ϵ Aurigae started in 1983 November and covers most of the 1983-1984 eclipse Boyd et al. (1984a). These data were published in Breger (1982; 1985; 1988; files 131, 136, and 137 respectively) covering JD 2445646 - 2455699, JD 2445701 - 2445785, and JD 2445792 - 2445972, respectively (1983 November 3 - 1984 September 29). Although the photometer was collecting data between 1984 September and 1987 September the original data have been lost due to a hardware failure (Boyd, 2010 private comm.). As far as we have been able to determine, these data were not published in subsequent publications of the IAU Archives of Unpublished Observations of Variable Stars. The next available set of data begins on JD 2447066 (1987 September 27) and ends on 2453457 (2005 March 27).

Epsilon Aurigae was observed along with a comparison (HR 1644) and check (HR 1729) star. A summary of the assumed UBV magnitudes and alternative names for these objects are summarized in Table 2.4. The observation order was KSCVCVCVCSK (K = Check, S = Sky, C = Comparison, V = Variable) iterating through the UBV filters (see Boyd et al. 1984b; table 1) with 10-second integrations.

These differential measurements were automatically corrected for extinction and transformed to the standard UBV system. Any data with an internal standard error (via. the standard deviation of the mean) of ± 20 milli-magnitudes or greater were discarded by the pipeline. Typical external errors are ± 0.011, ± 0.014, ± 0.023 mag in V, B, and U filters respectively, with mean internal errors of ± 0.005, ± 0.005 and ± 0.009 (Strassmeier and Hall 1988). The stability of the system has been satisfactory on decade-long timescales (Hall and Henry 1992, Hall et al. 1986).

Table 2.4: Star information for Boyd photometric data. Role: K = Check, S = Sky, C = Comparison, V = Variable.

Object	RA (HH MM SS)	DEC (DD MM SS)	Epoch	Role	Other Names
HD 34411	05 19 08	40 05 57	2000	K	HR 1729, SAO 40233
HD 32655	05 06 50	43 10 29	2001	C	HR 1644, SAO 40029
HD 31964	05 01 58	43 49 24	2002	V	HR 1605, SAO 39955
Sky	05 04 24	43 29 57	2003		

2.3.2 Hopkins UBV

Jeffrey Hopkins collected 811 U, 815 B, and 993 V differential magnitudes at the Hopkins Phoenix Observatory (HPO) in Phoenix, AZ. Two large blocks of data exist. The first set began on 1982 September 09 and ended on 1988 December 23. The second series started on 2003 December 04 and ended on 2011 April 25 at which time the photometric program at HPO ended.

Photometry was acquired using a home-built photometer consisting of a 1P21 photomultiplier tube operated at 950 volts. It was attached to a Celestron C-8 telescope mounted on a Meade LX-90 mount. Dead time for the detector was determined using an aperture mask. The mask contains irregularly spaced holes that reduced the aperture by 80%. A bright star and a faint star were measured

with and without the aperture mask in place. The resulting counts per each star were averaged and used to compute the dead time coefficient of the instrument.

ϵ Aurigae observations were conducted in a CSVSCSVSCSVSCS format. Each observation was composed of three 10-second integration in each of the three UBV filters. Nightly extinction coefficients were determined and applied. Color correction had been applied. After the 1980 observing season, λ Aurigae was used as the sole comparison star. The assumed magnitudes for λ Aurigae were $V = 4.71$, $(B - V) = 0.63$ and $(U - B) = 0.12$.

2.3.3 AAVSO Bright Star Monitor

Starting in 2009 October 16, ϵ Aurigae was placed on the American Association of Variable Star Observers' Bright Star Monitor (BSM) observing program. The BSM consisted of a Takahashi FS-60CB with a field flattener; 60mm f/6.2 telescope and a SBIG ST-8XME camera with Johnson/Cousins BVR_cI_c and clear filters. Data were reduced by Arne Henden at AAVSO headquarters to the standard photometric system. All color and extinction corrections were applied before data were submitted to the AAVSO database. Ongoing observations from this instrument can be found in the AAVSO database under the observer code "HQA."

2.3.4 Solar Mass Ejection Imager

For the sake of completeness, we also mention our work on data from the Solar Mass Ejection Imager (SMEI, Simnett et al. 2003). Although SMEI's primary mission is to map the large-scale variations in heliospheric electron densities by observing Thompson-scattered sunlight, it also collected precision photometry on ∼20,000 stars with $V < 8$. Through each 102-minute orbit, most regions in the sky were covered by a dozen or more frames through one of SMEI's three baffled, unfiltered CCD cameras.

The instrument was designed for 0.1% photometry and, when proper photometric extraction is performed, this precision was realized on stars brighter than 5th magnitude. On average the uncertainty on fainter stars was proportionally worse by the ratio of the star's brightness to 4th magnitude, meaning faint 8th magnitude stars still have better-than-ground photometry precision. The instrument was operational from launch until September 2011 when it was deactivated due to budget constraints. Our work with these data will be discussed in a future publication.

2.4 Calibration and mergers

The sources of photometry listed above are very inhomogeneous; consisting of multiple filters, reduction methods, observatories, instruments, and even reference star magnitudes. Although merging all of the data together clearly was not possible, one may compute offsets between observers that use the same filters. We have written a script that merges different photometry data sets. The script finds overlaps, bins the data, and then calculates the coefficients to offset/scale the data to the same system using a weighted least-squares minimization. The following equation is used:

$$A_i = a + bB_j + ct_j \tag{2.4.1}$$

where A_i is the i^{th} entry in the reference photometry, B_j is the j^{th} entry in the comparison photometry data set occurring at time t_j, a is a zero-point offset, b accounts for non-Pogson magnitudes, and c corrects for a time-dependent drift of the comparison photometry set.

In this work we have concentrated on filtered photometry in which only the linear offsets, a are required. As we have yet to consider the visual data, we have not used the b or c coefficients. Offsets to merge the various photometric sources are reported in Table 2.5.

Table 2.5: Offsets between observers. * implies no overlap existed or a manual offset was applied. *NU* means not used. "ref" indicates this was the reference photometry set for the associated column.

Source	U	B	P	V	R	I	J	H	K	L	L'	M	N	Q
1959Larsson-Leander			0.017353	0*										
1962Larsson-Leander			0	0*										
1963Kopylov			ref											
1974Albo	-0.15*	0*		0*										
1977Albo	-0.15*	0*		0*										
1983JapanAmateur	-0.204227	-0.119169		-0.08573										
1984Backman							0	0	0		ref	0	ref	ref
1984Bhatt				-0.088943	0*	0*	0*	0*	0*					
1985Flin	0			-0.054481										
1986Parthasarathy				4.701863	4.256636	3.91*								
1987Chochol	-0.106048	0		NU										
2001Taranova	NU			0	0*		0*	0*	Ref	ref		ref		
1983Boyd	6.944964	6.704575		5.955698										
1984Hopkins	-0.022894	-0.056568		-0.075453										
1987Boyd	-0.124972	-0.007964		-0.043503										
2011Hopkins	ref	-0.045311		-0.044434										
2011 AAVSO BSM		ref		ref	ref	ref								
2011 AAVSO MBE							-0.065819	-0.048444						
2012 AAVSO RTH							ref	ref						

2.5 Period analysis and results

In Figure 2.1 we show inter-eclipse UBV photometry primarily from Boyd and Hopkins. Typical internal standard errors are < 0.02 mag in all filters. On average, each observing season of ϵ Aurigae consisted of ~ 200 days of data followed by a $\sim$ 165 day block in which there were no observations. The Boyd and Hopkins data sets had several seasons of overlapping measurements which agree within uncertainties, this increased our confidence in the data collection and reduction techniques. A visual inspection of the data showed times where there are clearly visible periodic variations present (e.g. near JD 2449000), and other times where no variations appeared (e.g. JD 2450500-2451000). The sudden spike of $\Delta U = 0.2$, $\Delta B = 0.1$ and $\Delta V = 0.7$ between JD 2446736 - 2446737 might have been a flare.

Figure 2.2 shows the 2009-2011 eclipse in $UBVRIJH$ photometric filters as observed by Hopkins, the AAVSO BSM, and other AAVSO collaborators. All filters, save V, have been offset by an arbitrary amount for display purposes. All bands showed the typical eclipse shape: a near-linear decrease of ~ 0.7 mag during ingress, the flat in-eclipse phase, followed by a sharp rise into egress. The OOE variations were superimposed on this profile as $\sim$ 60-day variations with a maximum amplitude of $\Delta U = 0.1$, decreasing in amplitude at longer wavelengths. Notice this eclipse did not feature any significant mid-eclipse brightening as was thought to exist in the 1983 eclipse data.

The photometry between JD 2455400 - 2455600 implied that the eclipse depth was slightly wavelength-dependent. Indeed, the U-band photometric plot during this interval was sloped downward, whereas the H-band plot had a slight upward slope. This may be, in part, due to a change in opacity caused by molecules or other material in the line of sight that have recently sublimated from grains of material on the F-star side of the disk (e.g. CO, Stencel et al. 2011).

As the out-of-eclipse variations clearly were not periodic, searching for periods using traditional Fourier-based methods would likely fail. Instead, we used the WWZ algorithm to find dominant periods. The WWZ is essentially a time-dependent, windowed Fourier transform. Unlike a windowed Fourier transform, the WWZ convolves the underlying sinusoid with a decaying exponential. This decreases the impact of data far away from the current "time window center." Akin to the output of a Fourier transform, the output of a WWZ shows the power associated with a particular frequency and time.

We have processed the inter-eclipse data (JD 2446000 - 2455000) from Boyd and Hopkins using *WinWWZ* with a decay constant of $c = 0.0125$. In Figures 2.3, 2.4, and 2.5 we show the WWZ output for U, B, and V photometric filters, respectively. In addition to the WWZ output (color background), we have also plotted the maximum WWZ coefficient as a function of time using white dots. Because the APT-10 was not operational during the interval JD 2449500 - JD 245000, we blocked out the WWZ result in this region. We caution the reader that WWZ results within < 200 days of this interval may be artificial. We have also intentionally limited the z-scale (color) to 100 in the U and B plots to assist with comparison to the V-band data.

In general there was good agreement between the WWZ output between filters which attests that the variations, although slightly wavelength dependent, are a global property of the system. Inspection of the U-band photometric data revealed the variations are strongest in U-band (decreasing in amplitude towards longer wavelengths), therefore we will discuss the U-band data below noting any significant differences between the B and V results as necessary.

Figure 2.3 shows 12 peaks with WWZ output greater than 40. Of these, the peaks at $(8977, 102.7)$ and $(12259, 87.9)$ (hereafter the "upper track") appeared most dominant. These periods were spaced apart by 3282 days with $\Delta P = -14.8$ days. It was easily seen that the earlier of these two peaks is absent from the B and V-

band WWZ plots. The WWZ value was determined by a χ^2-like metric, therefore the additional noise in the B and V-band data at these intervals diminished the strength of the period signature.

In addition to the high WWZ output the radial velocity changes as these times were nearly in phase with the photometric variations. Combined with the fact that the spacing of the peaks was 1/3 of the orbital period, we were led to believe that these events should be regarded as significant.

Operating on the assumption that these peaks provided a glimpse of period evolution in the F-star, we intentionally sought variations following a parallel evolutionary path. Three peaks located at $(7166, 90)$, $(10492, 82.7)$, and $(13744, 68.9)$ (hereafter the "lower track") followed a similar evolution. Like the "upper track," these peaks were separated by nearly 1/3 of an orbital period.

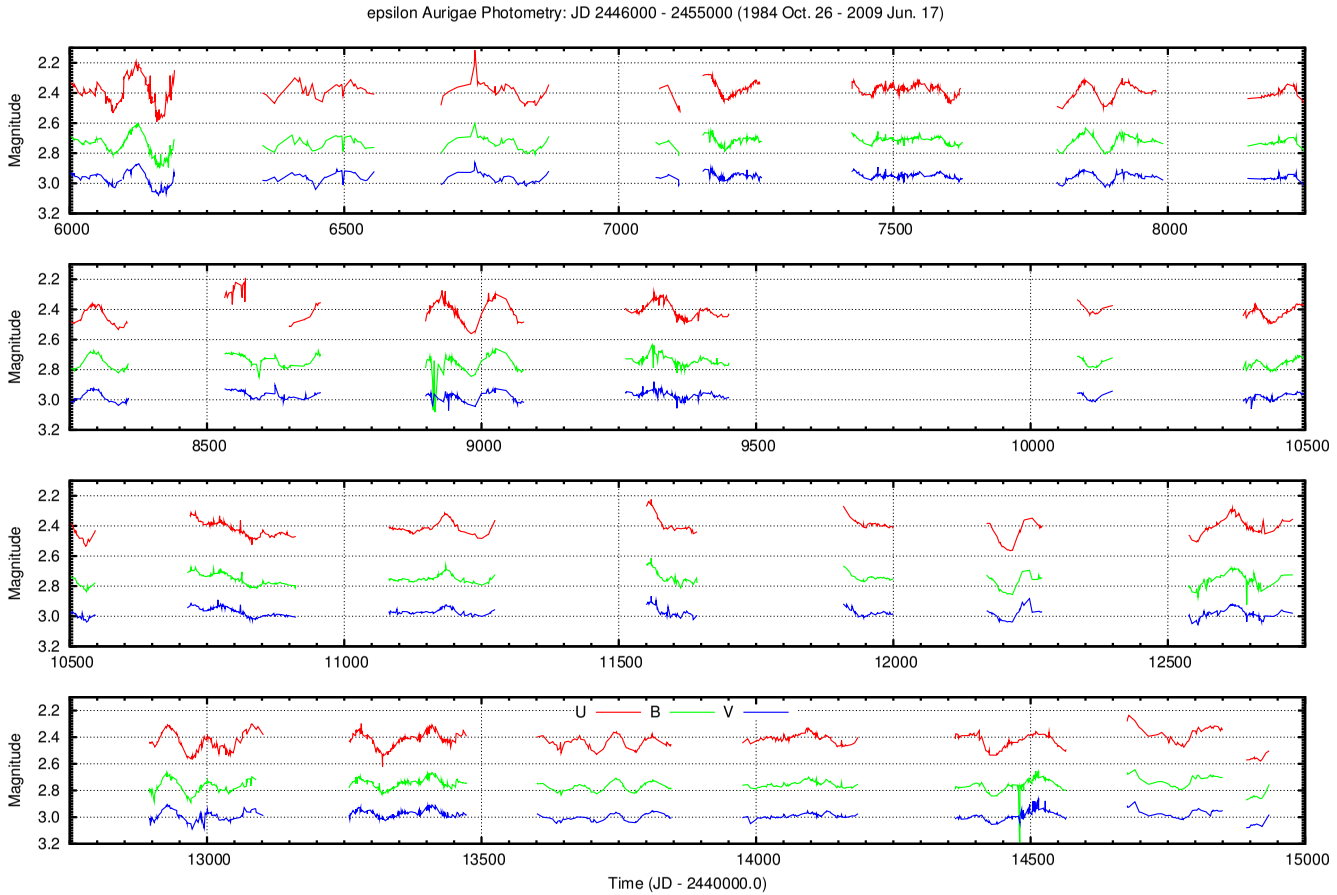

Figure 2.1: Inter-eclipse UBV photometry, JD 2446000-2455000 (1984 Oct. 26 - 2009 Jun. 17) from the Boyd and Hopkins data sets. All data are plotted as observed. Uncertainties (not plotted) are typically 20 mmags or less.. The observing windows consist of about 200 days of data followed by 165 day gaps. During the interval 2449500 - 2450000 the APT-10 photometer was not operational. The out-of-eclipse variations have amplitudes of ~ 0.1 mag in U and ~ 0.05 in V with characteristic timescales of 60-100 days. The sudden brightening seen around JD 2446736 - 2446737 might be a flare.

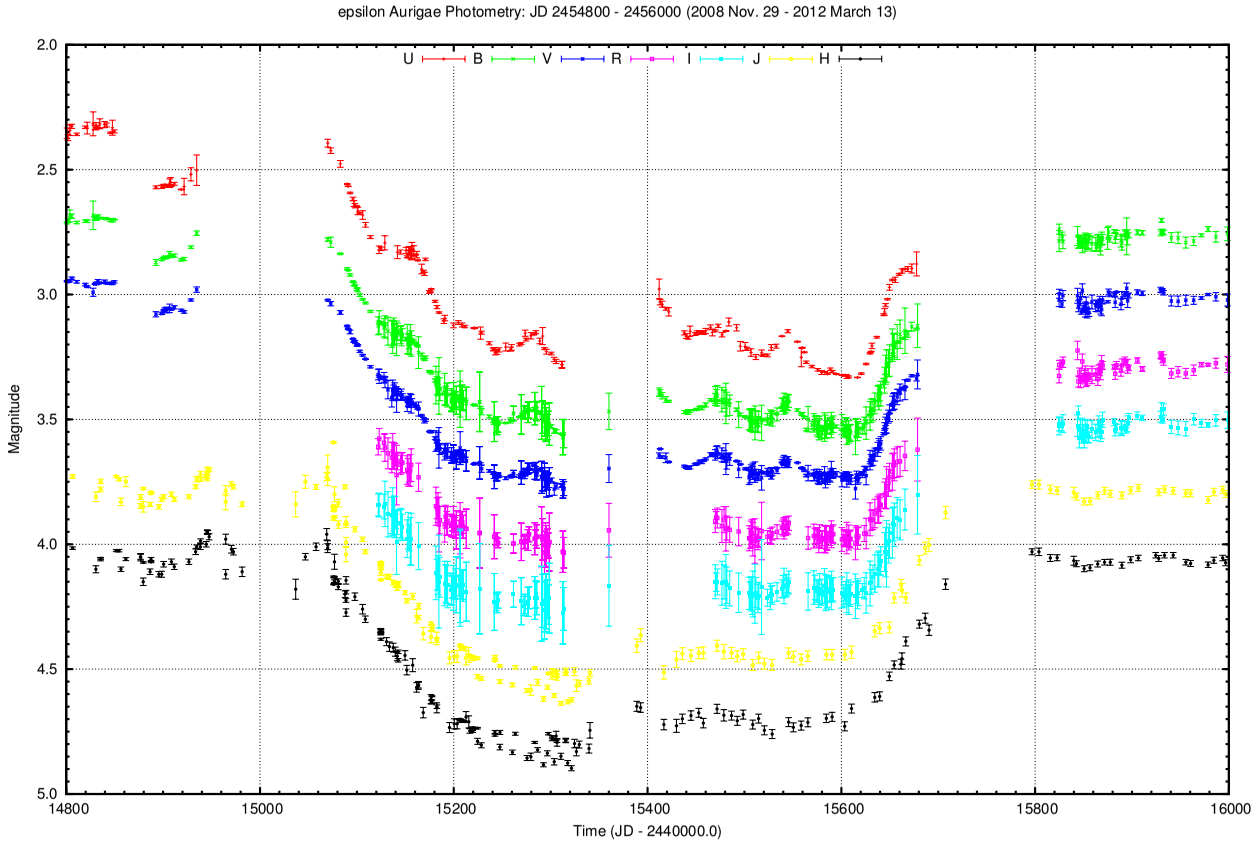

Figure 2.2: 2009-2011 eclipse of ϵ Aurigae in $UBVRIJH$ filters, JD 2454800-2456000 as measured by Hopkins (UBV), the AAVSO BSM ($BVRI$) and AAVSO observers Brian McCandless and Thomas Rutherford (JH data). The V-band data is plotted as observed, all other filters have been offset by an arbitrary amount for display purposes. The eclipse may be represented by a linear decrease in brightness by ~ 0.7 mag, followed by a flat minimum and then a sharp rise back to out-of-eclipse brightness. The out-of-eclipse variations are superimposed on this profile and result in 60-100 day cycles with characteristic amplitudes of ~ 0.1 mag in U, decreasing in amplitude towards longer wavelengths. Notice during second half of eclipse the U-band light curve slopes downward, whereas the H-band has an upward slope. This attest that the eclipse has wavelength-dependent extinction.

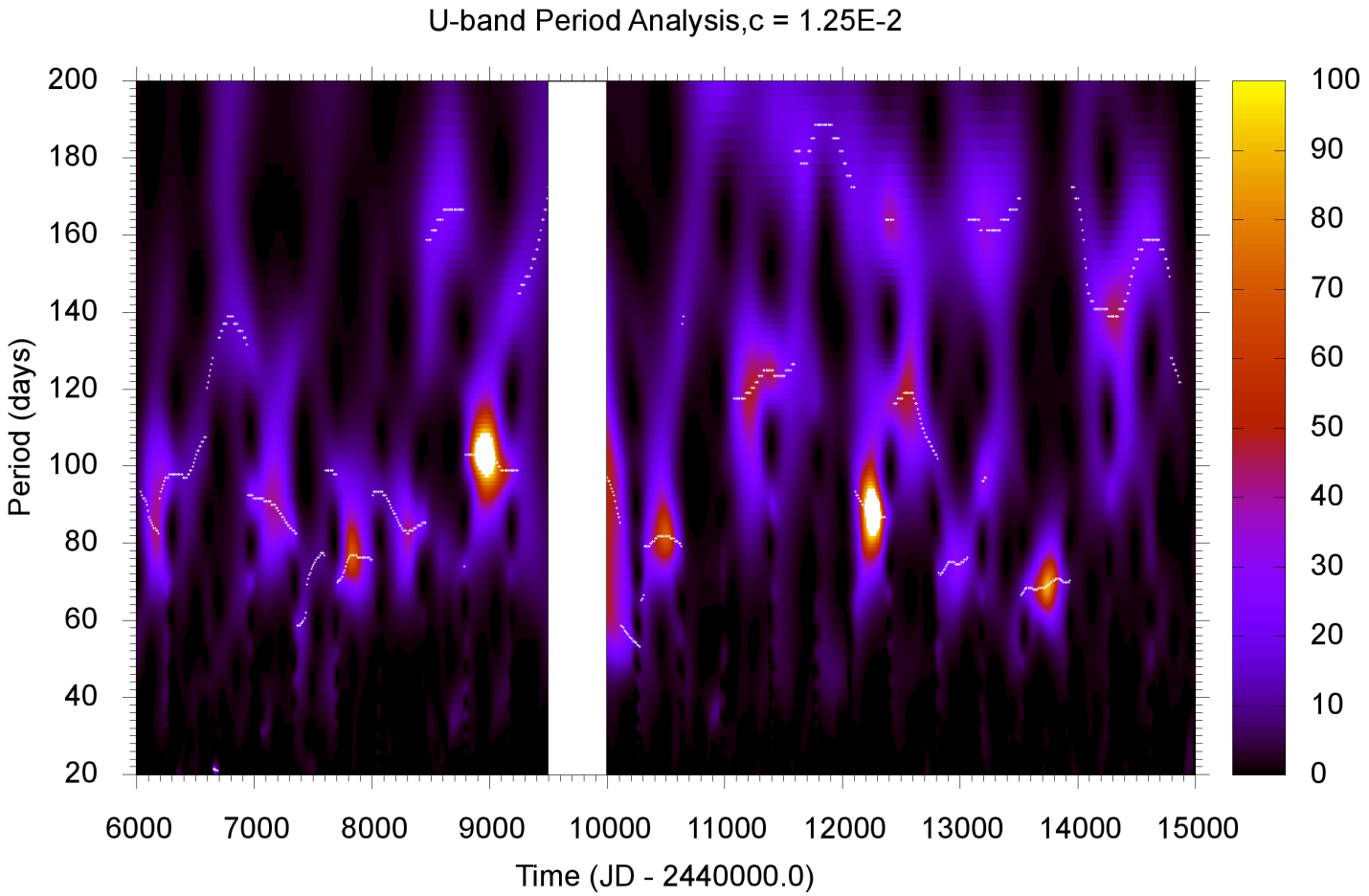

Figure 2.3: U-band WWZ period analysis. The color indicates power associated with a given period at a particular time. See text for discussion of dominant periods.

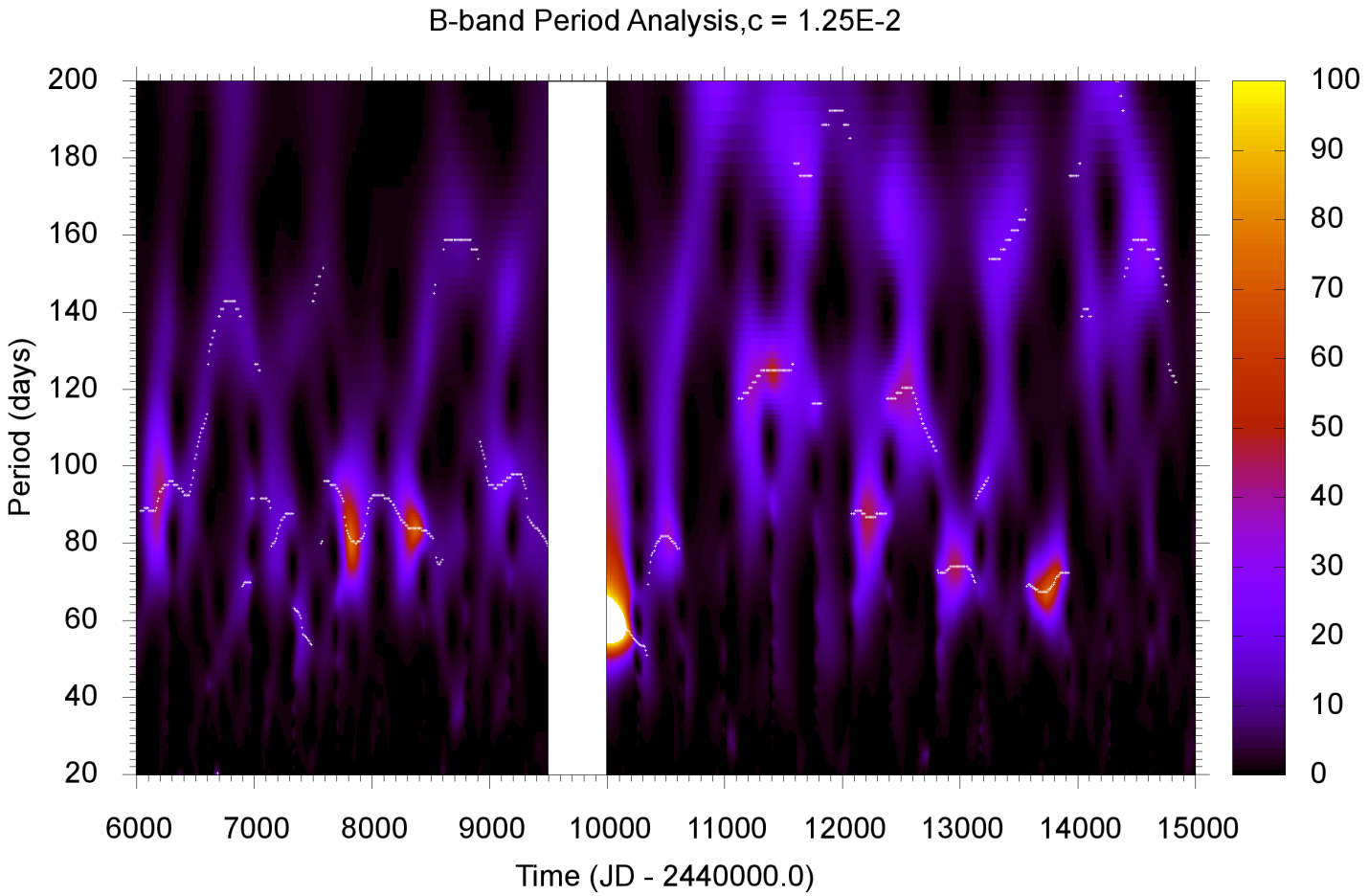

Figure 2.4: *B*-band WWZ period analysis. The color indicates power associated with a given period at a particular time. See text for discussion of dominant periods.

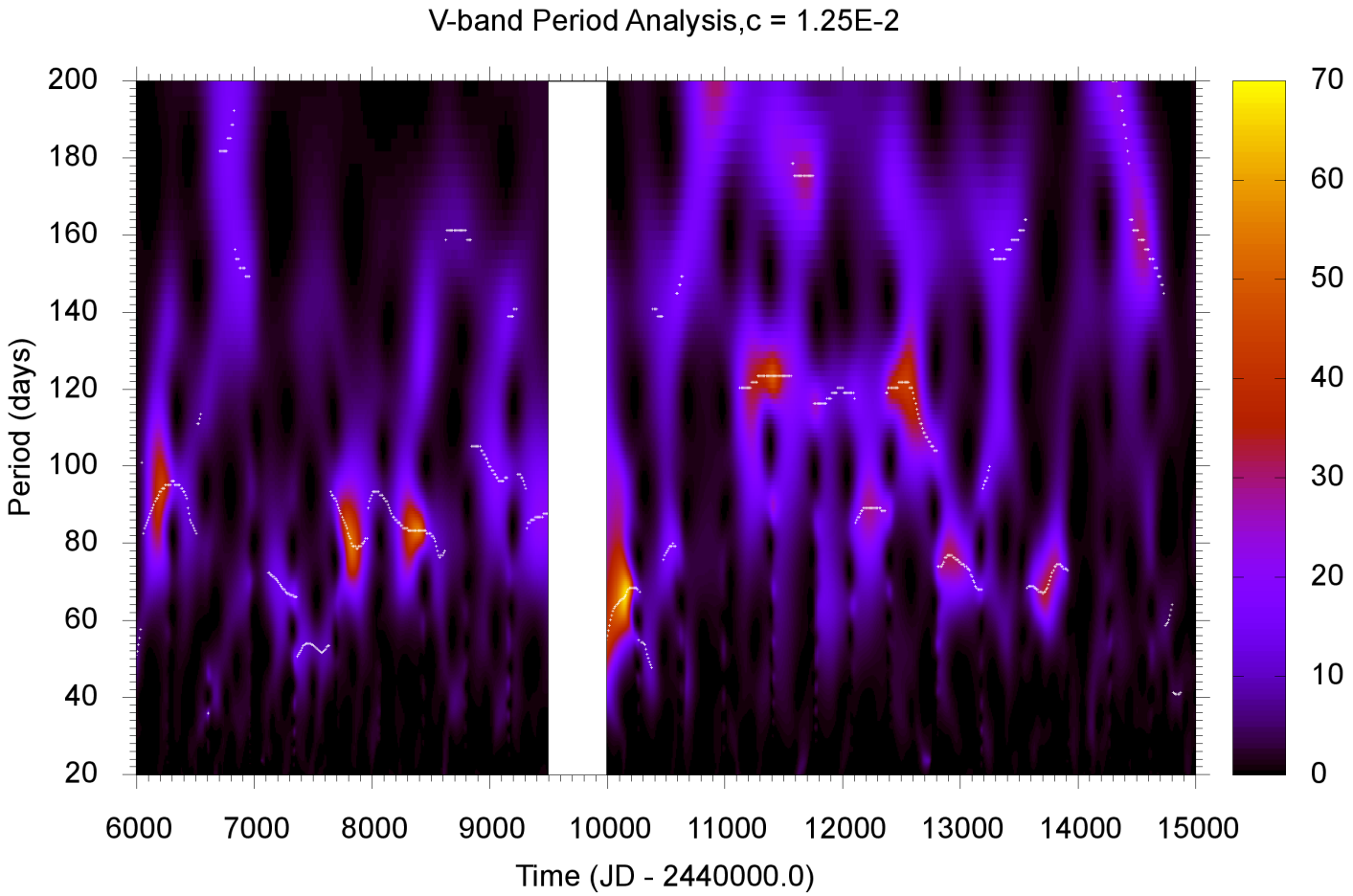

Figure 2.5: V-band WWZ period analysis. The color indicates power associated with a given period at a particular time. See text for discussion of dominant periods.

At the time of this writing, a consistent asteroseismic interpretation for evolved supergiant-class stars does not exist due to the uncertainties underlying the theoretical calculations of mixing theory and radiation pressure (Aerts et al. 2010; Ch. 2). Therefore, we cannot provide a rigorous, quantitative interpretation of the periods which we have observed. Instead we interpreted these results qualitatively in terms of observed supergiant and post-AGB behavior.

The "upper track" evolved at a rate of $\Delta P = -1.6$ day/year whereas the lower track changed at a slightly lower rate of $\Delta P = -1.2$ day/year. Assuming that these trends were indicative of evolutionary changes in the F-star, we predicted the dates and periods of stable variation features in Table 2.6. Near the end of the 2009-2011 eclipse a sawtooth-like pattern with $61 - 76$ day periods developed (see Figure 2.2). This is tantalizingly close to the ~ 73 day period we predicted would develop at this time.

It was instructive to compare the variations seen in ϵ Aurigae with those observed or predicted for "recently evolved" supergiants and "much older" post-AGB stars. It had been known for some time that stars near the F0Ia spectral and luminosity class show low-level variations with 0.015 - 0.025 mag amplitudes in the V-band (Maeder 1980). An investigation of 24 super- and hyper-giant stars using HIPPARCOS photometry by van Leeuwen et al. (1998) showed that all of these B to late-G stars exhibited photometric changes that were not strictly periodic. Indeed, many of these "periods" would be better described as "quasi-" or "pseudo-periods". Across this region of the HR diagram, stars tended to show variations on 10 to 100 day timescales.

Indeed, in this respect ϵ Aurigae could easily be regarded as a recently-evolved supergiant. Several stars in van Leeuwen et al.'s sample were a close match for ϵ Aurigae: At a slightly higher temperature, HIP 25448 (A8:Ia+) has $\Delta VT = 0.1$ mag variations with several short periods in the 8-40 day interval, and two longer

periods at 146 and 182 days. The slightly cooler HIP 25892 (F5Ia) had two equally significant periods at 48 and 84 days with photometric variations between 0.01 and 0.05 mag in ΔVT. HIP 42570 was the closest match to ϵ Aurigae in the van Leeuwen et al. sample. This star showed quasi-periods at 53, 80, and 160 days with variations of 0.06 mag.

Observational evidence of several carbon-rich post-AGB objects by Hrivnak et al. (2010) have established a relationship between effective temperature and period. From this empirical relationship, one would anticipate ϵ Aurigae to exhibit pulsations on a $\sim$ 40-day timescale, a factor 2-3 less than what we have determined above. Therefore we do not characterize the observed photometric behavior in ϵ Aurigae to be similar to post-AGB objects.

Table 2.6: Predicted dates of stable variations and observed periods for ϵ Aurigae

Upper Track			Lower Track		
JD	Period	Observed?	JD	Period	Observed?
2396465	340		2397831	249	
2399747	325		2401120	239	
2403029	310		2404409	228	
2406311	295		2407698	218	
2409593	280		2410987	207	
2412875	266		2414276	196	
2416157	251		2417565	186	
2419439	236		2420854	175	
2422721	221		2424143	165	
2426003	206		2427432	154	
2429285	192		2430721	144	
2432567	177		2434010	133	
2435849	162		2437299	123	
2439131	147		2440588	112	
2442413	132		2443877	102	
2445695	118		2447166	90.0	Y
2448977	102.7	Y	2450492	82.7	Y
2452259	87.9	Y	2453744	68.9	Y
2455541	73		2457026	66	
2458823	58		2460308	52	
2462105	43		2463590	37	
2465387	29		2466872	22	
2468669	14		2470154	7	

2.6 Conclusions and next steps

In this chapter we reported on digitization efforts of 27 sources of historical photometry from 81 different observers. We also reported two unpublished sources of UBV photometric data that, when combined, resulted in an impressive 27 years worth of photometric coverage of ϵ Aurigae.

We analyzed the out-of-eclipse UBV photometry using a WWZ transform. In the U-band data, we found that there are two tracks of evolving periods. Within each track, stable pulsations manifest at ∼3300-day intervals (1/3 orbital period). Following the evolution of what we call the "lower track," we predicted, for the first time, the development of stable variational patterns that occurred during the second-half of the 2009-2011 eclipse.

As a consistent asteroseismic theory for supergiant and post-AGB stars has yet to be published, we are unable to make a fully quantitative assessment of our work. Instead we qualitatively compared the periods observed in ϵ Aurigae with observationally determined supergiant and post-AGB behavior. Our "upper track" manifested in stable 102- and 88-day variation patterns, whereas the lower-track showed 90, 82, and 69-day periods. Post-AGB stars of a similar temperature and luminosity were expected to exhibit periods in the ∼45-day range. Supergiants, on the other hand, show periods in almost perfect agreement with what we have derived here. Therefore we qualitatively conclude that ϵ Aurigae is more likely a supergiant than a post-AGB star based upon its variational pattern.

We encourage continued photometric monitoring of this system for the next several decades to test the predictions in Table 2.6. We also suggest a WWZ-based period analysis be conducted on historic radial velocity measurements (i.e. those found in Stefanik et al. 2010) to see if any trends similar to those discovered here exist in those data as well.

Chapter 3

Interferometry of ϵ Aurigae

In this chapter I present a series of interferometric observations of ϵ Aurigae that occurred mostly during the $2009 - 2011$ eclipse. This work extends on the initial Kloppenborg et al. (2010) and updated Kloppenborg et al. (2011) interferometry reports. The first few sections are designed to acquaint the reader with the terminology and data products of modern optical interferometers. Mid-way through there is a quick discussion of Bayesian statistics and how they can be used in model selection and parameter estimation. The two principal software products of this dissertation are presented in conjunction with the data, images, and models for the F-star and eclipsing object. All of the data discussed in this chapter are provided electronically in the supplementary files associated with this manuscript.

3.1 Introduction

The study of astrophysical objects is primarily limited by two factors: the quantity of light gathered by the primary aperture, and the resolving power of the instrument. The light gathering capabilities of an instrument clearly increases proportional to the surface area of the primary aperture, whereas the resolving power grows according to the Rayleigh Criterion:

$$\theta = \frac{\lambda}{D} \tag{3.1.1}$$

where θ is the resolution (in radians), λ is the wavelength of observation, and D is the diameter of the aperture. At present the largest telescopes on Earth are a pair of 10.4 m segmented mirrors at the Keck Observatory on Mauna Kea. Each aperture provides a maximum resolution of about 40 milli-arcseconds (*mas* hereafter) at 1.6μm neglecting the effects of the atmosphere. The next generation instrument, like the Giant Magellan Telescope, will more than double the aperture diameter, permitting targets four-times fainter and nearly 20 *mas* in size to be resolved.

Yet even with these giant telescopes, many of the physical processes of stars and stellar environments will remain out of reach. To study the inner regions of YSOs, astrophysical disks, stellar features (e.g. spots, limb darkening, non-radial pulsation, and gravity darkening), the processes of mass loss and accretion, all require angular resolutions of one *mas* or better. To obtain this resolution from a single or segmented mirror telescope, apertures of 100 meters with aggressive adaptive optics would be required. Such a large optical device is both technologically and economically unfeasible at this time.

Interferometry is a potential solution to this issue. An interferometer permits the light from one or more telescopes to be combined, effectively creating a mirror with a diameter equal to the spacing between the two most distant apertures. In fact, interferometers not only meet the Rayleigh criterion, they exceed it by a factor of two! In the next few sections I will outline the basics of interferometry focusing on the interferometric observables, and terminology.

Figure 3.1: An idealized interferometer consisting of two telescopes separated by some distance $\vec{B}$. The path length, $d = \vec{s} \cdot \vec{B}$, is compensated by a delay line of length $d/2$.

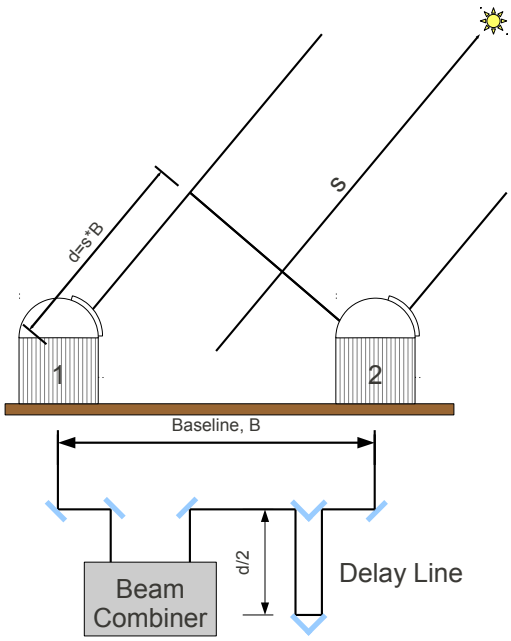

3.2 Interferometric observables and terminology

Unlike single aperture telescopes, interferometers do not yield "images" of the source they are observing. Instead, they provides measurements of interference patterns that corresponds to the Fourier transform ("FT" hereafter) of the source modulated by the instrumental spectral response, bandwidth, and atmospheric conditions. Comprehensive overviews of all topics presented in this section can be found in Lawson (2000), Labeyrie et al. (2006), and Glindemann (2011). In the next few paragraphs, I will summarize much of Chapter 2 from Lawson (2000) which discusses observations of a monochromatic and polychromatic source with an idealized interferometer.

Figure 3.1 represents a vastly oversimplified interferometer consisting of two identical apertures separated by a distance $b = |\vec{B}|$. Here the *baseline* is defined as the vector between the two apertures, $\vec{B} = \vec{x_1} - \vec{x_2}$, where $\vec{x_i}$ is a three-vector in the local reference frame of the interferometer. The interferometer is observing a source in the $\hat{s} = \vec{S}/|\vec{S}|$ direction at a distance $>> b$.

3.2.1 Unresolved monochromatic and polychromatic sources

Ignoring any effects of the atmosphere, when the monochromatic wavefront reaches each aperture in a two-telescope interferometer, each will record a phase of:

$$\phi_1 \sim e^{-i\frac{\omega}{c}\hat{s}\cdot\vec{B}}e^{i\omega t} \tag{3.2.1}$$

$$\phi_2 \sim e^{i\omega t} \tag{3.2.2}$$

$$\tag{3.2.3}$$

respectively. This shows that the phase of the advancing wavefront is dependent on differential path length $d = \hat{s}\cdot\vec{B}$ which, in turn, depends on the baseline and viewing angle. By directly combining the two beams we may derive the time-averaged power recorded by a detector (Lawson 2000; Eq. 2.3):

$$P = 2AF(1 + \cos k(\hat{s}\cdot\vec{B} + d_1 - d_2)) \tag{3.2.4}$$

$$= 2AF(1 + \cos kD), \tag{3.2.5}$$

where F is the source flux density, A is the aperture area, and $D = \hat{s} \cdot \vec{B} + d_1 - d_2$ is the relative delay between the two baselines. This function is plotted in Figure 3.3(a). Notice that this *interference pattern* is strictly periodic with an amplitude of $2AF$.

For a polychromatic source that passes through a "boxcar" filter with constant throughput η_0, mean wavelength λ_0 and bandwidth $\Delta\lambda$, the power as a function of relative delay is (Lawson 2000; Eq. 2.7):

$$P = 2AF_{\lambda-0}\eta_0\Delta\lambda\left[1 + \frac{\sin\left(\pi\Delta\lambda/\lambda_0^2 D\right)}{\pi\Delta\lambda/\lambda_0^2 D}\cos\left(k_0 D\right)\right] \quad (3.2.6)$$

$$= 2AF_{\lambda-0}\eta_0\Delta\lambda\left[1 + \frac{\sin\left(\pi D/\Lambda_{coh}\right)}{\pi D/\Lambda_{coh}}\cos\left(k_0 D\right)\right], \quad (3.2.7)$$

where $\Lambda_{coh} = \Delta\lambda/\lambda_0^2$ is the *coherence length* of the $\mathrm{sinc}(x) \equiv \sin(x)/x$ modulation. This function, is plotted in Figure 3.3(b). Typically the term in square brackets, called the *fringe envelope*, can be written as:

$$1 + M(\Lambda_{coh}, D)\cos\left(k_0 D\right), \quad (3.2.8)$$

where $M(\Lambda_{coh}, D)$ is the fringe modulation function.

3.2.2 Resolved sources

Interferometric observations of resolved and extended sources take advantage of the flux on the object, as a function of position, being incoherent. By the principle of superposition, the total power can be computed as a sum of infinitesimal point sources.

Figure 3.2: Monochromatic and polychromatic interference patterns.

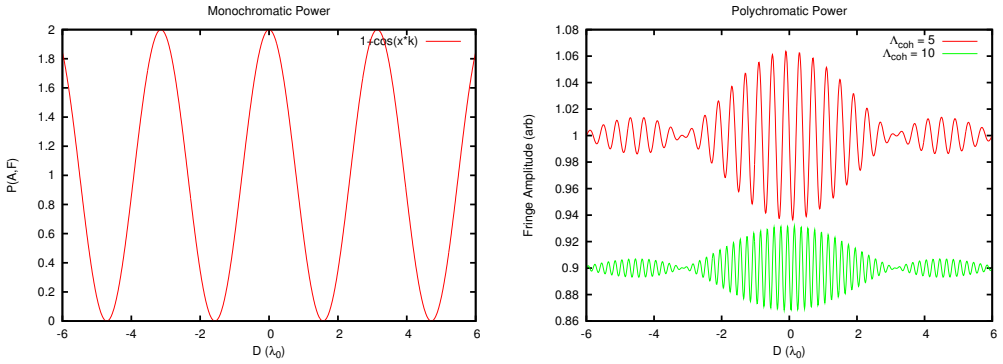

(a) (b)

Let $\hat{s}_0$ be the position of the phase tracking center of baseline $\vec{B}$, about which position $\hat{s}$ is observed to have flux $F(\hat{s})$. If the instrumental throughput is characterized by $A(\hat{s}, \hat{s}_0)$, then the power observed will be (Lawson 2000; Eq. 2.11):

$$P(\hat{s}_0, \vec{B}) = \int A(\hat{s}, \hat{s}_0) F(\hat{s}, \hat{s}_0)(1 + M(\Lambda_{coh}, \Delta D)\cos(k_0 \Delta s \cdot \vec{B}))d\Omega \quad (3.2.9)$$

$$= \int A(\Delta s) F(\Delta s)(1 + \cos(k_0 \Delta s \cdot \vec{B}))d\Omega \quad (3.2.10)$$

where $d\Omega$ is solid angle. The above equation may be rewritten in terms of *spatial frequencies* $u \equiv \frac{B_x}{\lambda}$ and $v \equiv \frac{B_y}{\lambda}$:

$$V(u, v) = \int A(\alpha, \beta) F(\alpha, \beta) e^{2\pi i(\alpha u + \beta v)} d\alpha d\beta, \quad (3.2.11)$$

where $V(u, v)$ is the *complex visibility* of the source. The astute reader will recognize $V(u, v)$ as the Fourier transform (FT hereafter) of the brightness distribution, $F(\alpha, \beta)$, on the sky. In this way, interferometers observe in the Fourier plane. This exact relationship between the brightness pattern and the visibility is the *Van Cittert-Zernike theorem.*

3.2.3 Analytic visibility functions

If a source is observed interferometrically, it is often desired to derive the geometrical and/or physical properties of the target. Some brightness distributions have complex visibility functions that may be computed analytically. Several of these *analytic visibility functions* have been derived and can be found in (many) interferometry texts. Therefore below I summarize only two special cases to demonstrate the properties of a few interferometric observables.

Point source

For a delta function centered at (α, β) away from the pointing position (α_0, β_0):

$$I(\alpha, \beta) = \delta(\alpha - \alpha_0, \beta - \beta_0), \tag{3.2.12}$$

the FT is trivially obtained:

$$V(u, v) = e^{-2\pi i(u\alpha_0 + v\beta_0)} \tag{3.2.13}$$

Uniform disk (circle)

Few astronomical objects are simple point sources. Moving into two dimensions, the simplest representation of a star is a circle of uniform brightness. This *uniform disk* has a simple FT:

$$V(u, v, \theta\lambda) = \frac{2J_1\left(\pi\theta|\vec{B}|/\lambda\right)}{\pi\theta|\vec{B}|/\lambda}, \tag{3.2.14}$$

where θ, often called the *uniform disk diameter* or UDD, is the diameter of the star, $|\vec{B}| = \sqrt{u^2 + v^2}$, and J_1 is a Bessel function of the first kind. The square of this function is plotted for several different diameters in Figure 3.3. As once can

Figure 3.3: Visibilities from uniform disks of various diameters.

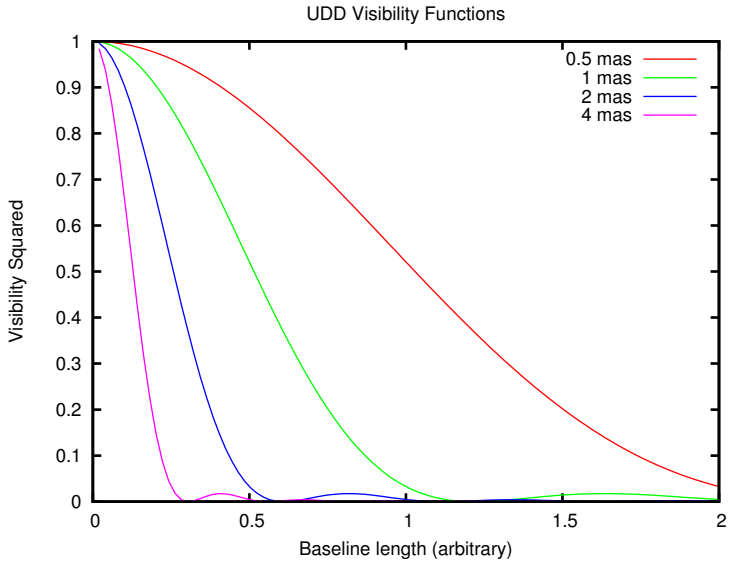

see, stars of greater diameter have lower visibilities as a function of baseline length. Larger stars are said to be more *resolved* than their smaller counterparts.

Other sources

Visibility functions, being complex quantities, obey the principle of superposition. Therefore complicated models consisting of multiple emitting sources are easily computed; however, one must use caution when applying this principle because flux is a positive definite quantity, whereas superposition could create negative flux.

Consider an eclipsing binary system. At most times, the system may be modeled by superimposing the visibility functions of the individual components, but whenever an eclipse happens, the flux contribution from the obscured portion goes to zero. In this case, the model for the *eclipsed* component must be modified to account for the fractional coverage induced by the *eclipsing* object. For the simplest geometries this is a trivial task; however for complex sources it may be easier to render an image of the object, then compute the complex visibility using a numeric FT method, like a discrete Fourier transform or non-uniform fast Fourier transform instead.

3.3 Optical interferometric data products

For current generation optical interferometers, it is possible to form seven data products which this section describes in detail. Although all of these products can be generated by interferometric arrays with four or more telescopes, only a subset are used in practice. A common data format, called the Optical Interferometry Exchange Format (OIFITS, Pauls et al. 2005) is used for storing reduced optical interferometric data. The OIFITS format is managed and endorsed by the International Astronomical Union working group on Optical Interferometry. Currently only a subset of the interferometric data products have official storage mechanisms.

3.3.1 UV coordinates

As discussed above, interferometric observations occur in complex space, therefore the coordinates of an observation are specified by three vectors, (u, v, w). The so-called UV plane is oriented perpendicular to direction of the source in the $\hat{s}$ direction (i.e. in the "plane" of the sky) with u corresponding to astronomical North. Because of projection effects, two transformations are required to convert the local reference frame of the interferometer (North, East, Up) into UV coordinates.

Let the (x', y', z') coordinate system denote the local topocentric coordinate system, (East, North, Altitude), respectively. To transform into the standard array coordinate system (x, y, z) where x points towards the intersection of the meridian and Celestial Equator, y points East, and z is towards the North Celestial Pole[1], the following transformation is applied:

$$\begin{bmatrix} x \\ y \\ z \end{bmatrix} = \begin{bmatrix} 0 & -\sin(\delta) & \cos(\delta) \\ 1 & 0 & 0 \\ 0 & \cos(\delta) & \sin(\delta) \end{bmatrix} \begin{bmatrix} x' \\ y' \\ z' \end{bmatrix} \tag{3.3.1}$$

where δ is the declination of the observed object (note, this is a correction to a typesetting error in Lawson 2000). The complex coordinates (u, v, w), require yet another transformation because w is directed towards the star, v is perpendicular to w along the great circle from the star to the NCP, and u is perpendicular to the other two axes. The transformation is thus:

$$\begin{bmatrix} u \\ v \\ w \end{bmatrix} = \begin{bmatrix} \sin(H) & \cos(H) & 0 \\ -\sin(\delta)\cos(H) & \sin(\delta)\sin(H) & \cos(\delta) \\ \cos(\delta)\cos(H) & -\cos(\delta)\sin(H) & \sin(\delta) \end{bmatrix} \begin{bmatrix} x \\ y \\ z \end{bmatrix}. \tag{3.3.2}$$

After applying these rotations, one will find that the path of the UV coverage at a constant declination is an ellipse centered at $(u, v) = (0, z\cos(\delta))$ with a semi-major axis of $\sqrt{x^2 + y^2}$:

$$u^2 + (v - z\cos(\delta)/\sin(\delta)) = x^2 + y^2 \tag{3.3.3}$$

[1]The North and South Celestial Poles are defined to be the projection of Earth's rotational North and South poles into space.

Figure 3.4: High (left) to low (right) contrast fringes which would result in high to low visibilities. Image credit: ESO, file 0111e

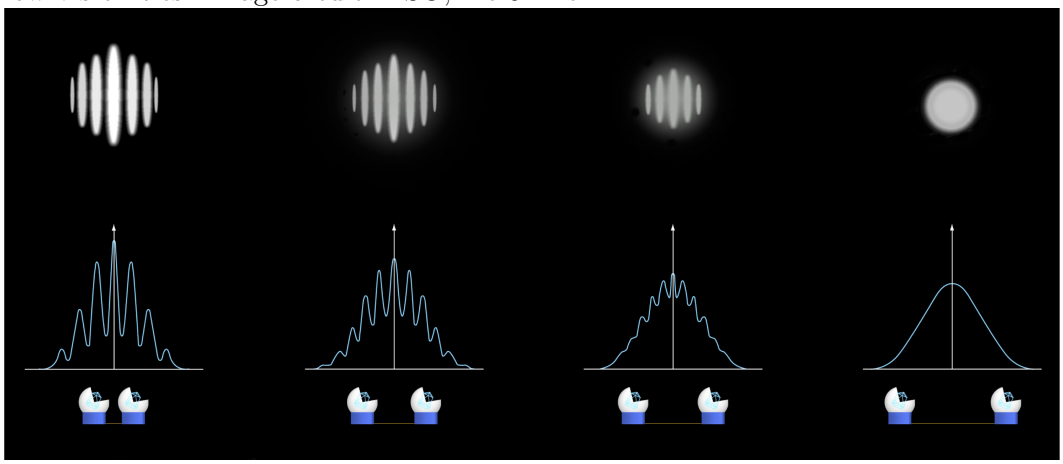

It is worth noting that the (North, East, Up) coordinates reported by a surveyor are not in alignment with the astronomical equivalents because surveyor North might be as much as few degrees away from astronomical North.

3.3.2 Visibility

Complex visibility is a principle interferometric observable. Unfortunately, turbulence in the atmosphere prevents the phase (and hence the complex visibility) from being directly measured. Fortunately, the amplitude of the complex visibility, simply called the *visibility*, is easily observed. The visibility is a measurement of fringe contrast defined in terms of the minimum and maximum fringe intensities:

$$V = \frac{I_{\max} - I_{\min}}{I_{\max} + I_{\min}}.$$

A sample of high to low contrast (high to low visibility) fringes are shown in Figure 3.4. Because of noise, the visibility is often squared, yielding the *visibility squared* or V^2.

Figure 3.5: Closure phase is formed by summing the phase around a closed triplet of telescopes. The differential phase introduced by atmospheric disturbances are canceled out.

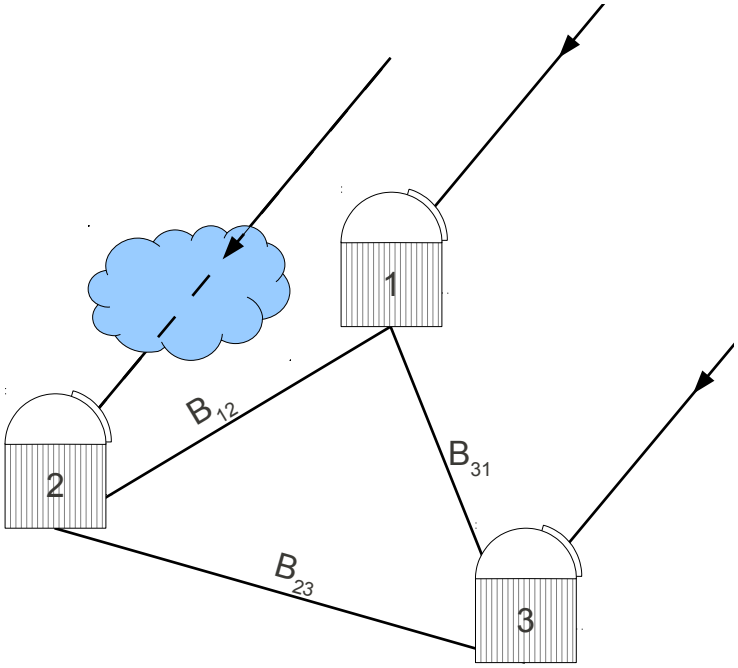

3.3.3 Closure phase and the bispectra

Until the a method for removing the aforementioned atmospheric distortions is found, optical interferometers cannot directly measure the complex visibility on a baseline with much certainty. Instead, the idea of *closure phase* was suggested in the early stages of radio interferometry (Jennison 1958), and later implemented in optical interferometers. Consider a three telescope interferometer as depicted in Figure 3.5. Let one telescope receive an additional phase offset, ϕ_{atm}, due to atmospheric turbulence. The phase offset introduced on baseline $1-2$ will be equal in magnitude to that on baseline $2-3$, but of opposite sign. Therefore the measured phases are

$$\phi'_{12} = \phi_{12} + \phi_{atm} \tag{3.3.4}$$

$$\phi'_{23} = \phi_{23} - \phi_{atm} \tag{3.3.5}$$

$$\phi'_{31} = \phi_{31}. \tag{3.3.6}$$

Therefore, the sum of the phases around the triplet of telescopes is:

$$\phi_{123} = \phi'_{12} + \phi'_{23} + \phi'_{13} \tag{3.3.7}$$

$$\phi_{123} = \phi_{12} + \phi_{atm} + \phi_{23} - \phi_{atm} + \phi_{31} \tag{3.3.8}$$

$$= \phi_{12} + \phi_{23} + \phi_{31}. \tag{3.3.9}$$

The number of closure phases in an N-telescope interferometer is determined using the binomial coefficient,

$$\frac{n!}{k!(n-k)!} = \binom{n}{k}. \tag{3.3.10}$$

Although there are $\binom{N}{3}$ closure phases, only $\binom{N-1}{2}$ of them are independent (Monnier 2007).

The closure phase is normally encoded in a quantity called the *bispectra* (colloquially called the "T3" or "triple product"). The bispectra can be formed in two ways. First it may be measured directly by determining the amplitude and phase of the interference pattern formed by a closed loop of three telescopes. In this case, the bispectra is defined by the triple product of the underlying complex visibilities:

$$B_{ijk} = V_{ij} V_{jk} V_{ki}. \tag{3.3.11}$$

Notice the order of the the indicies matters, as the triplet of telescopes must be traversed in one direction. Alternatively, the visibility amplitudes and closure phases can be measured on each baseline baseline independently. Then the bispectra is formed *via*:

$$B_{ijk} = |V_{ij}||V_{jk}||V_{ki}|e^{i\left(\phi_{ij}+\phi_{jk}-\phi_{ki}\right)}. \tag{3.3.12}$$

The first method is preferred as it provides an independent measurement of the bispectra's amplitude, whereas the second method introduces a degeneracy between the visibilities and bispectra.

3.3.4 Closure amplitudes

The second to last interferometric product I wish to discuss is the *closure amplitude*. This quantity is often used in radio astronomy as it is independent of fluctuations in telescope-specific gains, G_i. If a quartet of telescopes with indicies i, j, k, and l are used to observed a source, then the closure amplitude is formed by:

$$A_{ijkl} = \frac{|V_{ij}^{measured}||V_{kl}^{measured}|}{|V_{ik}^{measured}||V_{jl}^{measured}|} \tag{3.3.13}$$

$$= \frac{|G_i||G_j||V_{ij}^{true}||G_k||G_l||V_{kl}^{true}|}{|G_i||G_k||V_{ik}^{true}||G_j||G_l||V_{jl}^{true}|} \tag{3.3.14}$$

$$= \frac{|V_{ij}^{true}||V_{kl}^{true}|}{|V_{ik}^{true}||V_{jl}^{true}|}. \tag{3.3.15}$$

Classically, this quantity has found little use in optical interferometry because changes in gains are often caused by the atmosphere, rather than something intrinsic to the instrument. Techniques that correct or rapidly follow the wavefront like adaptive optics, fast fringe tracking, or simple spatial filtering may make this quantity more useful in the future (Monnier 2007). Indeed, with fiber-based beam

combiners becoming more popular, small changes in flux injection into fibers could be compensated using closure amplitudes. To date, a specification for storing closure amplitudes in OIFITS data files has not been ratified.

3.3.5 Differential phase and differential visibility

Finally, the case where the interferometric data are spectrally dispersed, additional quantities called differential phase and differential visibility can be computed. As there is no ratified standard for reporting this data in OIFITS format, implementations differ, but most choose a spectral channel as the "standard" and then compute the difference in visibilities, $V_{\text{diff}} = V_{\text{ref}} - V_m$, and phase, $\phi_{\text{diff}} = \phi_{\text{ref}} - \phi_m$, potentially normalizing so the reference visibility or phase has unit magnitude. The reference spectral bin is often chosen to reside in the continuum. An inspection of the *differential visibility* can determine if the region contributing to V_m is of a different angular extent than the reference region. Changes in *differential phase*; however, represent either a shift in the photocenter of region ϕ_m with respect to the reference channel, or some wavelength-dependent asymmetry.

It is worth noting that much like differential phase, differential closure phase can also be measured; although it too has not been ratified for storage in the OIFITS format.

3.4 Bayesian analysis

It is common in optical interferometry to use traditional χ^2 methods (i.e. Frequentest statistics) to judge the validity of a model or an image given some data; however, a more powerful technique exists which I have extensively used in this work. Bayesian statistics provide a consistent approach to estimate a set of parameters, Ω, in a hypothesis (an image/model), H, given some observed data, D. Furthermore, it also provides an objective method by which the likelihood of two models can be compared. Bayes' theorem states that

$$P(\Theta|D,H) = \frac{P(D|\Theta,H)P(\Theta|H)}{P(D|H)}, \tag{3.4.1}$$

where $P(\Theta|D,H) \equiv P(\Theta)$ is the posterior probability distribution of the parameters, $P(D|\Theta,H) \equiv L(\Theta)$ is the likelihood, $P(\Theta|H) = \pi(\Theta)$ is the prior, and $P(D|H) \equiv Z$ is the Bayesian Evidence.

In parameter estimation problems, where the model remains the same, the normalization factor Z is often ignored as it is independent of the parameters Θ. When selecting between various models the evidence plays a central role through the Bayes Factor:

$$R = \frac{P(H_1|D)}{P(H_0|D)} = \frac{P(D|H_1)P(H_1)}{P(D|H_0)P(H_0)} = \frac{Z_1}{Z_0}\frac{P(H_1)}{P(H_2)}. \tag{3.4.2}$$

The difficulty in using Bayesian evidence stems from the requirement that a multidimensional integral,

$$P(D|H) \equiv Z = \int L(\Theta)\pi(\Theta)d^D\Theta, \tag{3.4.3}$$

must be evaluated. Although it may be possible to evaluate this function analytically, often one of several numerical integration techniques (like Markov Chain

Monte Carlo combined with thermodynamic integration) must be invoked. In this work we use the *MultiNest* (Feroz and Hobson 2008, Feroz et al. 2009) library to compute the Bayesian evidence and sample the probability space. *MultiNest* accomplishes this using Markov chain methods and a clever implementation of ellipsoidal bounding conditions to constrain the values of Ω sampled at any given point in the optimization process. Bounding using this technique creates an efficient method by which systems that contain multiple minima and/or large curving degeneracies can be explored.

3.4.1 Likelihood functions

To use *MultiNest* the programmer must specify a likelihood function, $L(\Theta)$. This function computes the probability of the given parameters, Θ, subject to a set of observed outcomes (i.e. data). The likelihood function employed depends on the problem being solved. In this work we have assumed that simple multivariate statistical methods are appropriate for our data. We will discuss the likelihood functions used later in this text.

3.4.2 Joint probability distribution

In addition to providing a framework to evaluate the validity of one or more models, Bayesian statistics also provide a method by which different, yet complementary information on a set of parameters may be obtained. Consider two sources of data, D_1 and D_2, which form the entire data set $D = D_1 \cup D_2$. These data are described by a single set parameters, Θ, by two independent hypotheses, H_1 and H_2. We wish to find *the* hypothesis, $H = H_1 \cup H_2$, that describes both data sets in a consistent fashion. In this case, the *joint probability* is formed by:

$$P(\Theta|D,H) = \frac{P(D_1|\Theta,H_1)}{P(D_1|H_1)}\frac{P(D_2|\Theta,H_2)}{P(D_2|H_2)}P(\Theta|H_1,H_2). \tag{3.4.4}$$

This method is more constraining than the individual probabilities $P(H_1|D_1)$ and $P(H_2|D_2)$. This is because the probability densities for each data set are different from one another, so the product, called the *joint probability*, is much more tightly bound than either component alone.

3.4.3 Choice of priors

One of the main advantages to Bayesian analysis is that it uses your prior knowledge along with the data, contrasted with traditional frequentist statistics which only use the data to infer knowledge. If the experimenter has no prior knowledge about the parameter being explored, they may choose a uniform or logarithmically-uniform (Jeffrey's) prior; however, if some external source provides significant constraints on a particular parameter one of several conjugate priors may be used. In this work we will summarize the priors used in each chapter.

3.5 Past interferometric observations of ϵ Aurigae

3.5.1 Speckle interferometry

Using the astrometric orbit from Strand (1959), ϵ Aurigae was identified as a potential candidate for speckle interferometry because of the predicted 30+ *mas* separation during nodal passage (McAlister 1976). Even though conditions seemed favorable, the vast difference in component fluxes prohibited several authors (McAlister 1978, Hartkopf and McAlister 1984, Isobe et al. 1990, Isobe 1991) from resolving the binary.

3.5.2 US Navy Optical Interferometer (NOI)

The Navy Optical Interferometer (formerly the Navy Prototype Optical Interferometer) obtained three scans of ϵ Aurigae, in 10 spectral channels spaced evenly in

wavenumber between 649 and 849 nm on the 38m baseline. From this, Nordgren et al. (2001) derived a uniform disk diameter (UDD) of 2.18 ± 0.05 *mas*. By assuming a spectral type, corresponding stellar model, and quadratic limb darkening coefficients from Claret et al. (1995), this UDD was converted to a limb darkened diameter (LDD) of 2.28 ± 0.09 *mas* with a limb darkening correction of 1.048. At the time, this compared favorably to the provisional Mark III LDD of 2.17 ± 0.03 *mas* with an LDC of 1.044 (see Nordgren et al. 2001).

3.5.3 Mark III

The Mark III interferometer (Shao et al. 1988) also observed ϵ Aurigae. At one point, it was claimed (Pan et al. 1994) that the companion was detected at a separation of 2 *mas* with a $\Delta m \approx 2.2$ mag. A few years later, the Mark III found an angular diameter of the F-star at about this value making the former claim unlikely. Indeed, visibility-only data acquired during six nights consisting of four scans on the 11.4m, two on the 15.2m, and nine on the 23.1m baselines were used to determine the F-star's UDD of 2.094 ± 0.042 *mas* at 451 nm, 1.946 ± 0.058 *mas* at 500 nm, and 2.006 ± 0.082 *mas* at 800 nm (Mozurkewich et al. 2003). Applying the same conversion technique as Nordgren et al. (2001), the UDD was converted into a LDD of 2.096 $\pm$ 0.086 *mas* for the F-star. It is important to note that with such short baselines, the data is most certainly high up on the first visibility lobe. Therefore the LDD is entirely dependent on the assumed stellar model and limb darkening law.

3.5.4 Modeling and other sources

In addition to direct interferometric observations, there was at least one theoretical prediction of the angular diameter of ϵ Aurigae. Using photometric model fitting, Blackwell and Shallis (1977) predicted angular diameters of 6.3 to 7.9 *mas* for ϵ Aurigae between $2 - 10\mu$m. Given that the spectral energy distribution (see Hoard

et al. 2010; 2012) of both the F-star and disk have nearly equal intensities at these wavelengths, it is unclear which of the two objects may have this angular diameter.

3.5.5 Unanswered questions

Even with the angular diameter seemingly determined, several key questions remained. As discussed in Chapter 2, the F-star exhibits an out-of-eclipse photometric variation with a $\Delta V = 0.1$ mag amplitude. Stencel (2007) speculated these variations could be caused by radial changes on the F-star (akin to Cepheid pulsation), a heated region on the disk rotating into view, or possibly something assoicated with mass transfer.

More fundamentally, even though the existence of the disk had been theorized and observational evidence appears to support this interpretation (see Chapter 1), the disk has never been directly observed. It is possible, although unlikely, that one of the alternative hypotheses discussed in Section 1.1.1 might indeed be correct.

Therefore in early 2005, Dr. Robert Stencel organized an international campaign to investigate the system. Upon the start of my graduate career at the University of Denver, in late 2007, I joined these efforts. Our objectives are to investigate the nature of the photometric variations, the physical properties of the F-star (diameter, limb darkening coefficient, oblateness), the presence and characteristics of the disk (diameter, height, scale height, opacity, ingress/egress profiles), and the orbital parameters of the system (position angle of the ascending node, Ω, total angular semi-major axis, $\alpha = \alpha_1 + \alpha_2$, and orbital inclination, i).

3.6 New data sources

To accomplish these objectives, new data were required. A series of observations at the Palomar Testbed Interferometer (PTI hereafter) and Georgia State University's Center for High Angular Resolution Astronomy interferometric array (CHARA

hereafter) were undertaken. Through these efforts and archival work, a total of 62 nights of data starting in October 1997 and ending November 2011 were obtained. Although stated without substantiation, these data may represent the largest quantity of optical interferometric data obtained on a single target to-date. When consecutive nights of data were available, the resulting OIFITS files were merged to increase UV coverage. Calibrator information can be found in Table 3.1. All 62 nights of data are summarized in Table 3.2. In Figure 3.6 we plot a typical eclipse light curve along with tick marks to indicate the CHARA observations. The next two sections discuss the data in detail, including the reduction methods employed.

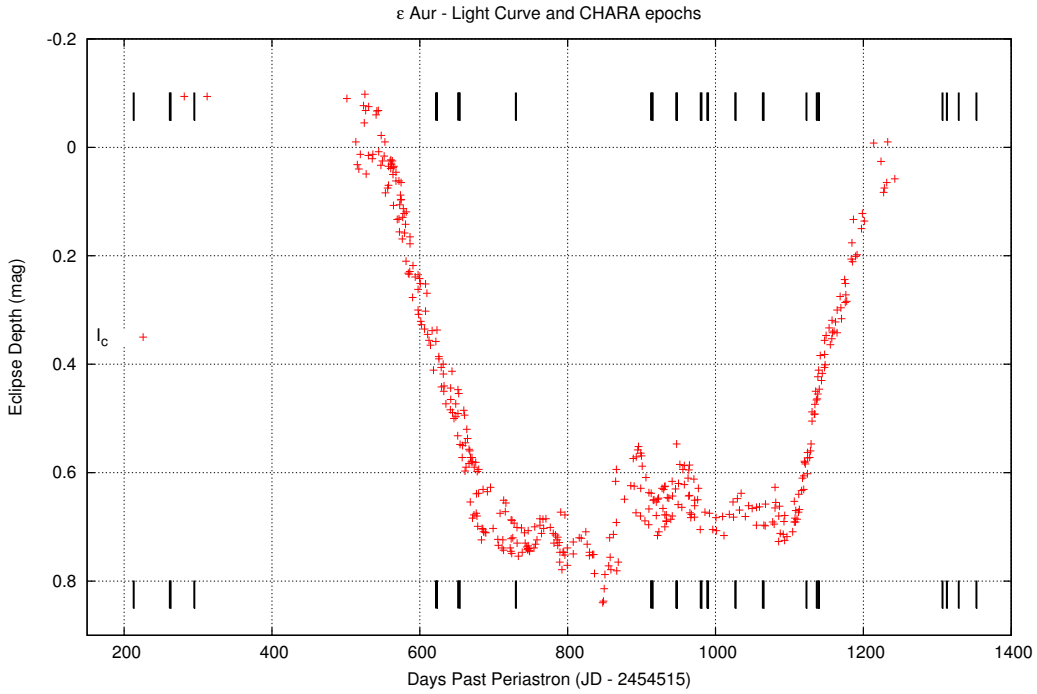

Figure 3.6: A representative eclipse depth plot from photometric I_c data (red points, from the AAVSO database) and nights of CHARA observations (black tick marks) as indicated in Table 3.2. Sequential nights of observations result in thicker tick marks. As can be seen there are three pre-eclipse, two ingress, seven totality, two egress, and four post-eclipse epochs. Of the totality epochs, one is pre-mid-eclipse, one is centered on mid-eclipse, and five are post-mid-eclipse.

Table 3.1: All calibrators and adopted parameters. UDD_x is the UDD in band x. Array: C = CHARA, P = PTI. References are 1 MIRC calibration database, 2 Lafrasse et al. (2010), 3 van Belle et al. (2008).

		Position (J2000)					Diameters [1]			Adopted			
HD	Name	RA	DEC	μ_α	μ_δ	π	UDD_H	UDD_K	σ_{UDD}	UDD	σ_{UDD}	Array	Ref.
		(H M S)	(D M S)	(mas/yr)	(mas/yr)	(mas)	(mas)	(mas)	(mas)	(mas)	(mas)		
3360	17 Cas	00 36 58.28	+53 53 48.88	18.76	-8.64	5.5	0.287	0.288	0.02	0.3	0.02	C	1
5448	37 And	00 56 45.21	+38 29 57.63	153.48	36.49	25.14	0.593	0.594	0.042	0.64	0.04	C	1
14055	Gam Tri	02 17 18.86	+33 50 49.89	44.64	-52.57	29.04	0.47	0.471	0.033	0.471	0.033	P	2
21770	36 Per	03 32 26.26	+46 03 24.69	-52.11	-75.26	27.53	...	...	...	0.55	0.03	C	1
24398	zet Per	03 54 07.92	+31 53 01.08	5.77	-9.92	4.34	...	...	...	0.645	0.026	C	1
24760	45 Per	03 57 51.23	+40 00 36.77	14.06	-23.78	5.11	...	...	...	0.41	0.02	C	1
27946	67 Tau (V*)	04 25 25.01	+22 11 59.98	111.97	-47.71	22.03	0.442	0.443	0.031	0.443	0.031	P	2
29645	HR 1489	04 41 50.25	+38 16 48.66	241.65	-97.15	31.38	0.521	0.522	0.037	0.522	0.037	P	2
30138	HR 1514	04 46 44.47	+40 18 45.32	9.07	-36.83	7.53	0.856	0.86	0.061	0.86	0.061	P	2
30823	HR 1550	04 52 47.75	+42 35 11.85	-10.63	0.46	7.2	0.317	0.317	0.022	0.317	0.022	P	2

continued on next page

		Position (J2000)					Diameters [1]			Adopted			
HD	Name	RA	DEC	μ_α	μ_δ	π	UDD_H	UDD_K	σ_{UDD}	UDD	σ_{UDD}	Array	Ref.
		(H M S)	(D M S)	(mas/yr)	(mas/yr)	(mas)	(mas)	(mas)	(mas)	(mas)	(mas)		
32630	10/eta Aur	05 06 30.89	+41 14 04.11	31.45	-67.87	13.4	...	...	...	0.419	0.063	C,P	1
37394	V538 Aur	05 41 20.33	+53 28 51.80	1.82	-523.99	81.45	0.64	0.643	0.046	0.65	0.02	C	3
41636	HR 2153	06 08 23.13	+41 03 20.61	1.36	-48.55	7.82	...	...	...	0.77	0.04	C	3
42807	HR 2208	06 13 12.50	+10 37 37.70	77.38	-298	55.71	0.473	0.475	0.034	0.475	0.034	P	2
50019	the Gem	06 52 47.33	+33 57 40.51	-1.66	-47.31	17.25	0.802	0.804	0.056	0.88	0.057	C	3
78715	79 CNC	09 10 20.85	+21 59 47.10	2.64	5.37	8.86	...	...	...	0.7	0.044	C	3
79452	HR 3664	09 15 14.24	+34 38 00.65	-158.2	47.73	7.69	0.79	0.794	0.056	0.794	0.056	P	2
73262	del Hya	08 37 39.36	+05 42 13.60	-70.19	-7.9	20.34	0.464	0.465	0.032	0.465	0.032	P	2

Table 3.2: Information on all avaliable interferometric epochs including the time of observations, array, combiner, spectral model, calibrators, observers and additional notes. Observer codes are summarized in Table 3.3.

JD	Date	Array	Combiner	Band	Calibrators (HD)	Observers	Notes
2450743	1997-10-22	PTI	...	K_7CH	32630		
2450761	1997-11-09	PTI	...	K_11CH	32630		
2451124	1998-11-07	PTI	...	K_5CH	32630		
2451142	1998-11-25	PTI	...	K_5CH	30823		
2451143	1998-11-26	PTI	...	K_5CH	42807		
2453715	2005-11-12	PTI	...	K_9CH	29645, 79452		Seemingly Bad Calibration
2453766	2006-01-31	PTI	...				No Calibrators
2454392	2007-10-19	PTI	...	K_5CH	29645	RS, MCE, AAH	

continued on next page

JD	Date	Array	Combiner	Band	Calibrators (HD)	Observers	Notes
2454393	2007-10-20	PTI	...	K_9CH	30138, 32630	RS, MCE, AAH	
2454394	2007-10-21	PTI	...	K_5CH	30138	RS, MCE, AAH	
2454431	2007-11-27	PTI	...	K_5CH	14055, 27946	DM	
2454457	2007-12-23	PTI	...	K_5CH	30138, 32630, 79452	DM	
2454458	2007-12-24	PTI	...	K_5CH	30138, 32630, 79452	DM	
2454512	2008-02-16	PTI	...	K_5CH	27397, 32630	DM	
2454513	2008-02-17	PTI	...	K_5CH	30138, 32630	DM	
2454514	2008-02-18	PTI	...	K_5CH	30138, 32630, 79452	DM	
2454728	2008-09-18	CHARA	MIRC	H Low	22928	GS, PJ	
2454756	2008-10-17	PTI	...	K_5CH	32630	MCE, DM	
2454765	2008-10-26	PTI	...	K_5CH	32630	DM	
2454777	2008-11-06	CHARA	MIRC	H Low	5448, 24398, 50019	MZ, XC, PJ	

continued on next page

JD	Date	Array	Combiner	Band	Calibrators (HD)	Observers	Notes
2454778	2008-11-07	CHARA	MIRC	H Low	5448, 24398, 50019	MZ, XC, PJ	
2454778	2008-11-08	PTI	...	K_5CH	32630	DM	
2454779	2008-11-09	PTI	...	K_5CH	32630, 30823	DM	
2454786	2008-11-16	PTI	...	K_5CH	42807, 73262	DM	
2454792	2008-11-22	PTI	...	K_5CH	30138, 32630	DM	
2454810	2008-12-09	CHARA	MIRC	H Low	24398	GS, MZ	
2454820	2008-12-20	PTI	...			DM	No Suitable Calibrators
2454821	2008-12-21	PTI	...			DM	Only one Spec Record
2455137	2009-11-01	CHARA	MIRC	H Low	5448, 24760, 32630	BK, CF, FB, GS, MZ, PJ, RS	
2455138	2009-11-02	CHARA	MIRC	H Low	24760, 32630	BK, CF, FB, GS, MZ, PJ, RS	

continued on next page

JD	Date	Array	Combiner	Band	Calibrators (HD)	Observers	Notes
2455138	2009-11-03	CHARA	MIRC	H Low	24760, 32630	BK, CF, FB, GS, MZ, PJ, RS	MIRC + PAVO
2455167	2009-12-01	CHARA	MIRC	H Low	24760, 32630, 78715	BK, CF, FB, GS	
2455168	2009-12-02	CHARA	MIRC	H Low	24760, 32630, 41636	BK, CF, FB, GS	
2455169	2009-12-03	CHARA	MIRC	H Low	24760, 32630, 41636	BK, CF, FB, GS	
2455245	2010-02-17	CHARA	MIRC	H Low	32630, 41636	GS, PJ, TB, NT, JDM*	
2455246	2010-02-18	CHARA	MIRC	H Low		GS, PJ, TB, NT, JDM*	See Text
2455428	2010-08-19	CHARA	MIRC	H Low	21770, 24760, 32630	BK, GS, RS, PJ, CF	
2455429	2010-08-20	CHARA	MIRC	H Low	21770, 24760, 32630	BK, GS, RS, PJ, CF	

continued on next page

JD	Date	Array	Combiner	Band	Calibrators (HD)	Observers	Notes
2455430	2010-08-21	CHARA	MIRC	H Low	21770, 32630	BK, GS, RS, PJ, CF	
2455431	2010-08-22	CHARA	MIRC	H Low	21770, 24760, 32630	BK, GS, RS, PJ, CF	
2455462	2010-09-22	CHARA	MIRC	H Low	24760, 32630	BK, GS, PJ, XC	
2455463	2010-09-23	CHARA	MIRC	H Low	21770, 24760, 32630	BK, GS, PJ, XC	
2455465	2010-09-25	CHARA	MIRC	H Low	32630	XC, PJ, CF	MIRC + PAVO
2455466	2010-09-26	CHARA	MIRC	H Low	32630	XC, PJ, CF	MIRC + PAVO
2455467	2010-09-27	CHARA	MIRC	H Low	32630	XC, PJ, CF	MIRC + PAVO
2455495	2010-10-25	CHARA	MIRC	H Low	24760, 32630	BK, GS, PJ	
2455496	2010-10-26	CHARA	MIRC	H Low	32630	BK, GS, PJ	
2455504	2010-11-03	CHARA	MIRC	H Low	21770, 24760, 32630	GS, PJ	

continued on next page

JD	Date	Array	Combiner	Band	Calibrators (HD)	Observers	Notes
2455505	2010-11-04	CHARA	MIRC	H Low	21770, 24760, 32630	GS, PJ	
2455542	2010-12-11	CHARA	MIRC	H Low	32630	BK, CF, XC, RJ	
2455542	2010-12-12	CHARA	MIRC	H Low	24760, 32630	BK, CF, XC, RJ	MIRC + PAVO
2455543	2010-12-13	CHARA	MIRC	H Low	32630	XC, CF, BK, RJ	MIRC + PAVO
2455544	2010-12-14	CHARA	MIRC	H Low	32630	XC, CF, BK, RJ	MIRC + PAVO
2455579	2011-01-17	CHARA	MIRC	H Low	32630, 41636	GS, PJ	
2455580	2011-01-18	CHARA	MIRC	H Low	32630, 41636	GS, PJ	
2455638	2011-03-18	CHARA	CLIMB	K	32630	GS, PJ, BK*	
2455652	2011-04-01	CHARA	CLIMB	K	32630	CF, BK*	
2455654	2011-04-03	CHARA	CLIMB	K	32630	CF, BK*	
2455655	2011-04-05	CHARA	CLIMB	K	32630	CF, BK*	
2455822	2011-09-17	CHARA	MIRC	H Low	32630	XC, RP, PJ	

continued on next page

JD	Date	Array	Combiner	Band	Calibrators (HD)	Observers	Notes
2455828	2011-09-23	CHARA	MIRC	H Low	27396	RP, PJ	See Text
2455844	2011-10-09	CHARA	MIRC	H Low	21770, 32630	BK, CF, XC*	
2455868	2011-11-02	CHARA	MIRC	H Low	24760, 32630	XC, PJ, BK*	

Table 3.3: Observer codes for Table 3.2.

Code	Name	Code	Name
AAH	Alexa Hart	NT	Nils Turner
BK	Brian Kloppenborg	PAVO	U. Sydney Observers
CF	Chris Farrington	PJ	PJ Goldfinger
DM	Dale Mais	RJ	Randall Wall
FB	Fabien Baron	RP	Robert Parks
GS	Gail Schaefer	RS	Robert Stencel
JDM	John D. Monnier	TB	Theo ten Brummelar
MCE	Michelle Creech-Eakman	XC	Xiao Che
MZ	Ming Zhao		

3.6.1 Palomar Testbed Interferometer (PTI)

PTI (Colavita et al. 1999) was a long baseline interferometer located at the Palomar Observatory in California. It was built to test interferometric techniques for the Keck Interferometer. The instrument operated between 1995 July and 2008 December. The array consisted of three 40cm siderostats, each located at the termination of one of the interferometer's arms. Pairwise combination provided baselines between 85 and 110m. The beam combiner at PTI operated in several low resolution spectral modes (with up to 11 spectral channels) across the K-band (2.2μm). A unique feature of the array is that it had a pair of long delay lines, one short delay line, and a second beam combiner. Using all of this equipment, fringes from two stars within the same field of view could be tracked simultaneously for precise astrometric measurements.

Data and reduction

Data from PTI consisted of several levels. Level 0 data files are raw output from the interferometer. At the end of the observing night, the array operator ran a program

called *vis* (see Colavita et al. 1999) which processes the Level 0 data files and creates Level 1 files. These files are provided to the end user as a series of ASCII or FITS files for later processing.

Level 1 data files contain spectrally dispersed V^2, wide band (that is, spectrally averaged) V^2, an observer log, a nightly report, the catalog (observing schedule) file, postscript plots of the raw V^2 measurements, and additional metadata. This information, along with a baseline model (a *.baseline* file) are passed to the narrow- and wide-band calibration routines *nbCalib* and *wbCalib*, respectively, from the *V2calib* software package. These two programs automate a majority of the data reduction process by computing calibrated V^2 and the UV coordinates at the time of observation. For the reductions herein, I have used the web-based version of these calibration tools, *webCalib*, from the Michelson Science Center to produce the calibrated data products. When using *webCalib* we selected the PTI defaults with the following exceptions: (1) the calibration window was extended to four hours; (2) no ratio correction was applied, and (3) no minimum uncertainty was enforced.

Much of the wide-band visibility data has been discussed previously in Stencel et al. (2008), therefore we will not consider it further. Instead, we have re-reduced and re-calibrated the narrow-band data using updated angular diameter estimates for the calibrators from van Belle et al. (2008), Lafrasse et al. (2010) and Kloppenborg et al. (2010) while significantly improving upon the model fitting methods employed.

3.6.2 Center for High Angular Resolution Astronomy (CHARA)

Georgia State University's Center for High Angular Resolution Astronomy (CHARA ten Brummelaar et al. 2005) is an interferometric array located on Mount Wilson, CA. The array consists of six 1-m telescopes capable of 15 baselines ranging in length from 34 to 331 meters. Using the longest baselines, a resolution of down to 0.5 mas

in the H-band can be realized.

Initial calibration observations of ϵ Aurigae were taken far in advance of the eclipse, in 2008-09/11/12. Semi-regular observing commenced in 2009 November and ended in 2011 Nov. In total, ϵ Aurigae was observed on 38 nights, yielding 19 individual epochs after consecutive nights were merged. Details of the individual observations are summarized in Table 3.2. The UV coverage, visibilities, and closure phase plots for each epoch are plotted in Figures 3.18 - 3.33. Images of the ingress phase and preliminary fits were reported in Kloppenborg et al. (2010) with an update in Kloppenborg et al. (2011).

Michigan InfraRed Combiner (MIRC)

At CHARA we used the Michigan InfraRed Combiner (MIRC; described in Monnier 2006, Monnier et al. 2004). Over the years, the instrument went through several reincarnations. As it was first used, the combiner was configured for four telescope beam combination using a camera sensitive in the H- and K-bands. Three different spectral configurations with $R \sim 44$, 150, or 400 were available using a grisim or prisim. Photometric calibration of the individual beams was achieved using choppers that would periodically interrupt the beam during data acquisition. In August 2009, the choppers were replaced by dedicated photometric channels (Che et al. 2010) that utilize a fraction light from each science beam for calibrated, spectrally dispersed photometry. This led to a dramatic improvement in visibility and closure phase uncertainties. In the spring of 2011, MIRC was upgraded again to combine light from all six of CHARA's telescopes (see initial report in Monnier et al. 2010), permitting measurement of 15 non-redundant visibilities and all 20 independent closure phases available at CHARA.

All MIRC data were reduced using the standard reduction pipeline described in Monnier et al. (2007) with respect to the calibrators listed in Table 3.1. The reduction method consists of six major steps:

1. Pixels belonging to the unused quadrants of the detector are removed. The remaining subarray frames are then coadded, and filtered for data dropouts. Metadata files (logging and detector configuration) are written to disk.

2. The metadata files are parsed and the time of observation and instantaneous UV coordinates are calculated.

3. Establish the wavelength scale from fringe fitting by applying either a linear or quadradic model to the spectrometer channels. This step also applies backgrounds and shutter sequences.

4. Perform fringe analysis including the detection and extraction of interferometric data, creation of powerspectra, triple amplitudes and closure phases for the spectrally dispersed data.

5. The data are calibrated by using stars of known diameters. The data are split into chunks and averaged. The user is presented with the averaged data and is permitted to inspect the data in detail, removing any data where fringes are lost.

6. Lastly both calibrated and uncalibrated data are written out in the OIFITS data format and summary plots of the data are generated for each object.

In most cases the data reduction proceeded as described above, but in a few cases technical issues created extenuating circumstances that are be discussed in greater detail below:

2009-12-02/03 The OPLE computer at CHARA was upgraded to a 64-bit OS, but a 64-bit patch to MIRC control software had not been applied. This difference caused errors within the FITS headers, therefore we disabled any header information relating to the object being observed. Using our logs, we later restored the FITS headers and processed the data using the regular reduction pipeline.

2010-02-19 Observing conditions this night were very poor. Fringes were found for ϵ Aurigae on three of four baselines, but fringes could not be found on any calibrators. It is possible to exploit the stability of MIRC's closure phases and recover the closure phases from these data. When this night is included with the 2010 Feb. data the images reconstructed and models recovered have no substantial differences, save a much lower likelihood. Therefore we did not include data from this night in our analysis.

2010-12-14 During the reduction process we noticed some negative V^2 and uncharacteristically large uncertainties (i.e. 60 degree errors in closure phase) for the longest baselines. Because of these factors we have excluded this night from our merged data set.

2011-01-19 Telescope E2 malfunctioned near the end of the observing night and was stowed. Because the MIRC pipeline expects light on all beams (regardless of whether or not fringes are present), we inserted an E2 shutter sequences from the night prior. The resulting OIFITS data therefore contained baselines and triplets involving E2 which we have removed before conducting our work.

2011-09-17 The shutter sequence on HD 32630 (calibrator) was interrupted and was not repeated. This prohibits the entire calibrator data block from being used. We have used HD 27396 as a sole calibrator on this night.

2011 6T Data We have noticed adjacent spectral channels on S1E2 and S2E2 disagree at a 3σ or greater level. The channels most affected are at $(\lambda, \Delta\lambda)$ $(1.5602, 3.69E-2)$, $(1.5967, 3.61E-02)$, and $(1.6324, 3.53E-02)$ where all measurements are in μm. From our infrared spectroscopy (Stencel et al. 2011) we know this region is occupied by the Hydrogen Brackett band head at 1.46 μm. By comparing line depths at this time with a pre-eclipse spectrum, the 2011 lines appear less deep by $\sim 7 \times 10^{-4}$ (W/m^2). This is far beyond the uncertainties in our spectra, so this change is likely real. Given the S1E2 and S2E2 baselines have the highest angular resolution, it is possible that MIRC may have detected changes in the absorbing region.

CLassic Interferometry with Multiple Baselines (CLIMB)

The CLassic Interferometry with Multiple Baselines (CLIMB; Sturmann et al. 2010) combiner the in-house CHARA beam combiner. CLIMB uses three telescopes and can operate in one of five broadband spectral modes. Recent upgrades permit two, potentially independent, three-telescope CLIMB sessions to run in parallel, thereby utilizing all six of CHARA's telescopes (but providing only three V^2 and one T3). For our observations we have used CLIMB 1 (beams 1-3) during the egress phase in spring 2011 with the K-continuum ($\bar{\lambda} = 2089.4$ nm, FWHM 23.5 nm) filter installed and destructive readout mode.

The data reduction pipeline and method for fringe extraction for CLIMB is discussed in detail by Brummelaar (2012), therefore we only comment on the major reduction steps:

1. The background and amount of light in each beam is calculated from the shutter sequence. The background is subtracted from the data and the transfer functions are calculated.

2. The mean powerspectra for each beam and each fringe scan is computed. Using this information, the predicted noise power spectrum is calculated and subtracted from the fringe power spectrum.

3. Using the fringe power spectra, the frequencies which contain fringe information are computed.

4. The user is prompted to remove regions of the baseline fringe signal that contains noise and/or no data.

5. Visibilities are estimated on each baseline

6. The closure phase signal is estimated by computing the phase of each baseline independently, then the triple product is formed by Equation 3.3.12 from which the closure phase is calculated after weighting by the fringe amplitude.

For the ϵ Aurigae, we used the 2012-02-29 version of the CLIMB reduction software. The CLIMB data have been reduced, but an outstanding calibration issue with closure phases prohibits us from conducting a full analysis on these data. We will include them in a future publication.

3.7 Image reconstruction

The fundamental problem being solved by optical interferometric image reconstruction software is one of inversion: given sparse sampling in the complex plane and the associated interferometric data (and noise), what is the most probable image that corresponds to these data? Recently there several reviews on image reconstruction and the difficulties it encounters have been published. It is suggested that the reader review Berger et al. (2012) and references therein for an appreciation of this topic.

Inverting optical interferometric data to an image is difficult and there are many approaches to solving this problem. The Optical Interferometric Beauty Contests

(Lawson et al. 2004b;a, Lawson 2006, Cotton et al. 2008) were designed to facilitate the comparison between different algorithmic approaches. The Bispectrum Maximum Entropy Method (BSMEM, Buscher 1994) and Markov Chain Imager (MACIM, Ireland 2006) have consistently performed well in these competitions, so we have used them in this work.

To invert the data, these two programs employ fundamentally different approaches. MACIM uses global stochastic minimization by simulated annealing and Bayesian *a posteriori* methods, whereas BSMEM uses local gradient-based approaches combined with entropic principles. In collaboration with Fabien Baron at the University of Michigan, I have also worked on new image reconstruction techniques (SQUEEZE and GPAIR; Baron et al. 2010, Baron and Kloppenborg 2010). Due to the experimental nature of these methods, resulting images will not be discussed here.

3.8 Modeling

At the beginning of the 2009-2011 eclipse, ϵ Aurigae presented a significant challenge to existing interferometric modeling software because *none* were designed to model eclipses by an opaque object. Traditional modeling software uses analytic models of simple, light-emitting, geometric primitives whose FTs are known. For instance, *LITpro* (Tallon-Bosc et al. 2008) developed by the Jean-Marie Mariotti Center (JMMC) implements point sources, uniform and limb-darkened disks, ellipses, Gaussians, and rings with finite width.

In order to model a more complicated object, one is required to construct it from these primitives. Using such simple objects comes with one clear benefit: speed. Analytic FTs may be computed on paper and directly implemented in software. This benefit is also a detriment. For very complex geometries like Roche Lobes, stars with spots, objects undergoing non-radial pulsation, or eclipsing systems, the

FTs is dependent on underlying system parameters that may not be known *a priori*. In the case of ϵ Aurigae is it possible to write down the analytic FT for an eclipse caused by a simple object (i.e. a rectangle or ellipsoid), but it becomes quickly prohibitive to manually derive the FT for more complicated geometries.

Although existing software was adequate for many interferometric science objectives, it did not meet the criterion for modeling ϵ Aurigae. Not only was the eclipsing object dark, but the positions of the system's components were time-dependent. Existing modeling software would require each epoch be modeled individually, rather than fitting all epochs simultaneously. For example, the current approach to modeling a Cepheid would be to determine the star's diameter and limb darkening coefficient at each epoch and then fit the resulting values to determine the period and amplitude. If the period were known *a priori*, say from photometry, this information should be incorporated into the interferometric model fitting process. Similarly, at present the orbit of a binary is found by finding the positions of the components at each epoch and the resulting (r, θ) value are fit to an orbital solution. Clearly, the interferometric data should be fit *directly* to an orbit and stellar model to enforce cross-epoch consistency and any time-dependent effects.

I address the aforementioned issues by creating two software products. The first is the *OpenCL Interferometry Library*, *LIBOI*, which provides a framework for common interferometric tasks on a parallel computing platform. The second program is the *SImultation and Modeling Tool for Optical Interferometry*, *SIMTOI*, that performs model fitting of complex, time-dependent, geometries. It is my intention to make both of these software products open source projects after publication of the papers assoicated with this dissertation.

3.8.1 OpenCL Interferometry Library (*LIBOI*)

The OpenCL Interferometry Library (*LIBOI*) is a C / C++ library that aims to provide software developers with access to routines that are commonly used in interferometry. *LIBOI* heavily relies on the heterogeneous computing environment targeted by the Open Compute Language (OpenCL). OpenCL permits one set of code to target a wide range of compute platforms including traditional and multi-core CPUs, servers, hand-held/embedded devices, specialized hardware, and Graphical Processing Units (GPUs). GPUs are a particularly interesting platform because their massively parallel nature permits one compute task to be split among 10's to 1,000's of processors connected to high latency, but high throughput memory bus.

At present *LIBOI* implements image normalization, discrete Fourier transforms (FT), FT to V^2, FT to bispectra, χ^2 and $\log Z$ (log of Bayesian evidence) functions all using GPU acceleration through OpenCL. Many of the routines are based upon those found in the GPu Accelerated Image Reconstruction (GPAIR) program (Baron and Kloppenborg 2010) which experienced GPU to CPU speed up factors up to 280x.

3.8.2 SImulation and Modeling Tool for Optical Interferometry (*SIMTOI*)

The SImulation and Modeling Tool for Optical Interferometry (*SIMTOI*) is a C++ / C / Fortran program for fitting time-dependent 3D models to large interferometric data sets. Instead of using analytic models, *SIMTOI* uses the Open Graphics Library (OpenGL) to tessellate the "surfaces" of the astronomical objects being modeled. The objects then are rotated, translated and rendered to a multisample buffer to alleviate pixel aliasing issues (see Fig 3.7(a) vs. 3.7(b)) that might skew the interferometric data.

To compute the interferometric observables, *SIMTOI* uses *LIBOI*, thereby leveraging the power of GPU computing. Because the images are rendered *on the GPU*, the data are readily available for *LIBOI*. This avoids a $\mathcal{O}(n)$ copy operation, thereby implicitly increasing the potential throughput of the library.

SIMTOI is written with astronomical conventions and portability in mind. All images are rendered with North up and East to the left and angles specified in the traditional astronomical sense. The code is designed to run on multiple platforms because the underlying libraries (OpenCL, OpenGL, and QT) are cross-platform comparable and the build environment, CMake, is available on Windows, Mac OS and Linux.

The 3D environment of *SIMTOI* has its viewport along the $+\hat{z}$ direction and uses orthographic projection (i.e. perspective effects disabled) with no lighting calculations. This ensures objects are not distorted and their flux is accurately portrayed. Object positions may be specified in the (x, y) plane, or in 3D using (x, y, z), or a a Keplerian elliptical orbit. Models consisting of simple geometrical objects like spheres, cylinders and three types of disks (discussed in detail below) are already implemented. Roche Lobes, oblate/rapid rotators, and planar flux distributions are planned. Viewing angle effects, like limb darkening and approximate integrated opacity, are implemented using the OpenGL shading language extension. All of the position, model, and shader parameters may be explicitly specified by the user or found via. minimization.

To find minima, users can select from two different minimization engines. The first is *Levmar* (Lourakis 2005) which is an implementation of the Levenberg-Marqardt optimization algorithm. The algorithm behaves like a steepest decent method if the current solution is far from the global minimum. When the current solution is close to a minimum, the code behaves like a Gauss-Newton method. The second engine is *MultiNest* (Feroz et al. 2009). This is a Bayesian inference tool

that calculates the evidence and explores the parameter space specified by the user. This library is capable of efficiently sampling parameter spaces that have multiple posterior modes and/or pronounced curving in moderately high dimensions. This minimizer reports the Bayesian evidence and posterior probability distributions so not only can a solution be objectively compared against other solutions, but the values of the derived parameters and their uncertainties can be directly inspected and plotted.

A few final features of *SIMTOI* which I wish to illustrate are the ability to animate models in real time, export simulated photometry to a text file, and export model images to FITS files for later use.

Render region limits

When a model area is created in *SIMTOI*, the user specifies the window width in pixels, w, and scale in mas/pixel, s. The image width is bounded to $64 < w < 8192$ by a developer choice at the lower limit and the maximum allowable image size on modern GPUs. Because of this, if a model is to be rendered without error, it must fully reside within the following bounds: $(-\frac{ws}{2} < x < \frac{ws}{2}, -\frac{ws}{2} < y < \frac{ws}{2}, -100 < z < 100)$ in units of mas. If the user wishes, the z limits may be expanded in a configuration file. If a surface of an object goes beyond these bounds, it may not be completely rendered.

Geometrical stellar models

A sample of the stars modeled by SIMTOI is shown in Figure 3.7. All stars are modeled using a single uniformly colored sphere of diameter d. The sphere is rendered in spherical polar coordinates (r, θ, ϕ). The surface is tessellated into 50 slices in ϕ and 50 stacks in θ resulting in 2,500 vertices. Limb darkening is implemented using the Hestroffer (1997) model:

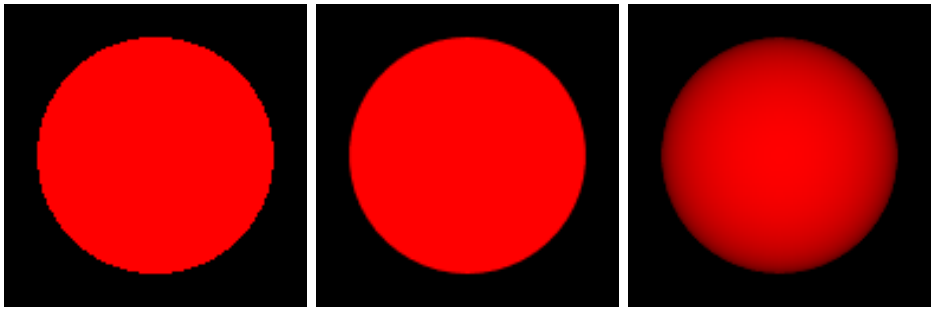

(a) Aliased (b) Anti-aliased (c) Limb Darkened

Figure 3.7: Sample of stars rendered by *SIMTOI*.

$$I_\lambda(\mu) = \mu^\alpha \tag{3.8.1}$$

in which α is the limb darkening coefficient (called LDD_α hereafter) and $\mu = \hat{z} \cdot \hat{n}$ where $\hat{z}$ is the viewing direction (i.e. towards the positive z direction), and $\hat{n}$ is the surface normal vector.

Disk models

The four disk models presently implemented in *SIMTOI* are drawn in Figure 3.8. All of the disk models inherit from a simple cylinder, but modify the vertex drawing routine for the cylinder rim. Like all other OpenGL primitives, cylinders are drawn in Cartesian coordinates, but for simplicity we list parameters in cylindrical polar (r, θ, ϕ) instead.

Cylinder The base-class cylinder object has total height h and diameter d. It is drawn about the origin. Additional cylinder functions use the intrinsic height $h_0 = \frac{h}{2}$ and radius $r_0 = \frac{d}{2}$ in their calculations. The top and bottom of the cylinder are drawn as solid surfaces at $z = \pm h_0$ with a radius of r_0. The side is drawn as a verticle wall from $-h_0 < z < h_0$ at $r = r_0$. By default, a cylinder is tesselated into 500 slices between $0 < \theta < 2\pi$ and 100 stacks between $-h_0 < z < h_0$ resulting in a model consisting of 5000 verticies.

Astrophysical disks The disk models modify the wall/rim of the cylinder by swapping a vertical wall with a monotonically decreasing function. This results in a disk that bulges radially outward as $z \to 0$. Internally the functions are implemented as $f(z)$, but below we write the functions as $f(r)$. In all cases, the surface of the cylinder or disk must be continuous and differentiable, so the normal vectors may be calculated.

Disk A uses an exponential decay defined by h_r

$$z(r, h_r) = \pm h_0 e^{-|r-r_0|/h_r} \tag{3.8.2}$$

Disk B attempts to implement a real astrophysical disk (i.e. one from Armitage 2010). The outer-edge of the disk follows a Gaussian defined by scale height, h_r:

$$z(r, h_r) = \pm h_0 e^{-\frac{(r-r_0)^2}{2h_r^2}} \tag{3.8.3}$$

Disk C is a power-law decay defined by β:

$$z(r, \beta) = h_0 \left(\pm \frac{r_0}{r}\right)^{\beta} \tag{3.8.4}$$

Figure 3.8: Sample of simple disk models rendered by *SIMTOI*. Images (b), (d), (f), (g), and (h) show the disk models edge on (i.e. $i = 90$). Images (a), (c), and (e) have $i = 45$ and were shaded for visualization of 3D geometry. Image (g) shows the "Disk B" model with height-dependent transparency. The darker ring in (e) shows where the Gaussian decay wall stops and the solid cap begins.

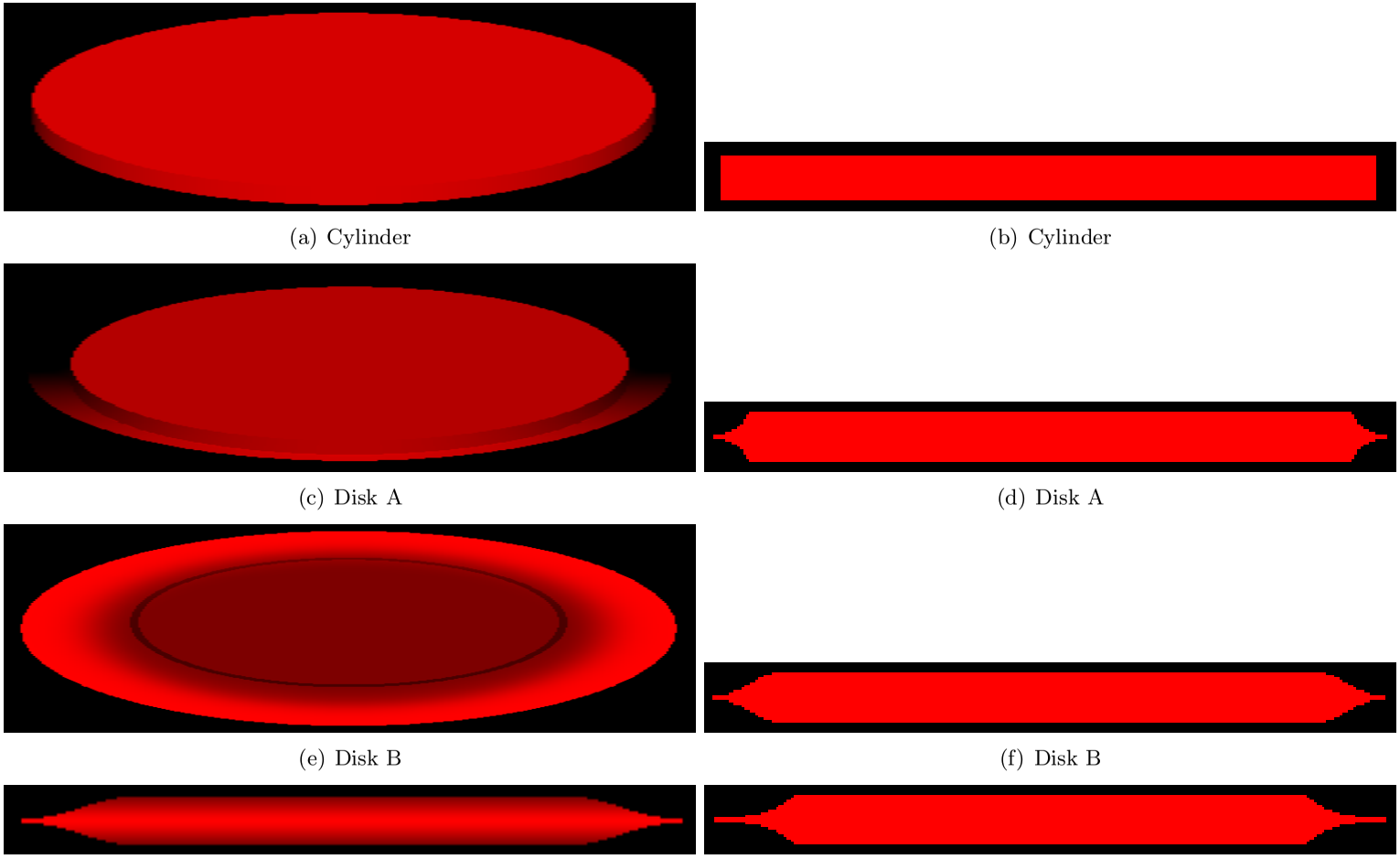

(a) Cylinder

(b) Cylinder

(c) Disk A

(d) Disk A

(e) Disk B

(f) Disk B

(g) Disk B

(h) Disk C

3.9 Results

Model fitting and image reconstruction on the available interferometric data has been conducted. As stated in the data analysis section, any interferometric observations that occurred over consecutive nights at a single facility using the same combiner have been merged to increase UV coverage. Even after being merged, the PTI data reside high-up on the first visibility lobe, therefore they do not provide sufficient information for image reconstruction. The CHARA data, however, often have one or more four-telescope observations from which images were generated. In the next several pages I provide a qualitative discussion of the images and quantitative descriptions from model fitting.

3.9.1 Images and qualitative discussion

BSMEM and MACIM were used to reconstruct both model independent and prior-informed images for most of the CHARA epochs. Initial images were reconstructed using the full field of view of CHARA, ~ 60 *mas*; however, no sources were detected at these large distances. Instead, we have reconstructed images using either 128x128 or 200x200 pixel images with a scale of 0.025 *mas*/pixel (corresponding to a field of view of $3.2 - 5.0$ *mas*). For the model-independent BSMEM images, an uninformative Gaussian prior with a characteristic spread of 1.4 *mas* was used. With MACIM we used 128x128 images with 0.025 *mas*/pixel pixellation and otherwise default parameters.

The results of these efforts are shown in Figures 3.9 - 3.13. The images are grouped into columns by observational epoch, and row by reconstruction/modeling method. When available, the BSMEM and MACIM model-independent images are in the top two rows, whereas the bottom row is always the best-fit model from *SIMTOI*. χ^2 for the resulting images can be found in Table 3.4. We postpone our discussion of the models until the next section. All images are drawn in the

traditional astronomical sense, namely North up, East to the left. On each page of these images,the 0.5 *mas* H-band resolution limit of CHARA is inscribed in the first image in the bottom row.

In the next few paragraphs we provide a qualitative discussion of the main features in the images. We reserve our discussion of image artifacts until later in this document. It is important to note that although some optical interferometric image reconstruction software do provide uncertainty maps, they are not widely used. A principle issue is that the uncertainties are frequently derived using a Markov chain process which results in a correlation between uncertainties and flux density. Therefore, we cannot provide a robust discussion of the photometric variations, or calibrated photometry from the images.

2008-09, 2008-11, 2008-12 The limited UV coverage for most of the 2008 data did not permit images to be reconstructed without the use of an informative prior. The 2008-11 data are the exception to this statement. In Figure 3.9 we see the BSMEM image (we were unable to create a MACIM image for this data set) that shows an approximately round object with three bright spots on the right edge. Because the spectral energy distribution (Hoard et al. 2010) predicts the F-star will be the brighter component at these wavelenghts, we interpret this to be the F-star. It appears to be nearly 2 *mas* in diameter with a slight elongation at a position angle of $\sim$ 120 degrees. The quantity of data is not very high, so we suspect any photometric variation is an artifact of the reconstruction process.

2009-11 Shortly after the photometric eclipse began, the 2009-09 data were acquired. In this image, we see a single, nearly circular object that is noticeably darker in the South-East quadrant. Knowing that the F-star is eclipsed we confirm our assumptions in the previous paragraph. The darkening in the South-East quadrant is interpreted to be due to the eclipsing object. Hereafter we shall refer to

the hemisphere of the star that is unobstructed as the "Northern hemisphere" and the obscured hemisphere as the "Southern hemisphere." A fraction of the F-star remains unobstructed in the South and South-West.

2009-12 This image closely resembles that of 2009 Nov, except the obscuration in the southern hemisphere has grown to the North-West. It appears as if there is additional obstruction immediately above the disk on the Eastern most edge.

2010-02 This image is composed of comparatively sparse UV coverage from 2010-02-17 for reasons discussed in Section 3.6.2. The limited quantity of data results in fairly poor model-independent images. Both BSMEM and MACIM imply that the entire southern hemisphere was obscured at this epoch. The best-fit model; however, implied that that a small fraction of the southern hemisphere may remain; however the thickness is likely too far below the resolution limit of CHARA to be detected.

2010-08 This epoch is placed 16 days after the nominal mid-eclipse date (2010-08-04). Here the northern hemisphere remains obscured and some flux in the South-West has reappeared. There is **no indication** of a central brightening or clearing associated with the center of the disk.

2010-09, 2010-10, 2010-11, 2010-12, 2011-01 These images are remarkably consistent. In all cases, the northern hemisphere remains unobstructed, as does streak of flux in the South (although it may be difficult to see in the printed figures). The UV coverages of these data are exceptional. The images imply the presence of photometric variations in the northern hemisphere and, perhaps, changes to the over-all shape of the F-star. We discuss the potential for artifacts in the 2010-10 data set below.

2011-09-17, 2011-09-23 After the eclipse ended, the science objective was post-eclipse calibration and study of the photometric variations. The 2011-09-17 epoch was the first MIRC six-telescope observation of ϵ Aurigae. The data represent a single six-telescope observation; however, the UV coverage is equivalent to at least three four-telescope observations. The 2011-09-23 epoch is again a single six-telescope observation. In both cases the reconstructed images imply the F-star is not entirely round. Small non-zero closure phases on these data may imply the presence of surface flux variations. The bright spot in the center of the 2011-09-17 image is likely due to a calibration issue on the longest baselines.

2011-10 This is the first multi-bracket six-telescope data set on ϵ Aurigae. It is qualitatively similar to the 2011-09 epochs.

2011-11 This single night of data is the largest six-telescope data set obtained on ϵ Aurigae to date. The image appears significantly more round than all prior observations, most likely due to the increased UV coverage. Again the bright spot in the center of the image is likely due to a calibration issue.

Figure 3.9: Pre-Eclipse observations of ϵ Aurigae. The BSMEM and MACIM rows are model-independent images as described in the text. The Model row is the best-fit result from *SIMTOI*. All images are rendered with North up, East to the left. The 0.5 *mas* H-band resolution of CHARA is indicated by the white circle in the upper left of the first model image. χ^2 for the resulting images can be found in Table 3.4

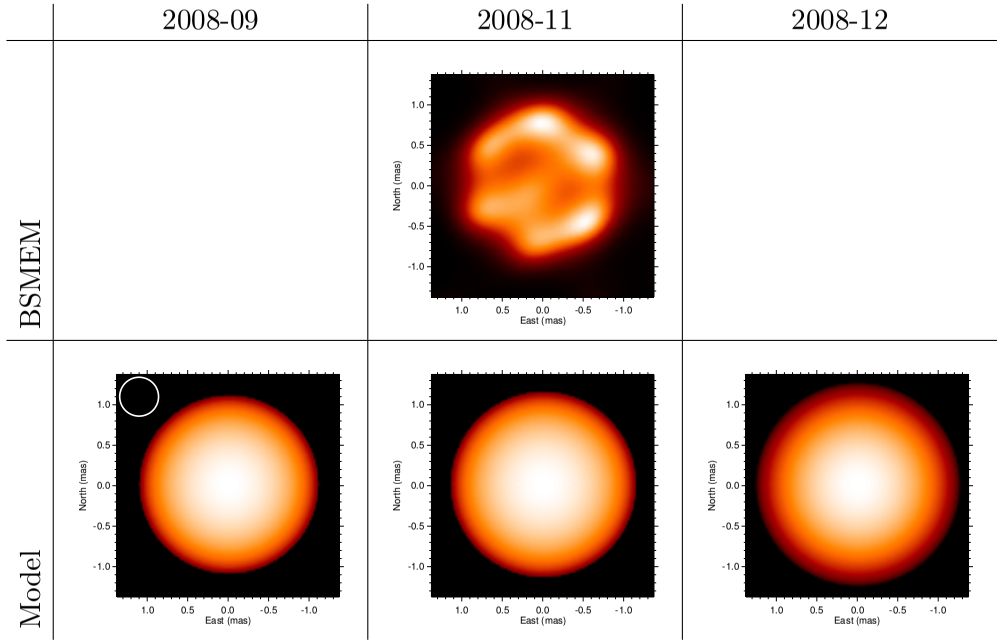

Figure 3.10: Ingress and totality images. See description in Figure 3.9 and in the text.

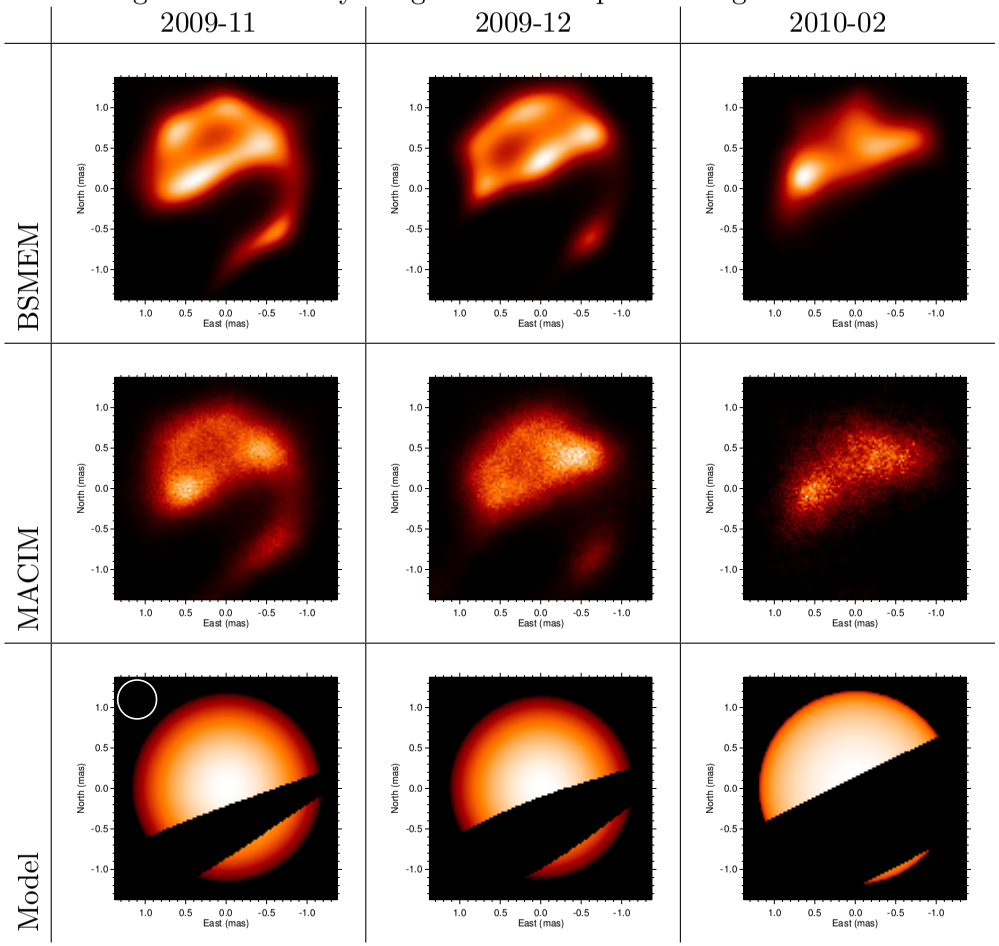

Figure 3.11: Mid eclipse and totality images. See description in Figure 3.9 and in the text.

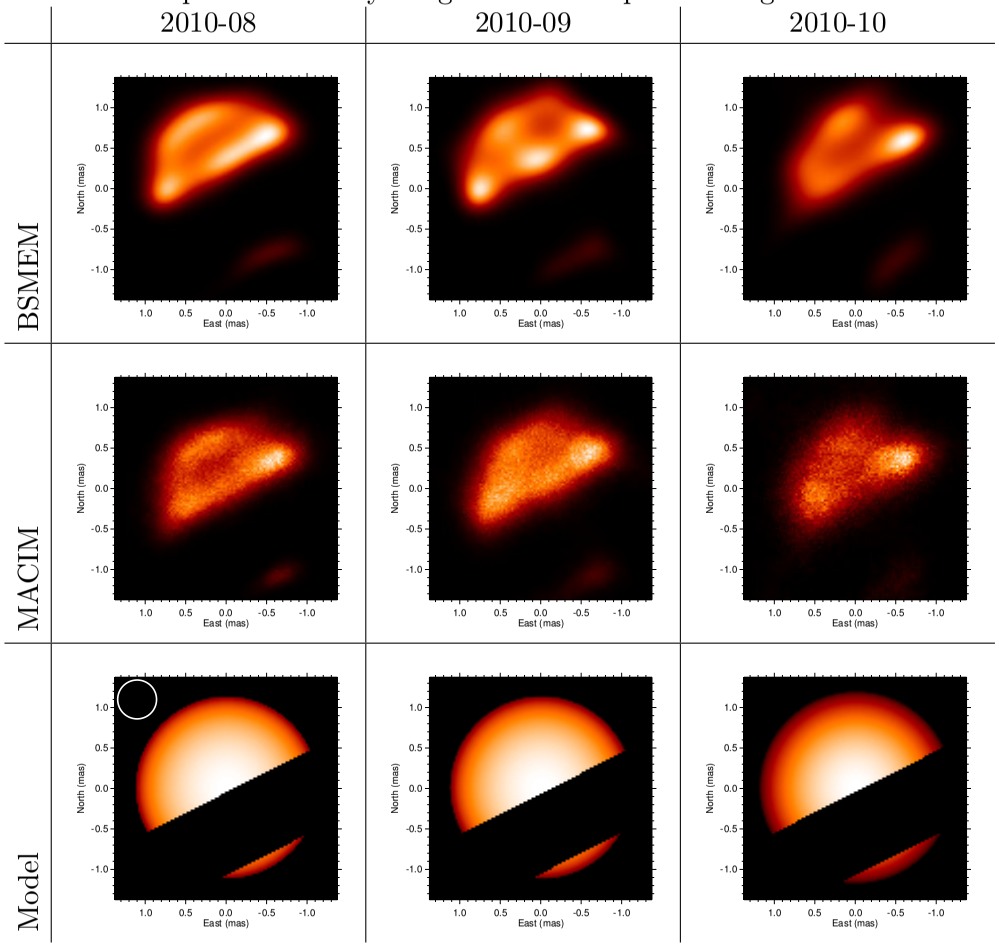

Figure 3.12: Post-mid-eclipse. See description in Figure 3.9 and in the text.

Figure 3.13: Post-Eclipse observations. See description in Figure 3.9 and in the text.

Table 3.4: χ^2 for reconstructed images.

Epoch	Width (pixels)	BSMEM	MACIM
2008-09	...	...	...
2008-11	128	1.02	...
2008-12	...	...	...
2009-11	200	0.88	0.98
2009-12	200	0.79	1.04
2010-02	200	2.56	1.78
2010-08	200	0.69	0.86
2010-09	200	1.65	1.78
2010-10	200	1.25	1.49
2010-11	200	1.10	1.59
2010-12	200	2.94	3.19
2011-01	200	0.91	1.11
2011-09-17	200	3.02	2.92
2011-09-24	200	0.54	0.54
2011-10	200	1.51	1.30
2011-11	200	1.05	1.19

3.9.2 Image artifacts

Although the large-scale structures in the reconstructed images were likely correct, the finer details could be artifacts introduced by the image reconstruction process. In Figure 3.14 we label our initial assumptions that the polygonal appearance of the F-star was due to UV coverage, the dark spot seen in the northern hemisphere was an alias of the eclipsing body covering the southern hemisphere, and the bright spots in the northern hemisphere were purely artifacts of the reconstruction process.

Figure 3.14: Possible artifacts in the interferometric images

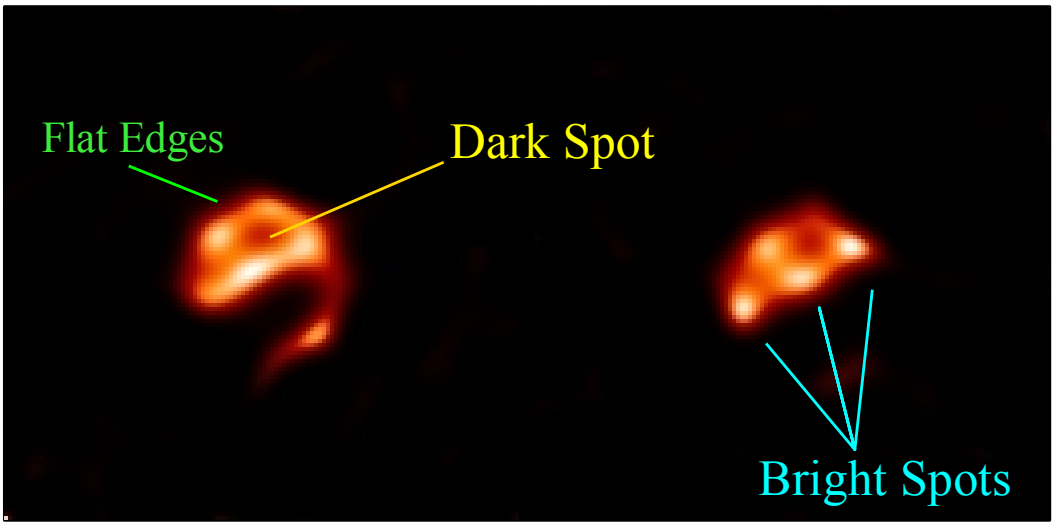

To test these assumptions we qualitatively compare the appearance of the BSMEM and MACIM images in Figures 3.9 − 3.13. BSMEM operates by searching through the parameter space using a gradient-based approach. It enforces image smoothness by way of an entropic function. This algorithm has consistently performed well in the Optical Interferometry Beauty contests discussed earlier. The MACIM method attempts to find the global optimum image using Bayesian techniques. The algorithm uses a Markov Chain approach to activate various pixels in the image and uses the joint probability of the images to maximize the *a posteriori* probability of the image. Because these programs use such different approaches to reconstruct the images, any features in common between both images are likely real. Both BSMEM and MACIM use entropic principles to "fill in" missing information in the images. This permits features below the formal resolution of the interferometer to be recovered (for a practical example of this affect, see Renard et al. 2011).

Inspection of the images revealed that both programs are capable of recovering details that are far below the formal resolution of CHARA. This was mostly due to the entropic functions used in both programs. Interestingly both sets of images

imply the F-star was not round. To test the validity of the suspected artifacts, we constructed model images using the program discussed in Kloppenborg et al. (2010) using the best-fit parameters from *SIMTOI*. Model images from this older software consist of a limb-darkened F-star and an 2D elliptical model for the disk which has Gaussian-smoothed edges. The resulting images were Fourier transformed and sampled in the same UV locations as the actual data. To simulate the interferometric observation process, the nominal values of the visibility, triple amplitude, and closure phases were randomly redistributed following a Gaussian whose characteristic size was determined by the uncertainties in the real data. Then, we reconstructed the resulting data using both BSMEM and MACIM.

Figure 3.15: Image artifacts seen in reconstructions of the real and simulated data for the 2010-09 data set. The 0.5 *mas* resolution at CHARA is indicated by the white circle in the model image. Images have a pixellation of 0.05 *mas*/pixel. Images have a pixellation of 0.05 *mas*/pixel. Any features seen in the simulated image that are not present in the model are likely artifacts. Any features seen in the real image that are not in the simulated image may be real.

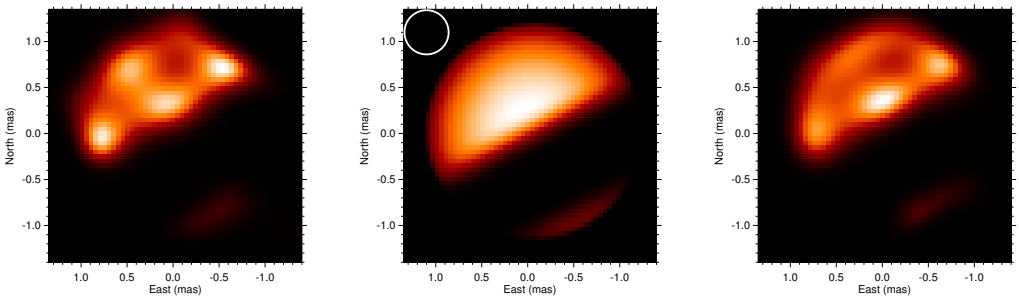

(a) Real Image (b) Model (c) Simulated Image

In Figure 3.15 we present reconstructions of the 2010-09 data for qualitative discussion. The BSMEM and MACIM images were very similar so we present only the BSMEM images here. It appears the three bright spots along the equator and the dark feature in the northern hemisphere were likely artifacts of the image reconstruction process. Our expectation that the straight-edged features on the F-

star were caused by UV sampling was not confirmed. Lastly, the appearance of the bright spot at the tip of the southern hemisphere appeared to be real even though its thickness is far below the formal resolution of CHARA.

Figure 3.16: Image artifacts seen in reconstructions of the real and simulated data for the 2010-02 data set. See description in Figure 3.15

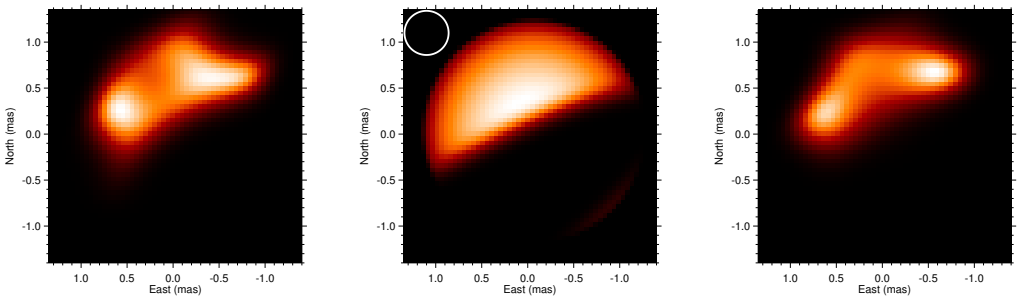

(a) Real Image (b) Model (c) Simulated Image

Figure 3.16 presents intriguing results. The images reconstructed from the real data imply that the southern hemisphere was fully covered by the eclipsing object which qualitatively agrees with a minimum seen in photometry. We have found that the UV coverage in this data set (the equivalent of two 4-telescope observations) cannot reproduce the southern spot in our model; however, given the limited coverage we believe the image fidelity was too poor to trust this "missing feature."

Finally we would like to discuss the post-eclipse images seen in Figure 3.13. In most of these images there is a central bright spot. An identical feature has been seen in other MIRC images (Parks and Che, private comm.) and was likely due to some calibration issue introduced when the combiner was upgraded to six telescopes. With our collaborators, we are presently exploring the cause in greater detail.

3.9.3 Modeling

The ϵ Aurigae system has been modeled using *SIMTOI* with the *MultiNest* minimizer. At the time of this writing, anti-aliasing and transparency were recently

added features that have not been throughly tested, therefore both of these features were disabled for the work herein. In all of our models, we have used 128x128 pixel images with a pixellation of 0.025 *mas*/pixel.

When the PTI data were fit, we modeled the F-star as a sphere of diameter d with no limb darkening, effectively yielding a numeric uniform disk model. For the CHARA data, the F-star was again a sphere of diameter d to which the Hestroffer limb darkening law was applied as described above, yielding the limb darkened diameter, LDD, and limb darkening coefficient, LDD_α.

The CHARA eclipse epochs were much more complex. During the eclipse, one of the disk models as described in Section 3.8.2 was used to represent the eclipsing object. Common parameters for the disk are the disk height H_{Disk}, disk diameter D_{Disk}, and disk decay factor β_{Disk}. In order to construct reasonable models, we needed to establish bounds to minimize the computational investment. Using the results from Kloppenborg et al. (2010) as an initial guide, we limited the F-star angular diameter to $1 < \theta_{\mathrm{LDD}} < 3$ *mas* with a limb darkening coefficient $0.1 < \mathrm{LDD}_\alpha < 1$ and fit all of the out-of-eclipse epochs individually.

The interrelated nature of the orbital parameters presented an additional level of difficulty. We began by manually selecting a set orbital parameters (the position angle of the ascending node, Ω, the total orbital semi-major axis, α, and the orbital inclination, i) that resulted in an eclipse that closely resembled the interferometric images. Holding α and i constant, we established bounds on Ω by simultaneously fitting all totality data. Next, we freed α and i and fit the ingress data. Because no prior studies could comment on α, we used the smallest and three times the greatest values of α_1 from literature (Strand 1959, van de Kamp 1978) as an initial guess for α. For illustrative purposes, I plot the light curves resulting from the cylindrical model with slight modifications to various model parameters in Figure 3.17.

The final bounds on the parameters used in modeling are $2.0 < \mathrm{LDD} < 2.5$, $0.3 < \mathrm{LDD}_\alpha < 1.0$, $3.0 < D_{\mathrm{Disk}} < 20$, $0.10 < H_{\mathrm{Disk}} < 1.5$, $85 < i < 95$, $10 < \alpha < 50$, and $295 < \Omega < 305$. The bounds on the disk decay factors (for disk models A-C) were set with generous initial bounds and later constrained by minimization.

3.9.4 Orbital parameters

Our first objective was to determine the orbital parameters for the system. To do this, we used *SIMTOI* and *MultiNest* along with the cylindrical disk model. By a "χ by eye" method we found an arbitrary α and D_{disk} that closely replicated the eclipse shape. Given prior knowledge from the interferometric images, this was a relatively simple task. Then we ran the *MultiNest* minimizer in *SIMTOI* to identify the best-fit stellar diameter, limb darkening coefficient, disk height, and position angle of the ascending node, Ω, across all totality epochs. We permitted i to freely float within the aforementioned bounds. *MultiNest* found a single global minimum which is summarized in Table 3.5. By modeling all of the eclipse epochs simultaneously, we were able to use the joint probability distribution to place tighter constraints on the orbital parameters than any single epoch alone.

Table 3.5: Totality model, global solution for all epochs. The limb darkening coefficient, LDD_α, is described in Equation 3.8.1.

Model	LDD_H (mas)	LDD_α (mas)	H_{Disk} (mas)	Ω (deg)	$\log Z$
Cylinder	2.279 ± 0.025	0.66 ± 0.01	0.756 ± 0.025	297 ± 1	8813

Figure 3.17: Light curves resulting from different model parameters. Here we have used the Cylindrical model for the disk and modified (a) the total orbital angular semi-major axis, α, (b) the disk height, h, (c) the tilt of the disk with respect to the orbital plane θ, and (d) the inclination of the orbital plane, i.

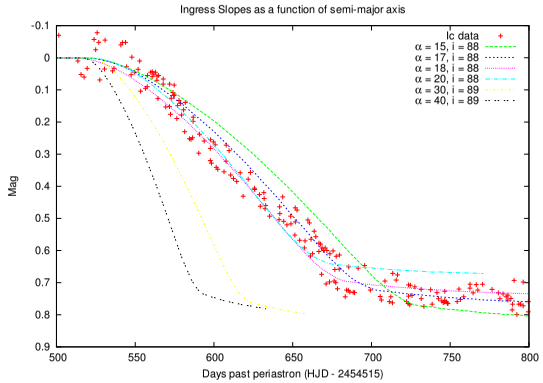

(a) Orbital semi-major axis, α

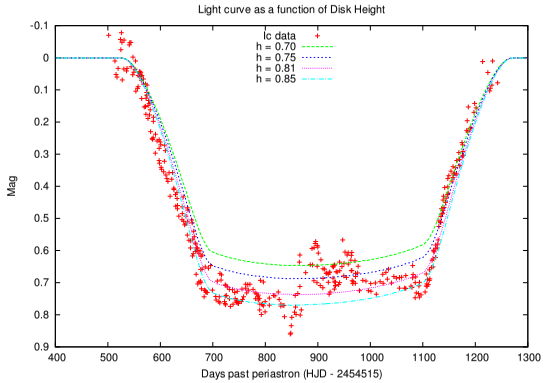

(b) Disk height, $h_{\rm disk}$

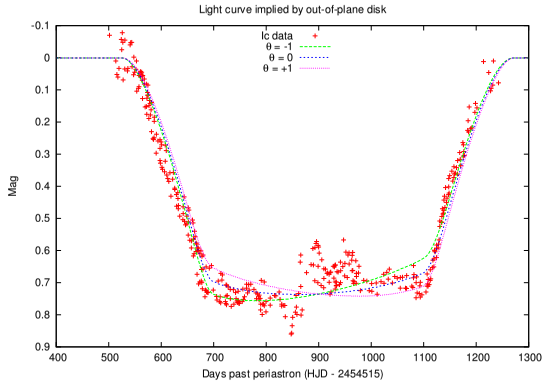

(c) Out-of-plane disk θ

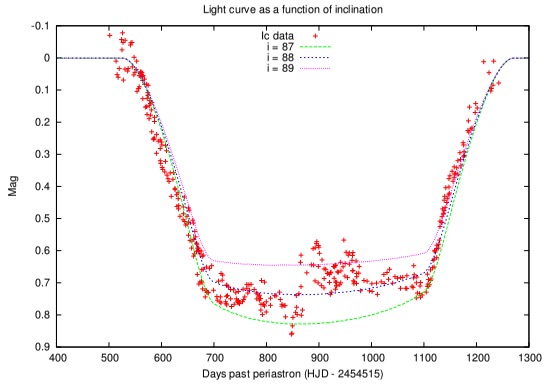

(d) Orbital inclination, i

We note that the uncertainties obtained from *SIMTOI* seemed unreasonably small, sometimes being on the order of tens of micro-arcseconds. An inspection of the likelihood space sampled by *MultiNest* revealed a potential cause. In a simple model consisting of a limb darkened star, several local minima appear within the last $\Delta \log Z \sim 10 - 100$, whereas no similar effect was seen in a uniform disk diameter star. Through much experimentation, we found the location of the minima were altered by the anti-aliasing level (None to 16x16). A higher anti-aliasing level led to fewer minima, but also introduced jump discontinuities ($\Delta \log Z \sim 1$ steps) in the likelihood. We believe both of these issues were artifacts of mixing discrete (i.e. pixel-based) and continuous (e.g. limb darkening parameter) probability spaces without properly accounting for this fact. We are actively discussing this issue with the developers of *MultiNest* to see if their minimizer may be written to account for this scenario. In the meantime, we rounded the uncertainties up to at least the equivalent of one pixel.

With the position angle of the ascending node fixed at $\Omega = 298$ degrees, we fit the ingress epochs (2009-11, 2009-12) with the cylindrical and "Disk B" models. The results are summarized in Table 3.6.

As discussed above "Disk B" modifies the cylindrical model by creating a protruding edge whose hight decays as a Gaussian. Operating under a Bayesian framework, the additional complexity introduced in this model was automatically penalized through the Bayesian prior. The resulting $\log Z \sim 14500$ for "Disk B" not only implies that this additional parameter was justified, but that this model was *significantly* favored over the cylindrical model.

Table 3.6: Ingress Models, global solution for all epochs. The limb darkening coefficient, LDD_α, is described in Equation 3.8.1.

Model	LDD (mas)	LDD_α	D_{Disk} (mas)	H_{Disk} (mas)	β_{Disk}	i (deg)	Ω (deg)	α (mas)	$\log Z$
Cylinder	2.309 ± 0.025	1.000 ± 0.01	5.458 ± 0.025	0.333 ± 0.025		86 ± 1	298 ± 1	10.173 ± 0.025	5946.143
Disk B	2.348 ± 0.025	1.000 ± 0.01	9.920 ± 0.025	1.104 ± 0.025	1.971 ± 0.01	89 ± 1	298 ± 1	36.277 ± 0.025	14466.103

It was instructive to compare the parameters for the F-star and disk between the ingress and totality model fits. In totality we see the F-star was 2.270 ± 0.025 *mas* in diameter and had a limb darkening coefficient of 0.66 ± 0.01. During ingress, the models imply the F-star grew by $0.03 - 0.09$ *mas* and also acquired a significantly higher limb darkening coefficient. Along with this, the disk thickness changed considerably. Both of these effects were certainly not real. If they were, the interferometric images would be noticeably different! We postulate that the hard-edge of both disk models does not adequately represent the leading edge of the disk. Therefore, the minimizer attempted to compensate by "fuzzing" out the F-star.

Until a better disk model is implemented, we conclude the best-fit orbital parameters are $\Omega = 298.00 \pm 1$ deg, $i = 89.03 \pm 1$ deg, and $\alpha = 36.28 \pm 0.01$ *mas*. In the case of α, the uncertainties were likely underestimated by perhaps a factor of 10. We suggest future disk models incorporate variable opacity in the leading edge of the disk. We also suggest that the H-band photometric light curve be used as an additional constraint to the orbital parameters because the slopes of ingress and egress uniquely reveal the translational motion, and hence α (see Chapter 4).

3.9.5 F-star parameters

Once the orbital parameters were sufficiently constrained, all interferometric epochs could be modeled using *SIMTOI*. First we fit the pre-eclipse K-band data from PTI using a uniform disk model on a per-epoch basis. Best-fit parameters are displayed in Table 3.7. At first glance the parameters appear quite scattered, which might hint at a cause for the aforementioned photometric variations of the system. In our prior work (Stencel et al. 2008) we found significant variations in UDD between epochs that were not correlated with V-band photometric variations. Additionally, there were night-to-night changes in diameter by up to 0.2 *mas* (8% in diameter). Such extreme changes are likely not due to the F-star itself, but instead due to something

systematic. For instance, bad calibration data for HD 79452 were likely to blame for the unusually small angular diameter reported on JD 2453715.

It is possible to reinterpret the Bayesian evidence to garner an estimate on the quality of the data. Assuming the uniform disk model is appropriate for the PTI data, then $\log Z$ is then a measure of how closely the data fit to the model. From inspection, we assert that diameters with $\log Z \gtrsim 100$ are the most accurate representation of the true F-star UDD.

Nevertheless, Table 3.7 appears to show the F-star UDD is decreasing at a rate of -0.03 ± 0.01 *mas*/yr, or about 1% per year. This is strikingly similar to the 0.6% per year suggested by Saitō and Kitamura (1986). If this contraction is indeed true, the CHARA data should show a decrease in diameter of ~ 0.1 *mas* between the first and last epochs.

Next we modeled the CHARA data using the limb darkened star and "Disk B" for the eclipsing body. Our results are summarized in Table 3.8 with the corresponding UV coverage, visibilities, closure amplitudes, and closure phases in Figures 3.18 - 3.33. Modeling ϵ Aurigae was particularly challenging due to the dearth of information on the eclipsing object itself. At the start of this research, too few system parameters were known to sufficient accuracy to undertake a full hydrodynamical simulation of the disk. Indeed, the best model for the disk came from polarimetry (Kemp et al. 1986) in which it was regarded as a rectangle! Our three-dimensional, time-dependent, astrophysically-informed disk models represent a significant improvement in the study of this object. In the next few sentences we discuss the success and failures of our models.

Table 3.7: K-band PTI uniform disk fits.

JD	Date	UDD_K (mas)	log(Z)	Notes
2450743	1997-10-22	2.354 ± 0.025	14	
2450761	1997-11-09	2.524 ± 0.025	-244	
2451124	1998-11-07	2.231 ± 0.025	-8	
2451142	1998-11-25	2.333 ± 0.046	20	
2451143	1998-11-26	2.659 ± 0.043	-1	
2453715	2005-11-12	1.253 ± 0.080	-36	
2453766	2006-01-31	...		No Cals
2454392	2007-10-19	2.096 ± 0.025	332	
2454393	2007-10-20	2.077 ± 0.025	285	
2454394	2007-10-21	2.301 ± 0.025	-81	
2454431	2007-11-27	2.290 ± 0.025	38	
2454457	2007-12-23	1.982 ± 0.025	44	
2454458	2007-12-24	2.160 ± 0.025	31	
2454512	2008-02-16	2.229 ± 0.049	13	
2454513	2008-02-17	1.846 ± 0.025	12	
2454514	2008-02-18	1.944 ± 0.029	71	
2454756	2008-10-17	2.151 ± 0.025	93	
2454765	2008-10-26	1.960 ± 0.025	-198	
2454778	2008-11-08	2.252 ± 0.025	74	
2454779	2008-11-09	2.520 ± 0.025	-87	
2454786	2008-11-16	1.902 ± 0.025	41	
2454792	2008-11-22	2.110 ± 0.025	34	
2454820	2008-12-20	...		No Cals
2454821	2008-12-21	...		No Cals

The pre-eclipse and post-eclipse F-star data were modeled as a limb darkened sphere according to the models described above. The radius and limb darkening coefficient were both free parameters. This permits potential changes in the star

to be explored. With the exception of 2008-12, this simple model appeared to adequately describe the star, although some non-zero closure phases remain which indicated some form of asymmetry in the object. We think these signatures may be due to spots and/or non-radial pulsation on the F-star. We have yet to test this supposition pending implementation of additional models in *SIMTOI*.

Over all epochs, it appeared that the F-star exhibits large variations in angular diameter and limb darkening that exceed the formal uncertainties on these quantities. As was discussed in the prior section, we believe the minimizer was compensating for some aspect of the system that was not modeled by "fuzzing" out the star (i.e. increasing the limb darkening coefficient).

The data from CHARA provide weak support that the F-star is shrinking. Discounting the 2008-11 data, the change in diameter is -0.03 ± 0.02 *mas*/year with a χ^2 near 2.34. This is in agreement with both the PTI data and the claims of Saitō and Kitamura (1986). A better model for the eclipsing object used with the current data should improve upon the uncertainties, permitting us to establish the current angular diameter of the F-star with higher precision. Combining our data with a few interferometric observations taken in the H-band with six-or-more telescope arrays over the next decade should provide sufficient data to test these claims.

Table 3.8: Fit results for individual CHARA epochs. The limb darkening coefficient, LDD_α, is described in Equation 3.8.1.

Date	JD	LDD_H (mas)	LDD_α	H_{Disk} (mas)	β_{Disk}	$\log Z$
2008-09	2454728.0	2.263 ± 0.025	0.62 ± 0.04			417
2008-11	2454777.5	2.325 ± 0.025	0.65 ± 0.03			3189
2008-12	2454810.0	2.542 ± 0.025	1.00 ± 0.01			892
2009-11	2455138.0	2.365 ± 0.025	1.00 ± 0.01	0.74 ± 0.025	1.774 ± 0.000	8752
2009-12	2455168.0	2.297 ± 0.025	1.00 ± 0.01	0.84 ± 0.025	1.437 ± 0.001	4104
2010-02	2455245.0	2.406 ± 0.025	0.32 ± 0.01	1.17 ± 0.025		844
2010-08	2455430.5	2.279 ± 0.025	0.56 ± 0.01	0.83 ± 0.025		-7806
2010-09	2455465.5	2.287 ± 0.025	0.63 ± 0.01	0.80 ± 0.025		11013
2010-10	2455495.5	2.401 ± 0.025	0.98 ± 0.01	0.84 ± 0.025		3298
2010-11	2455504.5	2.253 ± 0.025	0.32 ± 0.01	0.82 ± 0.025		3645
2010-12	2455542.5	2.328 ± 0.025	0.95 ± 0.01	0.76 ± 0.025		123
2011-01	2455579.5	2.236 ± 0.025	0.30 ± 0.01	0.79 ± 0.025		3749
2011-09-17	2455822.0	2.257 ± 0.025	0.63 ± 0.01			1777
2011-09-23	2455828.0	2.184 ± 0.025	0.43 ± 0.01			4520
2011-10-09	2455844.0	2.264 ± 0.025	0.81 ± 0.01			-4013
2011-11-02	2455868.0	2.240 ± 0.025	0.55 ± 0.01			19963

Figure 3.18: 2008-09 Data, model, and residuals. In the top row from left to right we plot either the V^2 (inset UV coverage), T3 amplitude, or closure phase data vs. baseline length in red and the best-fit *SIMTOI* models (i.e. bottom panels of Figures 3.9 - 3.13) vs. baseline length in green. Notice the y-axis of the V^2 and T3 amplitude plots have linear scale for $y > 0.1$ and logarithmic scale for $y < 0.1$. In the lower panels, we plot the data quantities (with uncertainties) vs. model-predicted values in red along with a 1:1 correspondence line (indicating perfect data to model agreement) in green. Horizontal and vertical scale are maintained across all subfigures in Figures 3.18 - 3.33. In general, the models are in excellent agreement with the data, save some closure phase disagreement which may indicate residual asymmetry in the system.

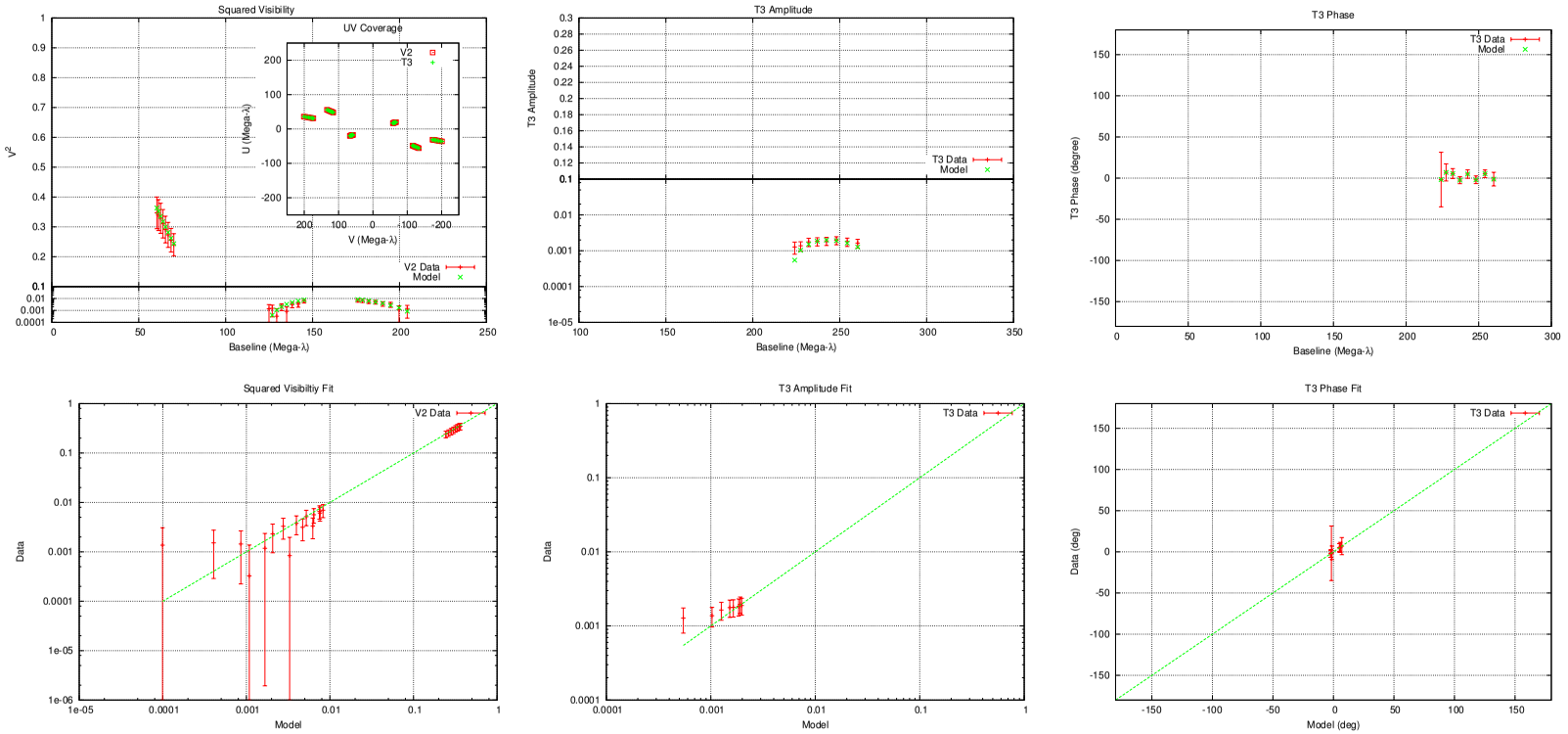

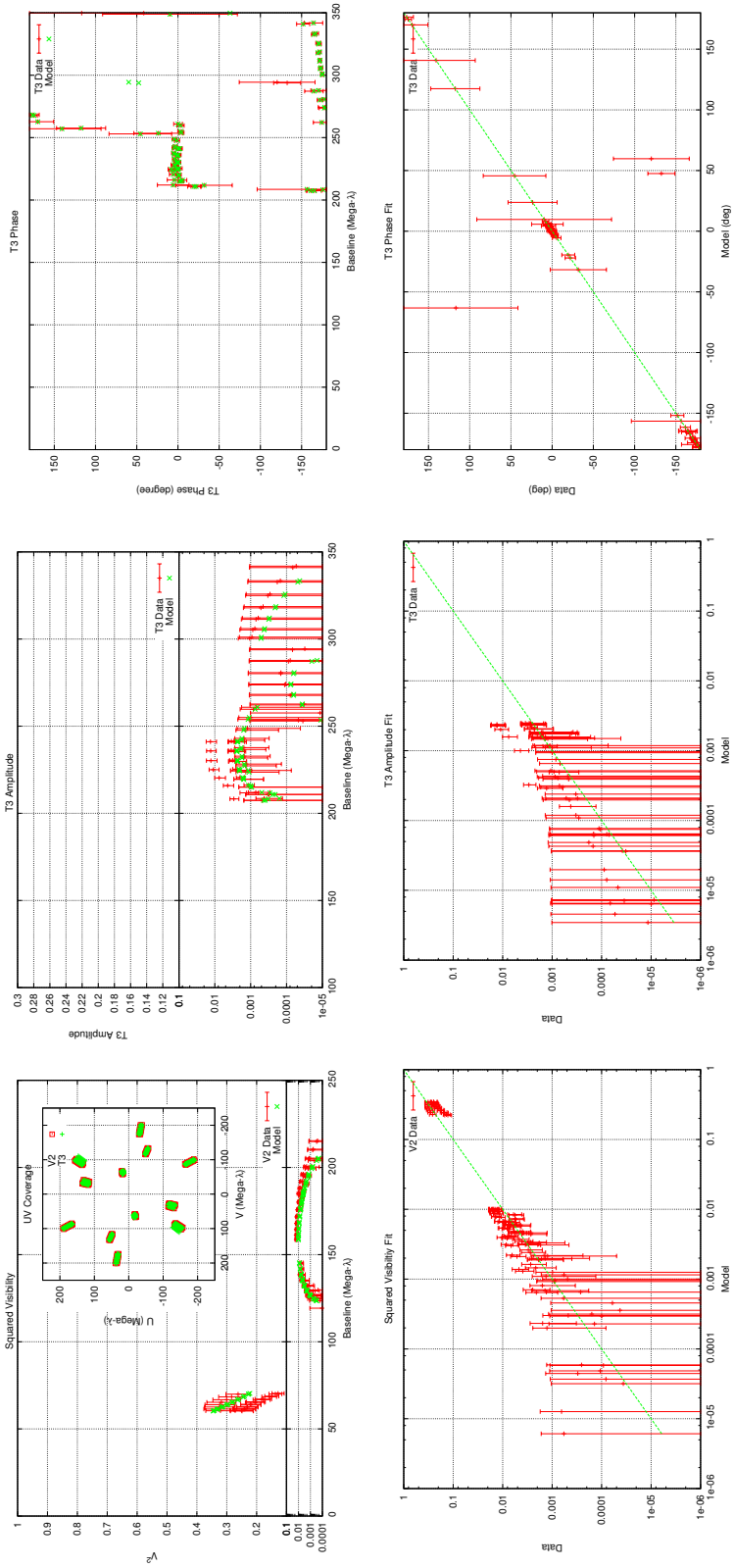

Figure 3.19: 2008-11 Data, model, and residuals. See description in Figure 3.18

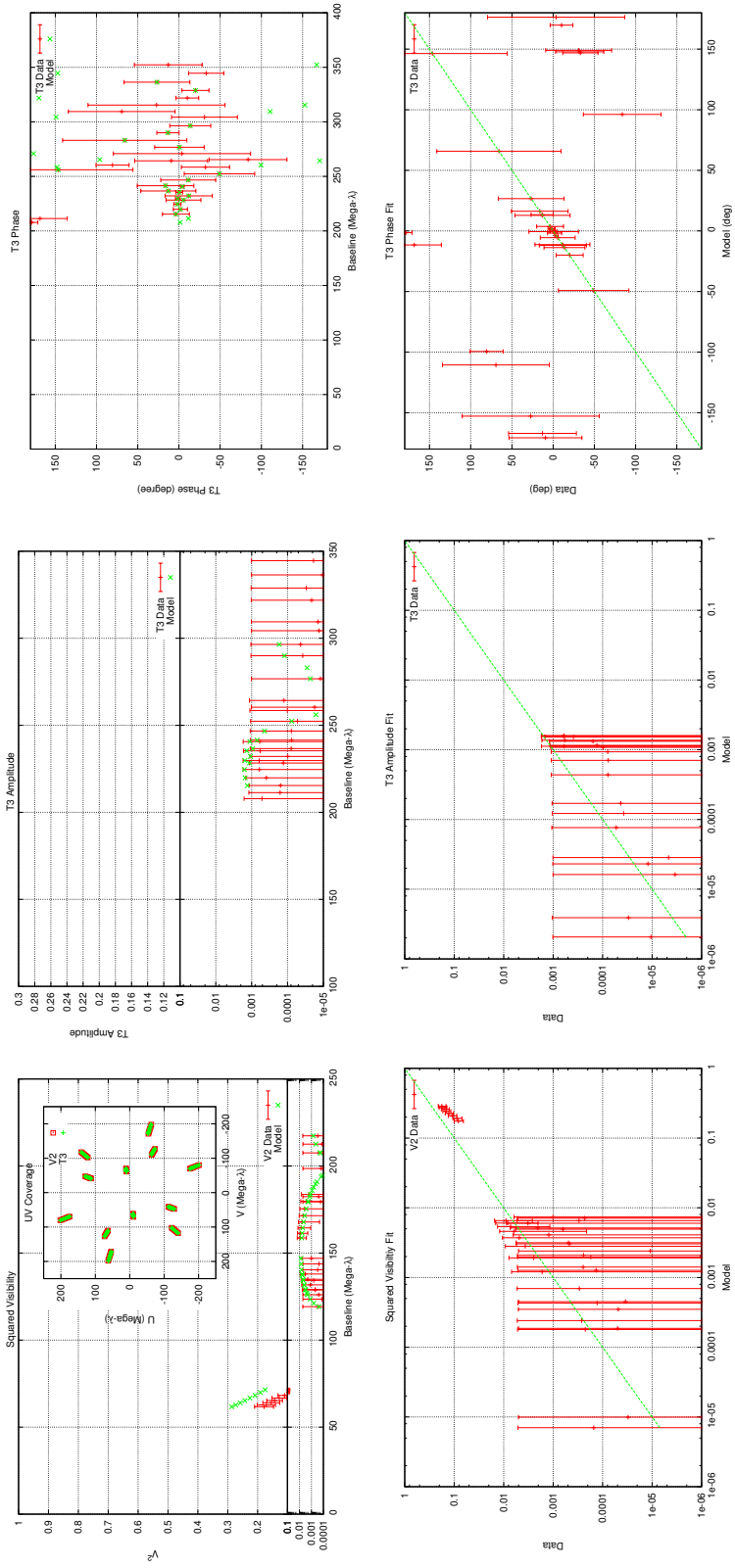

Figure 3.20: 2008-12 Data, model, and residuals. See description in Figure 3.18

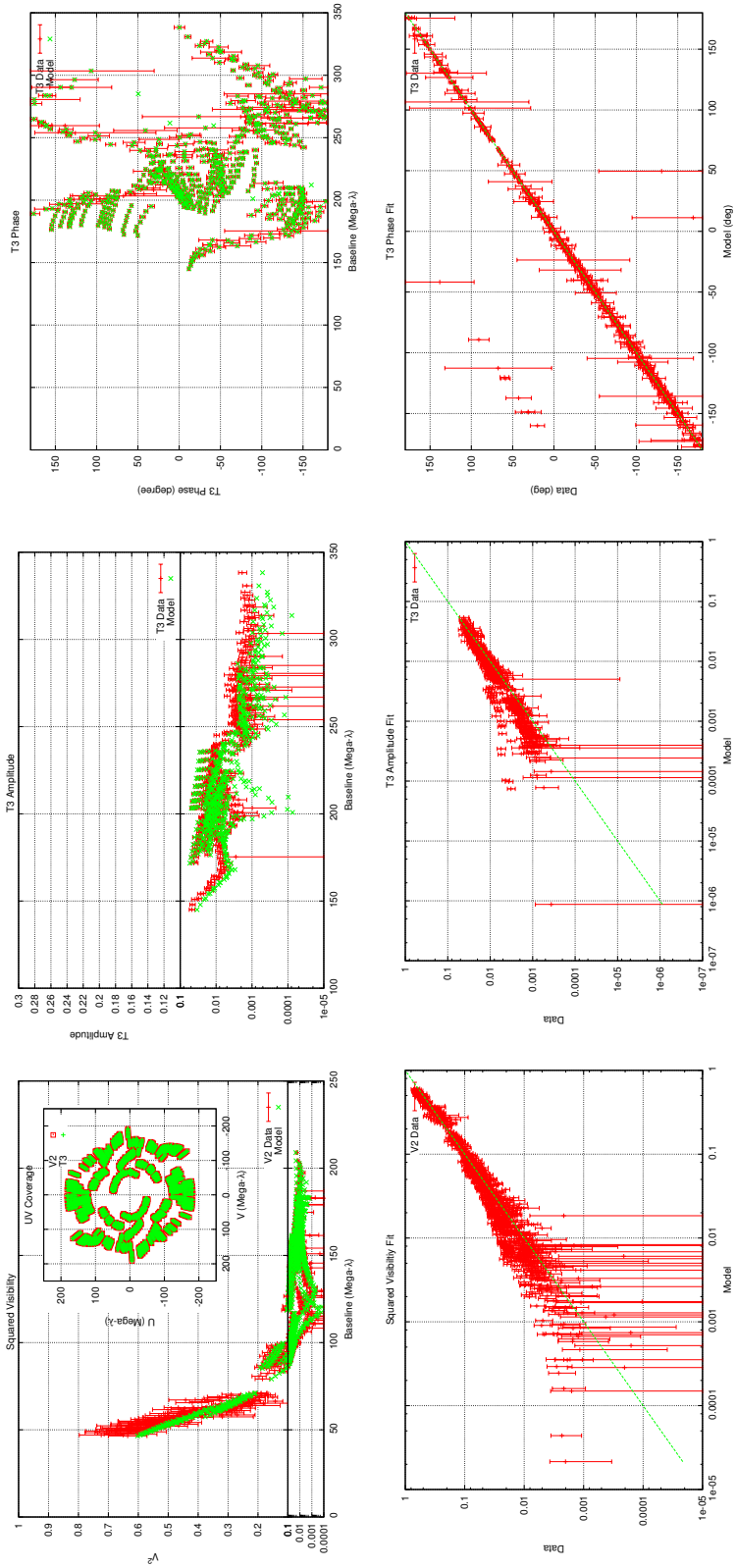

Figure 3.21: 2009-11 Data, model, and residuals. See description in Figure 3.18

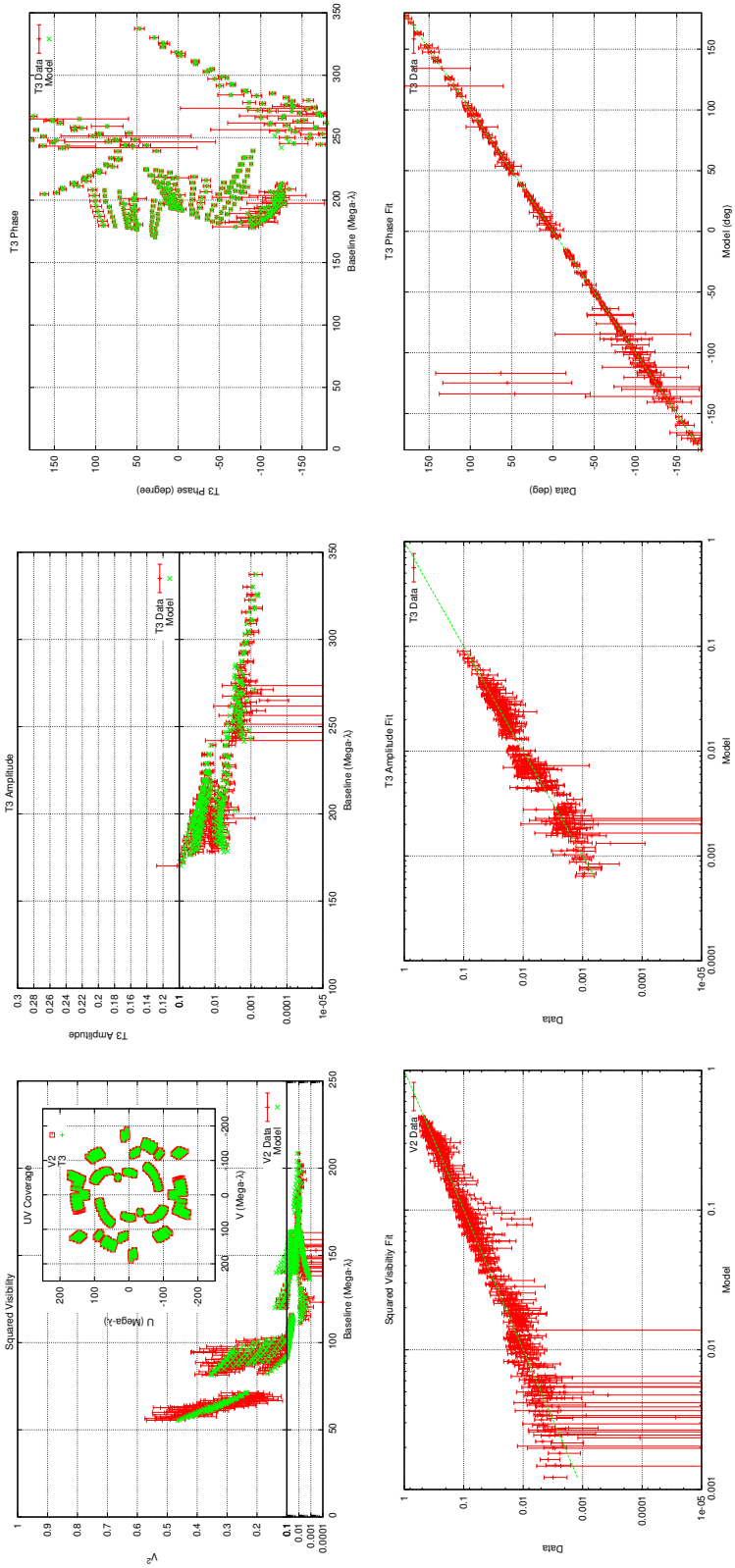

Figure 3.22: 2009-12 Data, model, and residuals. See description in Figure 3.18

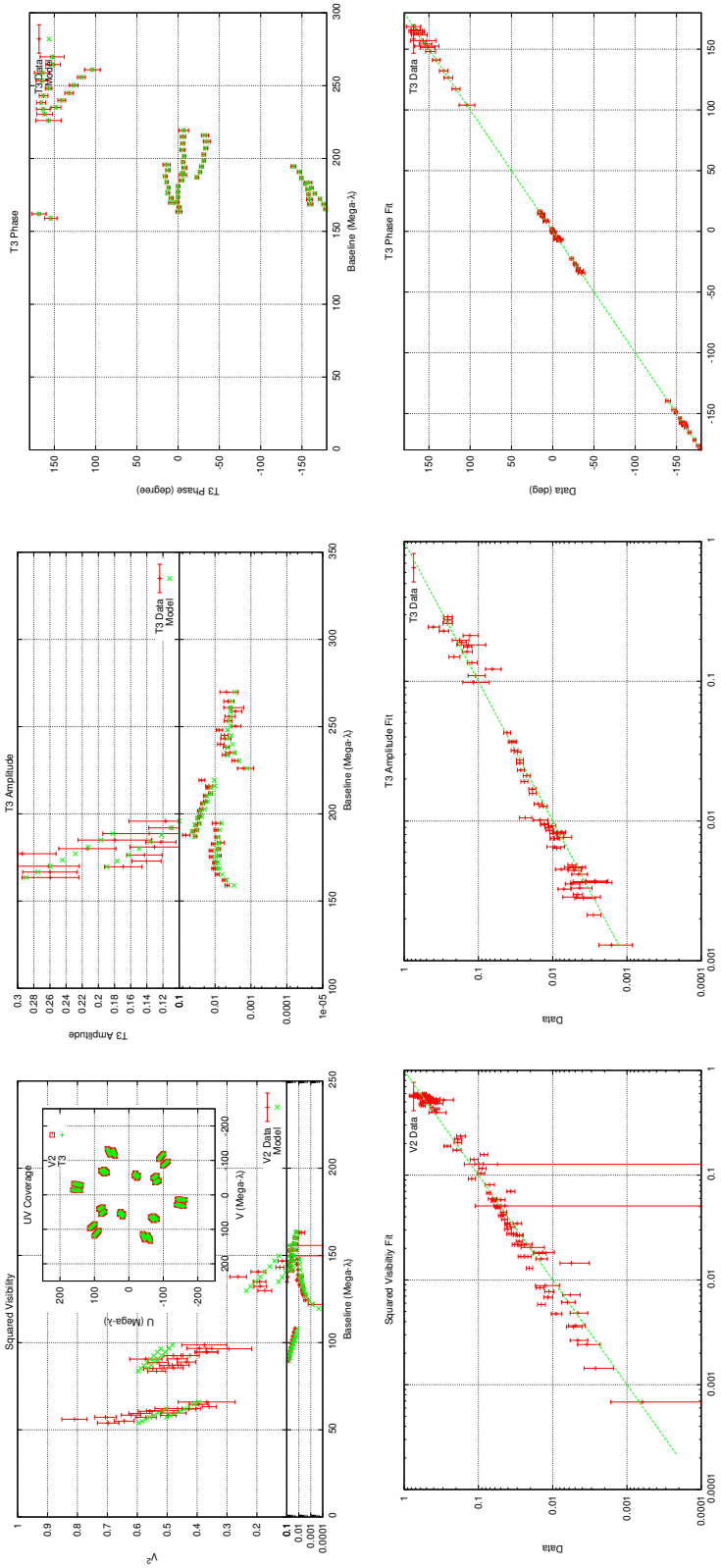

Figure 3.23: 2010-02 Data, model, and residuals. See description in Figure 3.18

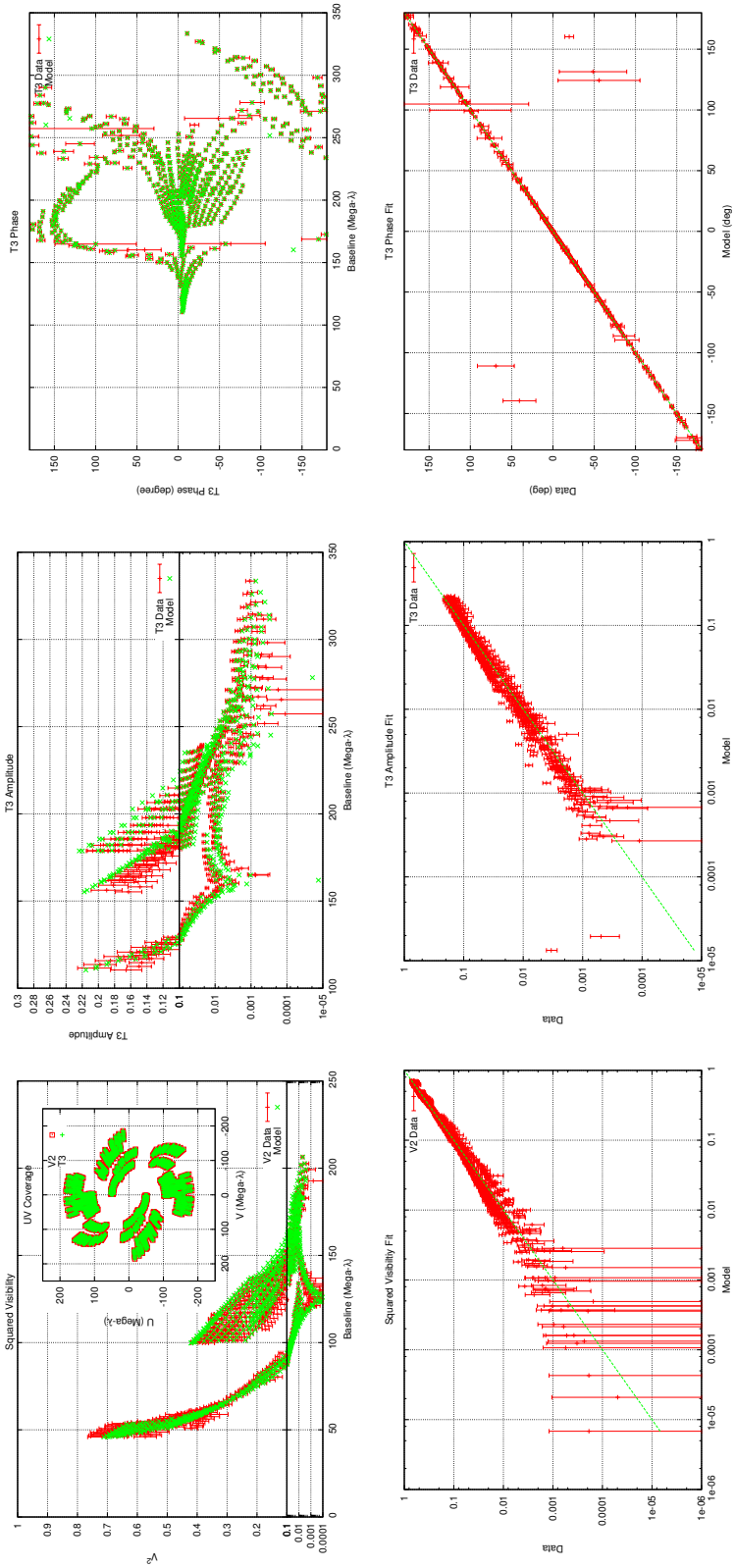

Figure 3.24: 2010-08 Data, model, and residuals. See description in Figure 3.18

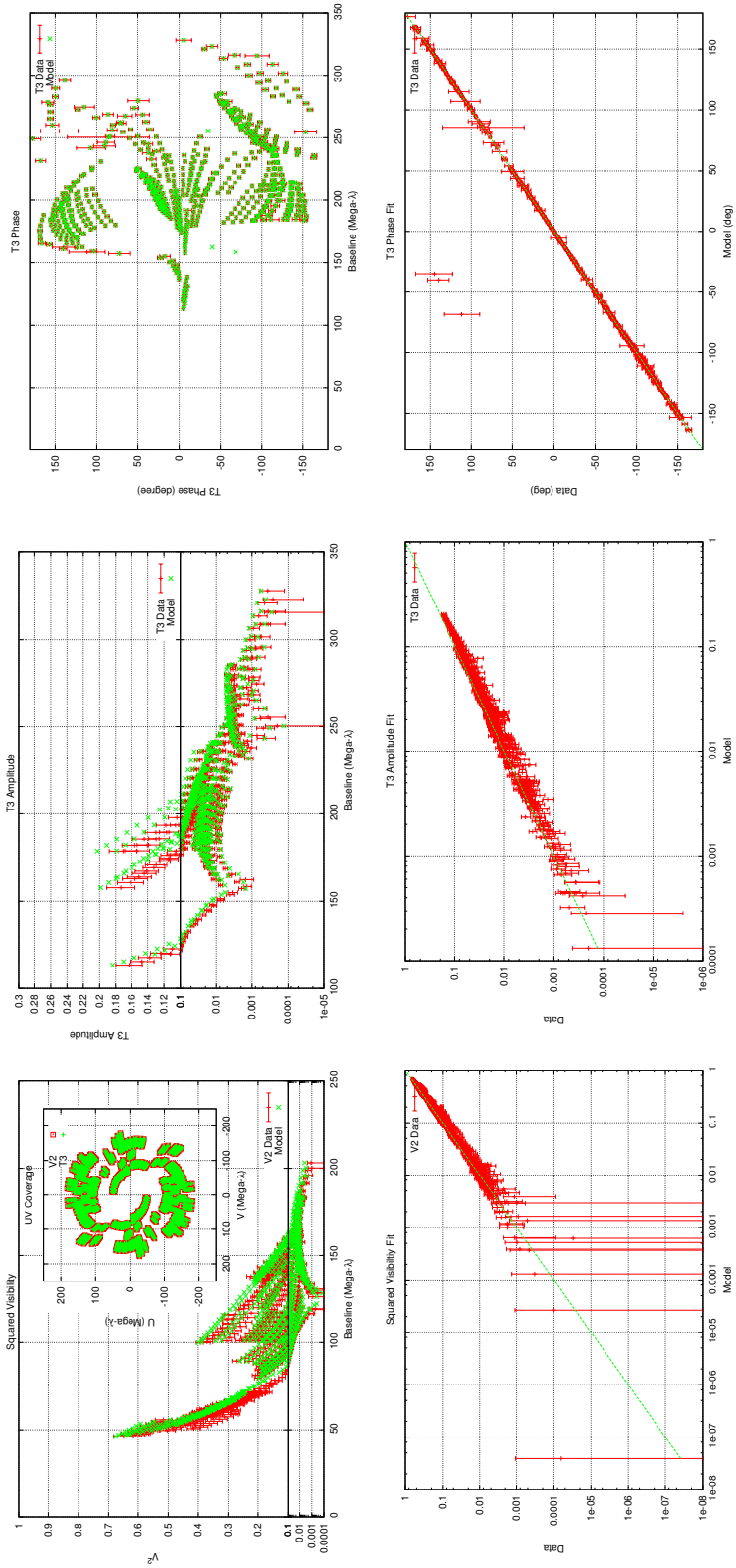

Figure 3.25: 2010-09 Data, model, and residuals. See description in Figure 3.18

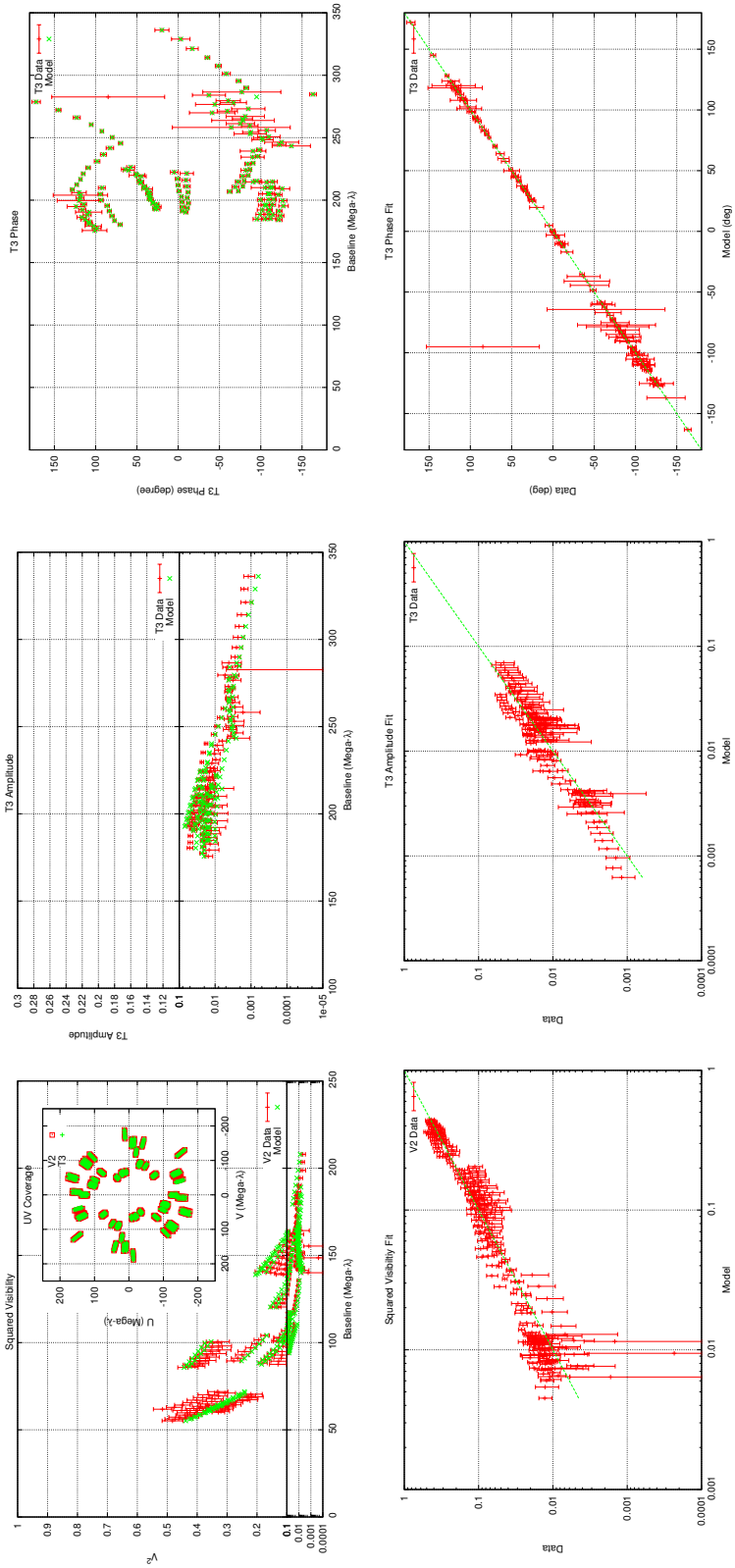

Figure 3.26: 2010-10 Data, model, and residuals. See description in Figure 3.18

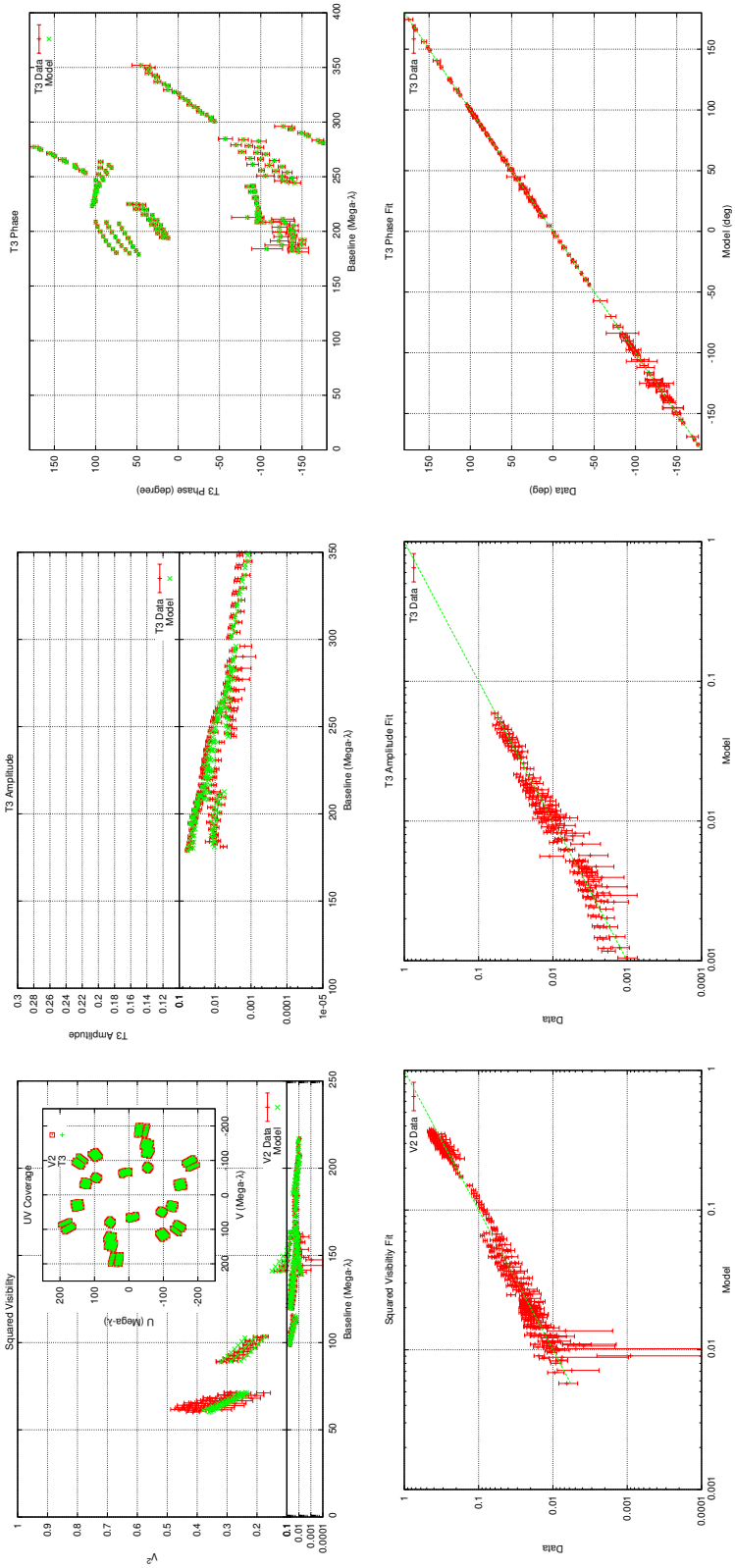

Figure 3.27: 2010-11 Data, model, and residuals. See description in Figure 3.18

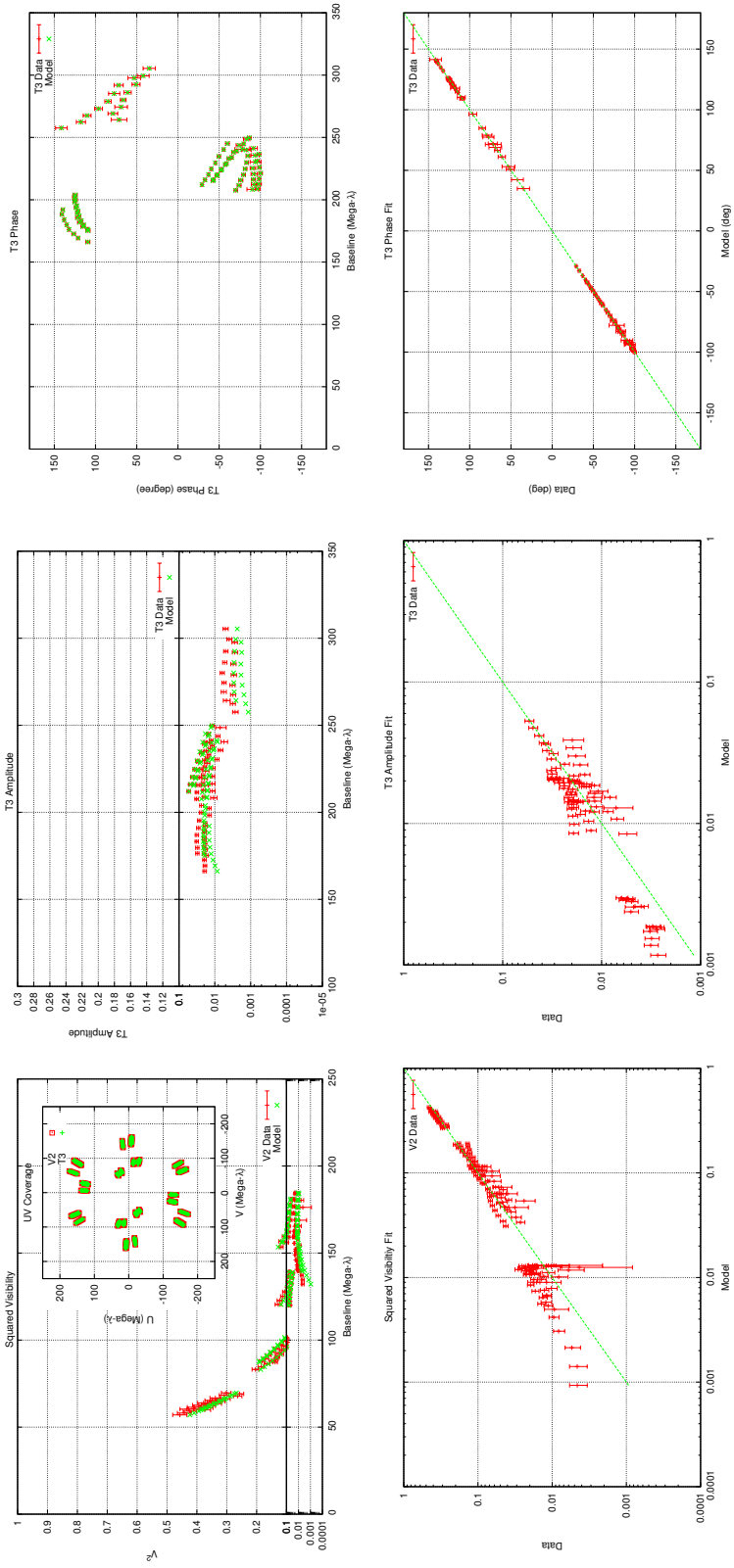

Figure 3.28: 2010-12 Data, model, and residuals. See description in Figure 3.18

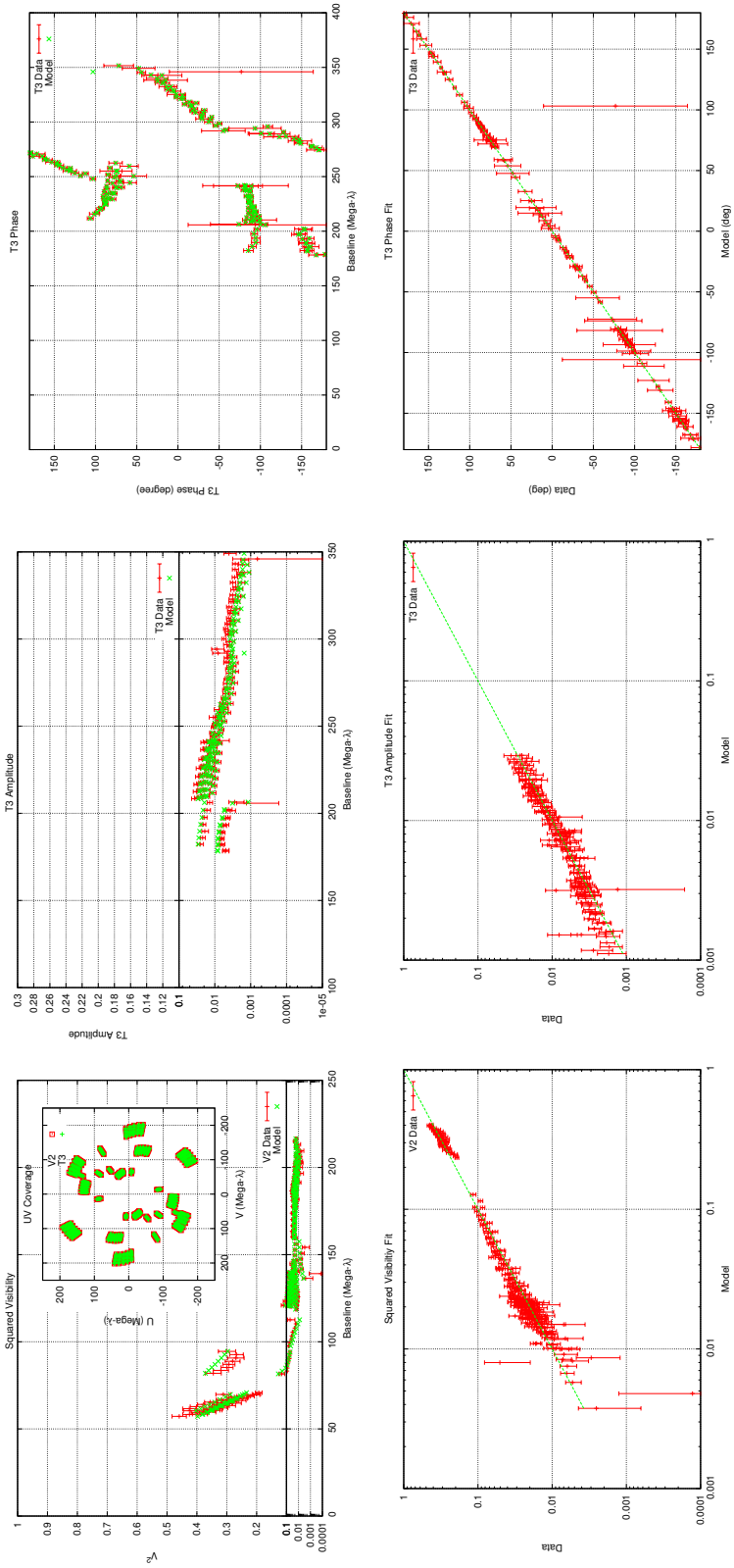

Figure 3.29: 2011-01 Data, model, and residuals. See description in Figure 3.18

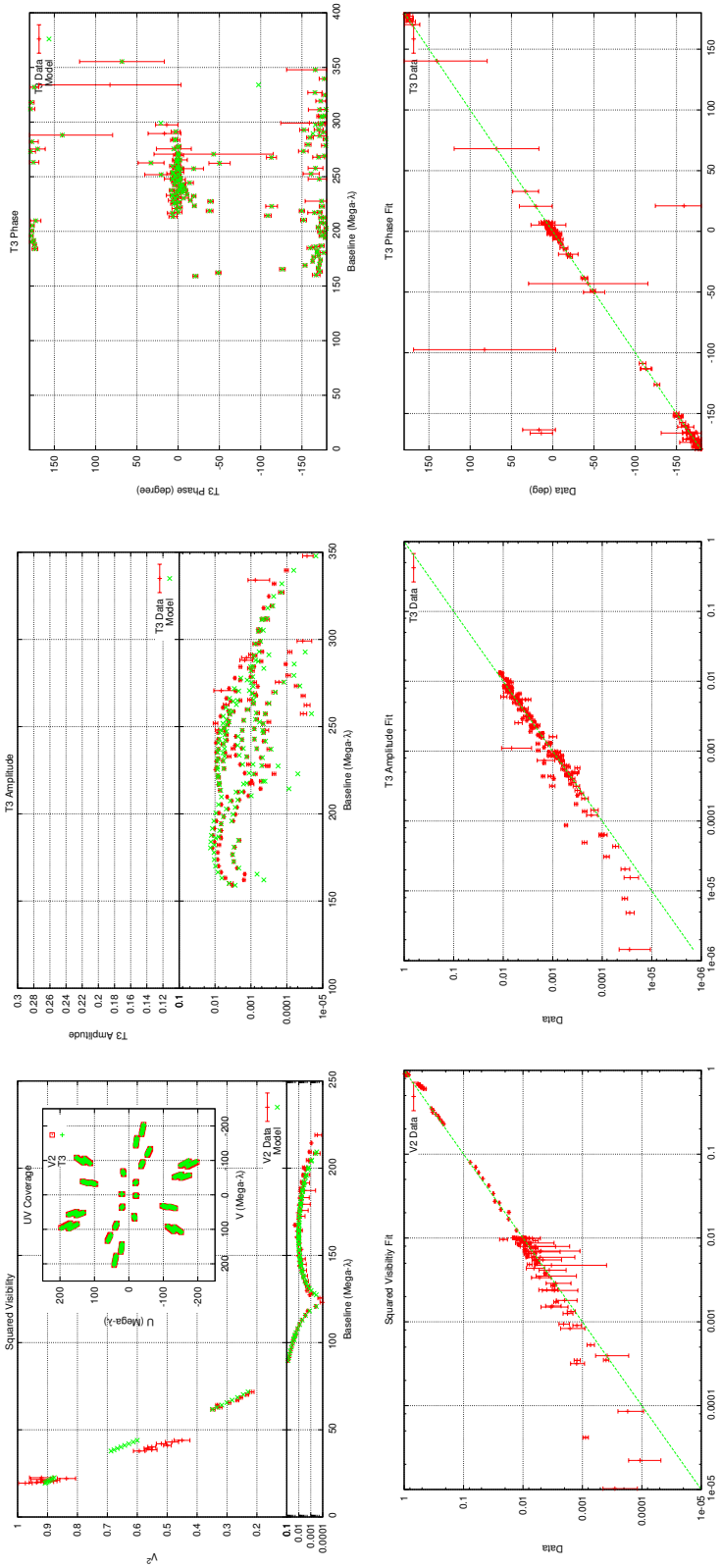

Figure 3.30: 2011-09-18 Data, model, and residuals. See description in Figure 3.18

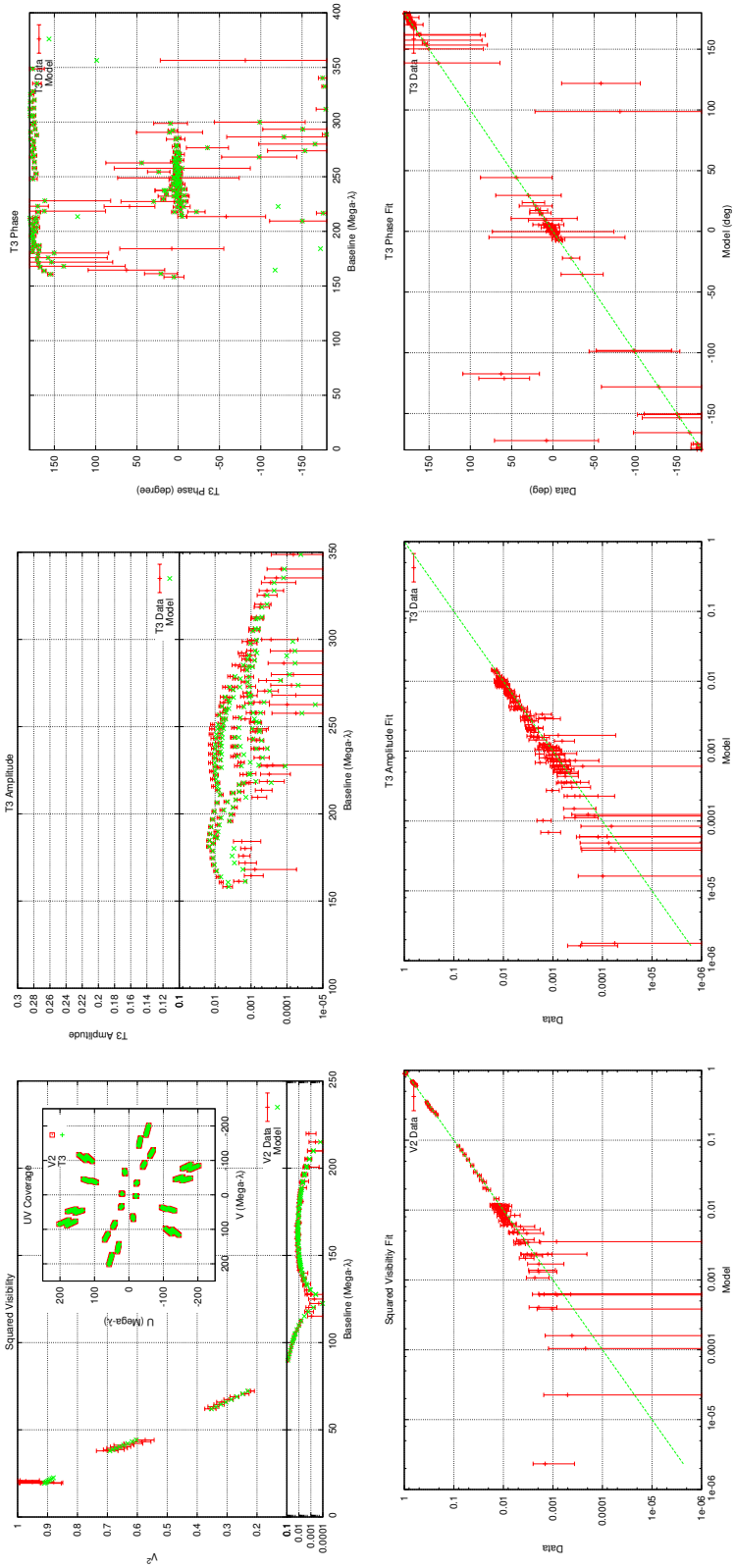

Figure 3.31: 2011-09-23 Data, model, and residuals. See description in Figure 3.18

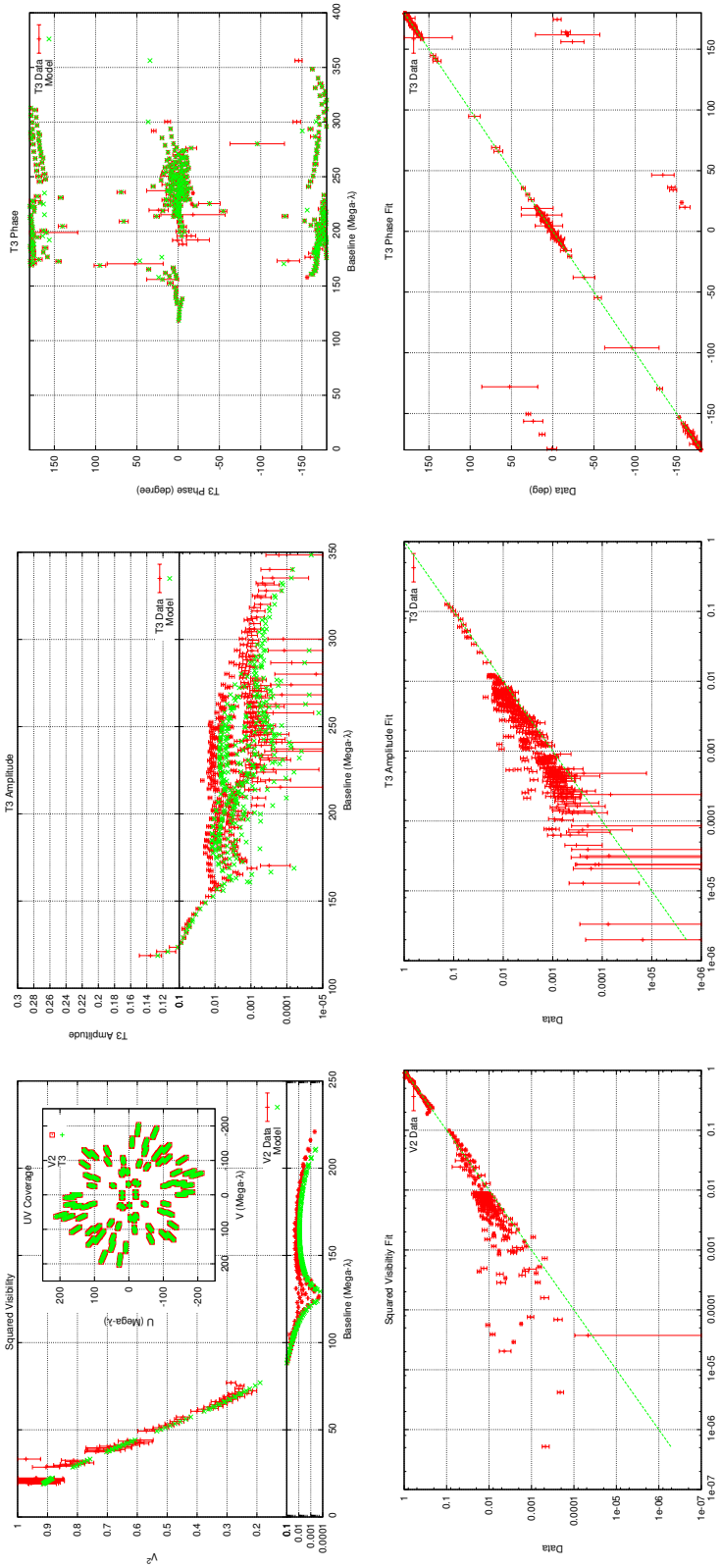

Figure 3.32: 2011-10 Data, model, and residuals. See description in Figure 3.18

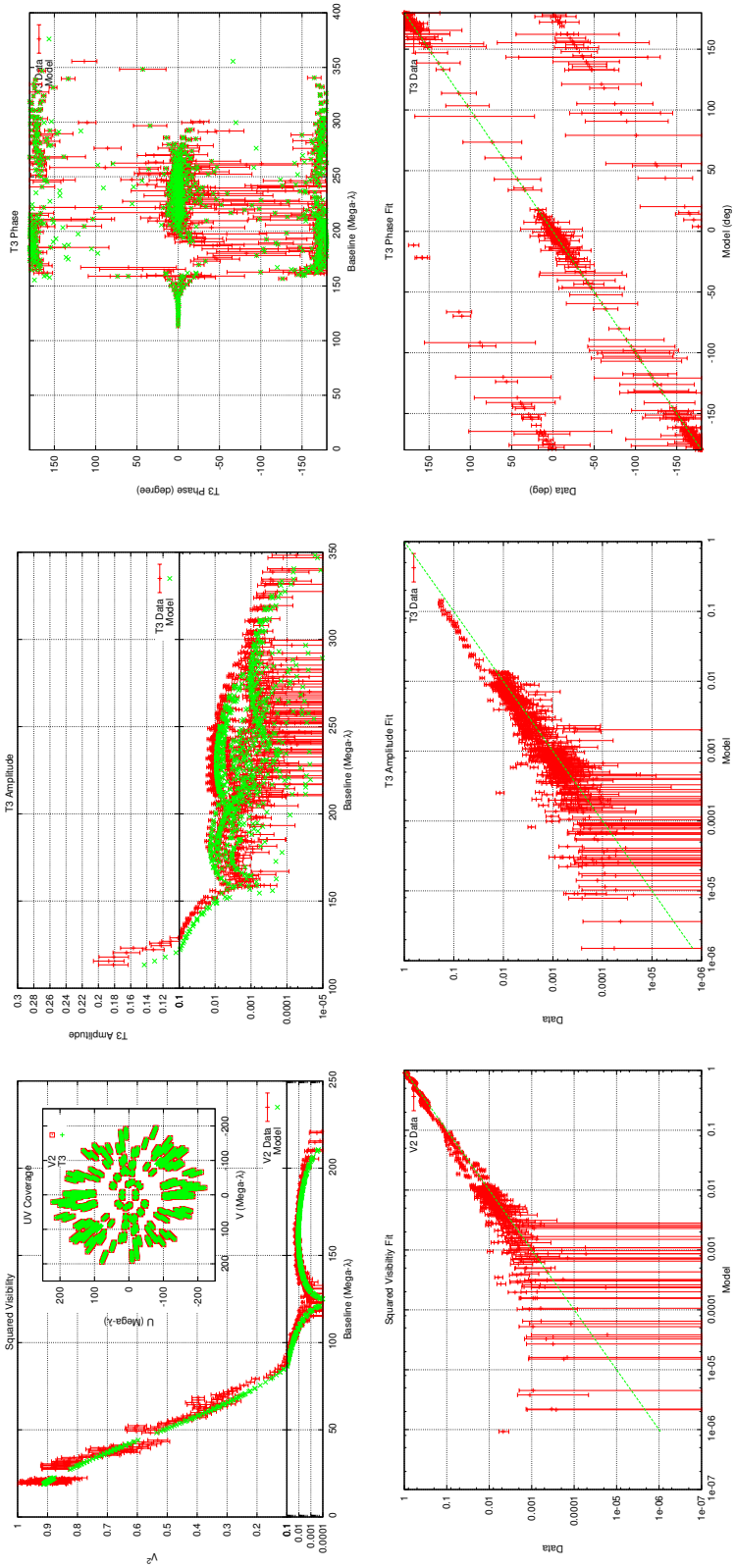

Figure 3.33: 2011-11 Data, model, and residuals. See description in Figure 3.18

3.9.6 Disk parameters

The geometric properties of the disk are quite interesting. First, the entirely opaque region of the disk which we model covers $36 \pm 4\%$ of the F-star. This is slightly smaller than the 53% predicted by light curve modeling (Handbury and Williams 1976). The opaque region of our model (i.e. not including the flared region) subtends $(1.7 \pm 0.05) \times 10^{-16}$ steradians on the sky. If opacity were to be included, this might increase by as much as $\sim 24\%$. This value is four times smaller than the 8×10^{-16} steradians predicted by Backman et al. (1984) using an infrared flux method and a 500K color temperature for the disk. By increasing the temperature of the disk in Backman et al. model, bringing the system closer (see Chapter 4) and including opacity in our model, these differences are likely to be reconciled.

The geometrical decay factor, $\beta_{\rm Disk}$, found in Table 3.8 changes between the two ingress epochs, implying the leading edge does not resemble a traditional astrophysical disk (i.e. one with a Gaussian decaying edge as found in Armitage 2010). Additionally, the disk's height, $H_{\rm Disk}$, flares to nearly half the F-star diameter in 2010-02. Photometry from the eclipse implies the system was up to ~ 0.1 mag fainter in all bands at this time which qualitatively agrees with an increased disk thickness.

As discussed in Chapter 2, the disk *does* appear to exhibit wavelength-dependent extinction. At shorter wavelengths the eclipse depth increases between mid-eclipse and 3rd contact, whereas the flux increases at longer wavelengths. Interferometry agrees with this conclusion in that the H-band thickness of the disk is thicker during ingress than egress. Furthermore, during the second half of the eclipse the disk thickness decreases slightly while the H-band flux increases slightly.

3.9.7 Implied photometry

Using the best-fit eclipse parameters from Tables 3.6 and 3.5 we have generated synthetic light curves using *SIMTOI* and plotted them along with the H-band photometry. One can see in Figure 3.34 that our model does a decent job of replicating the observed light curve. This implies that disk as characterized by our simple geometrical models is a close match for the real astrophysical disk. There are, however, a few discrepancies. Foremost, our model does not replicate the eclipse depth perfectly. We believe this can be alleviated by including a height-dependent opacity in our models. Secondly, our model predicts a flat light curve, whereas there is a clear discontinuity of ~ 0.1 magnitude right before mid-eclipse. We think this may be due to a genuine opacity difference in the disk where the ingress-side is slightly thicker (physically, optically, or both) than the egress side. It is theoretically predicted that radiation-induced sublimation zone may exist on the F-star side of the disk and rotation could result in a pile-up of material somewhere on the ingress side of the disk (Takeuti 2011). Indeed, as mentioned in the results section of Chapter 2, the appearance of molecular features and deepening of absorption lines during the second half of eclipse implies the line-of-sight composition of the disk has changed, therefore a change in opacity or geometry could be expected.

In the aforementioned figure we have manually adjusted the lower trace by increasing the thickness by 0.04 *mas*. As the formal resolution at CHARA is 0.5 *mas* in H-band, we feel this is within reason. From inspection of these plots, it is clear that the second half of the eclipse is up to 0.1 mag brighter. We believe the excess flux seen at these epochs is due to a decrease in opacity, disk thickness, or both. Spectroscopic data show He during mid-eclipse, and CO absorption post-mid-eclipse, suggesting that some physical changes in the disk have occurred.

Figure 3.34: Simulated photometry from the "Disk B" model. The top trace is from the best-fit models, whereas the lower trace is manually adjusted. Units for total semi-major axis, α, total disk height, h, and total disk diameter d are *mas*

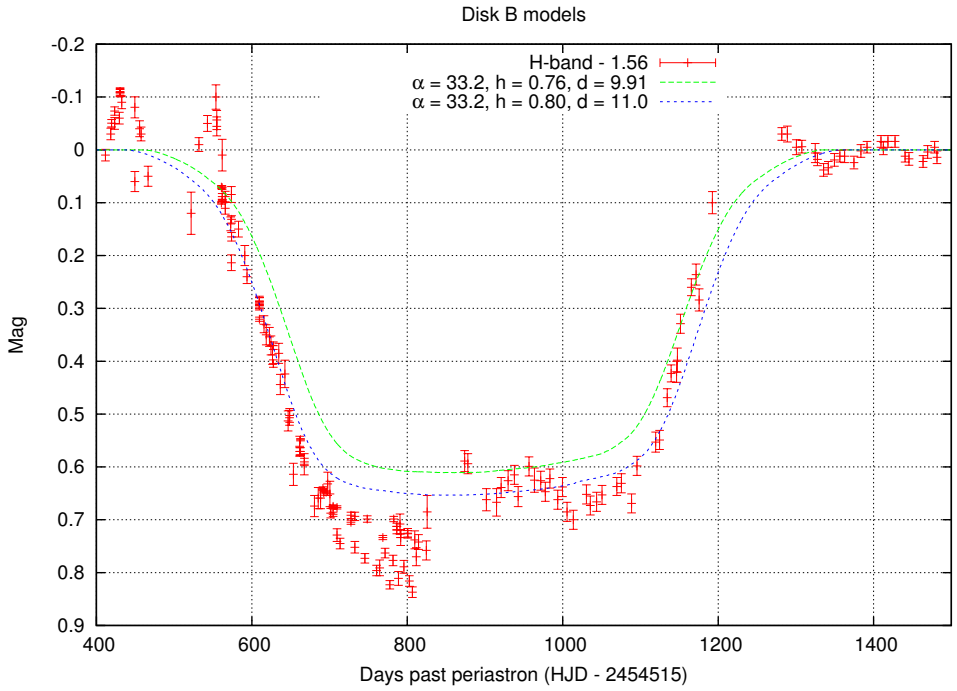

3.10 Conclusion

Using a series of interferometric observations obtained at PTI and CHARA, we have obtained the first interferometric data of ϵ Aurigae during eclipse. We have generated model-independent interferometric images (Figures 3.9 - 3.13) which show the photometric eclipse was likely caused by a disk of material passing in front of the F-star. The images do not support the notion that the eclipse is caused by an inclined disk with rings and a central clearing as was suggested by Ferluga (1990). Indeed, there is no hint of light passing through a central clearing in the 2010-08 image (see Figure 3.11). Note, this does not preclude the disk being composed of concentric rings (indeed, spectroscopic evidence supports the existence of rings), but suggests any rings present will not be observable using present photometric or interferometric techniques.

Our interferometric model fitting derived uniform and limb-darkened disk diameters for the F-star and orbital parameters for the system. We have minor evidence to support the notion that the F-star was shrinking at $\sim 1\%$/year and suggest further interferometric modeling over the next decade to test this claim. Our work also suggests that the disk was asymmetric, being slightly thicker (physically, optically, or both) in the first half of the eclipse and thinner thereafter. This may be a result of a pile-up of material exposed to the F-star's radiation.

Chapter 4

A Complete orbital solution for ϵ Aurigae

In this chapter I discuss new astrometric and radial velocity orbital solutions for ϵ Aurigae using Bayesian statistical methods. From a combination of radial velocity (RV) data and constraints from interferometry, I have refined the orbital elements for this system. I outline a method by which the translational motion of the disk, along with a model for the eclipsing object, can be used to determine the total semi-major axis of the system. We compare our work to the recently derived orbital solutions from Stefanik et al. (2010) and Chadima et al. (2010) and discuss how the differences may be reconciled. In the results section, we present a new combined orbital solution and a new distance estimate for the system. This work has been conducted with much input from Paul Hemenway of the University of Denver, Eric Jensen from Swarthmore College, and Wayne Osborne from Central Michigan University.

4.1 Introduction

With significant evidence in favor of the disk-interpretation for the secondary in the ϵ Aurigae system, our research efforts have focused on determining the evolutionary state of the system. As discussed in Chapter 1, spectroscopic data present conflicting information: the spectroscopic abundance study by Sadakane et al. (2010) indicates the F-star is a "normal supergiant" with only a slight overabundance of s-process material. This is starkly contrasted with the smaller-than-expected ^{12}CO/^{13}CO ratio (Hinkle and Simon 1987) observed *in the disk* which implies ^{13}C has been created and deposited perhaps by a mass transfer scenario. Recent ultraviolet spectral fitting by Hoard et al. (2010) suggests a $\sim 6\ M_{\odot}$star resides within the disk which by way of the mass function forces the F-star to have a mass near $\sim 2.2\ M_{\odot}$, lending support to the post-AGB interpretation.

With such conflicting evidence, clearly the evolutionary state cannot be determined by spectroscopic means alone. Because of this, we sought out an alternative method to determine the component masses of the system. As will be explained in a later section, the total orbital semi-major axis, $\alpha = \alpha_1 + \alpha_2$ can be determined from the interferometric observations. When combined with the F-star's orbital semi-major axis, α_1, the mass ratio $q = \frac{M_1}{M_2} = \frac{a_2}{a_1} = \frac{\alpha_2}{\alpha_1}$ is uniquely determined. By substuting this quantity into the spectroscopic mass function,

$$f(M) = (a_1 \sin i)^3/T^2 = (M_2 \sin i)^3/(M_1 + M_2)^2, \tag{4.1.1}$$

the masse of the the individual components are easily computed:

$$\begin{aligned} M_2 &= \frac{f(M)(1+q)^2}{\sin^3 i}, \\ M_1 &= M_2 q. \end{aligned} \tag{4.1.2}$$

Although mathematically sound, this method relies on excellent estimates for the orbital parameters involved. Interferometry has provided α to sufficient accuracy for our work, but α_1 is poorly constrained. Indeed, estimating $a_1 \sin i$ with any present parallaxes would result in near 100% uncertainty in q (see Table 4.1). The "good" parallax estimates are dynamical parallaxes which are derived by equating the semi-major axes in linear and angular terms. Clearly, this method depends on the assumed/derived orbital parameters which, in many cases, have been proven incorrect by modern work. The three astrometric studies of ϵ Aurigae do provide an estimate of α_1; however, solutions from different observatories disagree at a few-sigma level (van de Kamp 1978, Heintz and Cantor 1994, Strand 1959; see α_1 in Table 4.5).

Table 4.1: Published parallax estimates for ϵ Aurigae

Source	π_{abs} (mas)	π_{dyn} (mas)	Distance (pc)
van Leeuwen (2007)	1.53 ± 1.29		653 ± 551
Heintz and Cantor (1994)	3 ± 2	1.65 ± 0.15	606 ± 55
van de Kamp (1978)	1 ± 1	1.72 ± 0.08	587 ± 27
Strand (1959)	6 ± 3	1	1000
Mitchell et al. (1940)	6 ± 7		
Burns (1932)	-1 ± 7		

Because of these factors, we conducted a joint astrometric and radial velocity solution for ϵ Aurigae. In the following sections we discuss the availability of astrometric data, our data digitization and reduction procedures, and our use of Bayesian statistics. We present our results and discuss the validity of our conclusions in the last two sections.

4.2 Data

4.2.1 Astrometric data

The Sproul Observatory archives contain $\sim$ 1400 photographic plates of ϵ Aurigae taken between 1938 and 1983. When the plates were exposed, a 0.24% sector was used to reduce the brightness of ϵ Aurigae to V $\sim$ 9.6 mag, similar to the surrounding field stars. It is well known that several optical and photographic adjustments were made at Sproul that affect these data (see Hershey 1973, Lippincott 1957) including the installation of a new cell for the 24" objective lens and a change in photographic emulsion in 1949, followed by small adjustments in the optical system between 1957.74 and 1958.03. These adjustments resulted in a well-characterized color-dependent shifts, mostly in Right Ascension (Lippincott 1957) that are easily corrected. In addition to Sproul, the Yerkes observatory archives contain an additional 124 plates taken on 54 nights between 1926 and 1958. Both sets of astrometric data have been analyzed and their results published in prior works (van de Kamp 1978, Heintz and Cantor 1994, Strand 1959) which we summarize in Table 4.5.

Digitizing the original plates was beyond the scope of the current work. Instead we elected to start with intermediate records found in the Sproul Observatory archives. These documents largely consist of computer printouts and hand written notes by van de Kamp which have all been scanned and are available by request. In these materials we located the 301 nightly means published by van de Kamp (1978) along with roughly 45% of the raw ϵ Aurigae plate measurements contained in the archives. All of our plate measurements come from initial measures on the Grant-2 measuring machine whose specifics are discussed in Chapter 2 of van de Kamp (1981). The Grant-2 measures in half-micrometer steps which we call "Sproul Units" (SU). The often-quoted plate scale at Sproul is 18.87 arcseconds/mm or 9.435 *mas*/SU.

The printouts containing the raw plate measurements were digitized using an Optical Character Recognition (OCR) program. The resulting (x, y) positions were plotted and inspected for internal consistency. Then the rotation, scale, and offset values (discussed below) were plotted and visually inspected. Egregious outliers were checked for OCR errors and corrected accordingly. By this method all but 19 exposures (e) on nine plates (p) were validated. Of these, 11 exposures on four plates are an entirely different star field: p65443e1-2, p65444e1-2, p65751e1-3, and p65752e1-4. The remaining eight exposures were correctly digitized, but contain some intrinsic measuring error, therefore these exposures were excluded from our analysis: p561e1, p32027e4, p34589e1-4, p36574e4, p104937e1. It was also found that the plates measured by M.D. Worth (approx. p31619 - p36601) were inserted into the measuring machine rotated by 90 degrees and upside down relative to those measured by M.M. Jackson. It is our intent to publish all of the digitized OCR plate measures in an upcoming publication.

4.2.2 Spectroscopic data

The original radial velocity (RV) measurements come from the Potsdam, Yerkes, Mount Wilson, Dominion Astrophysical Observatory (DAO), Harvard-Smithsonian Center for Astrophysics (CfA), and the Ondřejov Observatories and were compiled in Stefanik et al. (2010), Chadima et al. (2010) and references therein. A discussed in Chapter 2, the F-star exhibits quasi-periodic variations in light and RV with timescales between 60 and 150 days. Although these variations appear to be stochastic, they are easily tracked for one to two years at a time. During the eclipse many of the spectral lines deepen, broaden, and shift due to the rotational velocity and absorption profile of the disk being superimposed on the F-star's spectrum. The combination of these two affects led Stefanik et al. (2010) to exclude all of the data from the eclipse intervals plus an additional 200 days before ingress and after egress,

resulting in a loss of nearly 1,100-days from the orbital solution. Here we have focused on enforcing the continuity of the out-of-eclipse variations while excluding the superimposed profile variations in order to include more data in our RV fit.

The tenuous nature of the disk's atmosphere ensures that only the low-excitation spectroscopic lines exhibit profile variations (see, Struve et al. 1958, Barsony et al. 1986, Lambert and Sawyer 1986) during the eclipse. Indeed, there is a noticeable difference between high and low-excitation lines of some atomic species. Therefore we have inspected the original sources of data to determine which, if any, data should be excluded. In detail 1901 - 1903 eclipse, JD 2,415,294 - 16,362; the publications corresponding to these data averaged over many spectral lines, therefore all data in these ranges is excluded. In the 1928 - 1930 eclipse, JD 2,425,193 - 26,261; the data appears to be unaffected except the range 2,425,804 - 26,032 where the data are highly scattered. During the 1955 - 1957 eclipse, JD 2,435,091 - 36,158; the data from Struve et al. (1958) are listed separately, therefore the low-excitation lines (often outside of $-10 < \mathrm{RV} < 15$ km/s) were excluded. In the 1982 - 1984 eclipse, JD 2,444,973 - 46,041; the contributions from individual spectral lines are labeled and again the low excitation lines of Na and KI were eliminated. This essentially excludes the contributions from Barsony et al. (1986) and Lambert and Sawyer (1986) in this interval. Lastly the start of the 2009 - 2011 eclipse, JD 2,454,880 - 55,948 is well documented. The CfA spectra (Stefanik et al. 2010) feature the rotational motion of the disk and were excluded during this interval from our analysis.

Additionally the Hα line is known to be complex and highly variable (Cha et al. 1994, Schanne 2007, Chadima et al. 2011) both in and outside of eclipse, therefore all of these data have also been removed from our analysis. Lastly about 42% of the data (pre-1933) do not contain uncertainty estimates, therefore we have adopted a standard error of 1 km/s on these older sets. Modern data (i.e. from CfA) show significant variations in the F-star's atmosphere that far exceed the systematic uncertainties, therefore increasing the standard error on the older data sets will not result in a significantly improved fit.

4.2.3 Interferometric data

As discussed in Chapter 3, the interferometric observations of ϵ Aurigae have significantly constrained the orbital inclination, i, and position angle of the line of ascending nodes, Ω. In this work we have adopted the values of i, and Ω in Table 3.5.

4.3 Analysis

4.3.1 Astrometry

By necessity, we have used the same four reference stars as indicated in van de Kamp (1978) with the notable exception that BD +43 1161 (B1IV) was incorrectly identified in his Table 1 as BD +43 1169 (A0). Data about the reference stars are summarized in our Table 4.2. We note the values under van de Kamp were found in a hand-written note dated 1973 October 16, and may have not been used in his 1978 publication. Reference star 3, BD +43 1168 (B9Iab, Morgan et al. 1955), is labeled in SIMBAD as a "star in double system" from the Third Catalog of Visual Binaries (Finsen and Worley 1970) and was assumed to be a companion to ϵ Aur; however, it was removed from the Fourth Catalog of Visual Binaries (Worley and Heintz 1983)

due to a "lack of [orbital] signal." BD +43 1168 is a bona-fide supergiant with a radial velocity of -22.0 km/s (Münch 1957). The large difference in RV from ϵ Aur (-2.26 km/s Stefanik et al. 2010) and its removal from the Fourth Catalog should assure the reader that the two stars are not physically assoicated, and therefore its use as a reference star is valid.

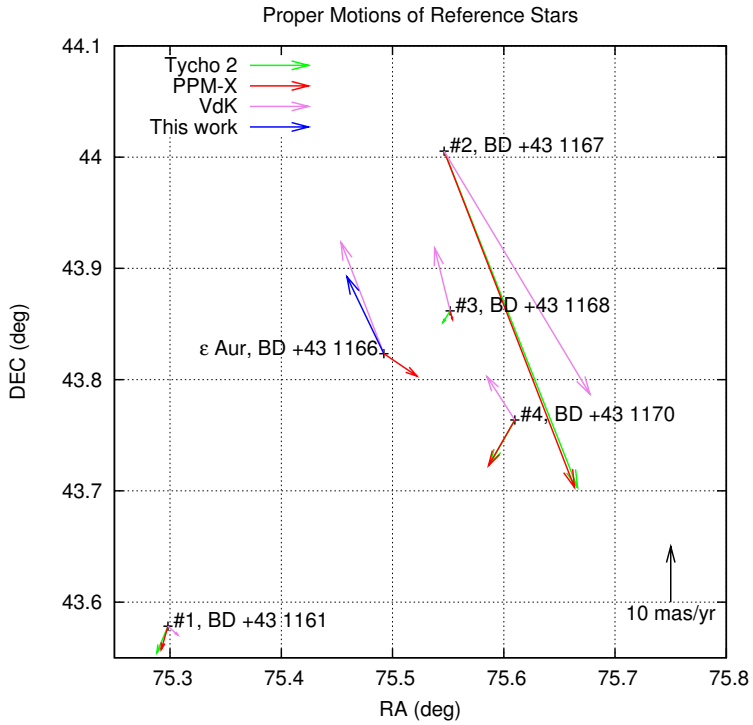

Figure 4.1: Reference frame for ϵ Aurigae in the Tycho-2, PPM-X and Van de Kamp reference frames. Proper motions have been multiplied to make them visible, a 10 *mas*/year scale bar is shown in the lower right for reference.

Table 4.2: Information on the reference and target stars. See text concerning the van de Kamp quantities.

Star #	Catalog Name	RA (J2000)	DEC (J2000)	μ_α (mas/yr)	μ_δ (mas/yr)	Spec. Type
Tycho-2						
0	2907-1275-1	75.49223333	43.82331389	...	...	F0Ia / A8Iab
1	2907-154-1	75.29810978	43.57830870	-2 ± 1.0	-4.8 ± 1.0	B1IV D
2	2907-460-1	75.54637761	44.00535634	24 ± 1.1	-60.5 ± 1.1	K0IV C
3	2907-626-1	75.55180050	43.86180924	-1.3 ± 1.5	-2.1 ± 1.7	B9Iab (star in double system)
4	2907-486-1	75.60988490	43.76375918	-4.4 ± 1.1	-7.8 ± 1.2	A0 D
5	2907-1275-1	75.49223333	43.82331389	...	...	F0Ia / A8Iab
PPM-X						
0	050158.1+434923	75.492333	43.823277	5.96 ± 0.4	-4.05 ± 0.5	
1	050111.5+433441	75.298114	43.578312	-1.21 ± 1.1	-4.2 ± 1.1	...
2	050211.1+440019	75.546378	44.005362	23.44 ± 1.2	-60.45 ± 1.1	...
3	050212.4+435142	75.551811	43.861817	0.41 ± 1.2	-1.54 ± 1.2	...
4	050226.3+434549	75.609884	43.763759	-4.75 ± 1.1	-8.23 ± 1.1	...
5	050158.1+434923	75.492333	43.823277	...	...	

continued on next page

Star #	Catalog Name	RA (J2000)	DEC (J2000)	μ_α (mas/yr)	μ_δ (mas/yr)	Spec. Type
van de Kamp (1978)						
0	BD +43 1166	...	...	...	...	F0Iap
1*	BD +43 1161	...	...	1.8	-1.6	A0
2	BD +43 1167	...	...	26.2	-43.7	K0
3	BD +43 1168	...	...	-2.8	11.3	G0
4	BD +43 1170	...	...	-5	7.8	A0
0	BD +43 1166	...	...	...	...	F0Iap

We have calibrated our reference frame to the predicted positions of two astrometric catalogs: Tycho-2 (Høg, E. et al. 2000), and the PPM Extended Catalog (PPM-X hereafter, Röser et al. 2008). Following the standard plate reduction method, we use the catalog proper motions to compute the position of the i^{th} reference star at the epoch of the j^{th} exposure and convert the resulting $(\alpha, \delta)_{i,j}$ into plate coordinates $(\xi, \eta)_{i,j}$ using the gnomonic projection defined on pg. 70 of Eichhorn (1974). As we are unsure of the true plate centers, $(\alpha_0, \delta_0)_{i,j}$, we have approximated them as the geometric average of the reference star positions. Because we have so few reference stars, we were not able to undertake a full plate solution that would compensate for optical distortions, therefore we began with a six parameter solution which accounts for plate scale ρ_x, ρ_y, rotation (θ_x, θ_y, and offsets (Δ_x, Δ_y) for each exposure:

$$\begin{aligned} \xi &= \rho_x \cos\theta_x x - \rho_y \sin\theta_x y + \Delta_x, \\ \eta &= \rho_x \sin\theta_y x + \rho_y \cos\theta_y y + \Delta_y, \end{aligned} \tag{4.3.1}$$

where x and y are the raw plate positions. The average plate scales were found to be $\rho_x = 9.429 \pm 0.002$ and $\rho_y = 9.428 \pm 0.002$ mas / SU which is slightly better than the often quoted 18.87 asec / mm scale at Sproul. Most plates have a small rotation of ~ 3 deg., but a few were inserted into the measuring machine rotated or inverted, negating one or both of the plate scales and/or yielding rotations near 90 degrees. Taking these effects into consideration, the rotations and scales were largely consistent in both directions ($(\rho_{x_j} - \rho_{y_j})/\bar{\rho} < 0.1\%$ and $(\theta_{x_j} - \theta_{y_j})//\bar{\theta} < 3.25\%$), therefore we used a four-parameter model with only one scale, ρ, and rotation θ per exposure:

$$\begin{aligned} \xi &= \rho \cos\theta x - \rho \sin\theta y + \Delta_x, \\ \eta &= \rho \sin\theta x + \rho \cos\theta y + \Delta_y. \end{aligned} \tag{4.3.2}$$

Various combinations of color, magnitude, and position dependent constants (at no time exceeding a total of four parameters per axis) were applied to account for

the aforementioned issues with Sproul data. Ultimately the four-parameter fit in Equation 4.3.2 was selected as it results in the most uniformly distributed residuals for all of the reference stars. The scales, rotations, and offset values are then applied to the data, yielding the tangential plane coordinates $(\xi_{c,j}, \eta_{c,j})$ for ϵ Aur which are used in our orbit fitting routines discussed below.

4.3.2 Improved proper motions

With the exception of BD +43 1168, the mean epoch for the reference stars from Tycho-2 and PPM-X is in the 1980s, therefore our data could significantly enhance the accuracy of the proper motions for these objects. To do so we have employed a two-stage least-squares minimization strategy in which the outer loop finds the best-fit proper motions, and the inner loop finds the best-fit scale, rotation and offset. In detail, the algorithm is initialized with the positions and proper motions from one of the aforementioned catalogs. From this, (1) the positions at the time of exposure j are computed, and (2) projected into the tangent plane as described above. Then, (3) the best-fit scale, rotations and offsets are computed in accordance with Equation 4.3.2. These values are (4) applied to yield $(\xi_{c,i,j}, \eta_{c,i,j})$ which are (5) compared against the positions $(\xi_{i,j}, \eta_{i,j})$ predicted from the current proper motion estimates. The proper motion values are modified, and the process is repeated until a minimum variance is found at which time the resulting proper motions and positions are written to file for further analysis. We will discuss the results of this effort in a future publication.

4.3.3 Modeling the data

We have modeled the orbital positions and radial velocities assuming the orbit is Keplerian using the following equations from Roy (2005):

$$\begin{aligned} X(\Theta, t_j) &= \alpha_1 \left(L_1 \cos E + \beta L_2 \sin E - e L_1\right), \\ Y(\Theta, t_j) &= \alpha_1 \left(M_1 \cos E + \beta M_2 \sin E - e M_1\right), \\ Z(\Theta, t_j) &= \alpha_1 \left(N_1 \cos E + \beta N_2 \sin E - e N_1\right), \end{aligned} \tag{4.3.3}$$

where

$$\begin{aligned} n &= 2\pi/T, \\ L_1 &= \cos\Omega \cos\omega - \sin\Omega \sin\omega \cos i, \\ M_1 &= \sin\Omega \cos\omega + \cos\Omega \sin\omega \cos i, \\ N_1 &= \sin\omega \sin i, \\ L_2 &= -\cos\Omega \sin\omega - \sin\Omega \cos\omega \cos i, \\ M_2 &= -\sin\Omega \sin\omega + \cos\Omega \cos\omega \cos i, \\ N_2 &= \cos\omega \sin i, \end{aligned} \tag{4.3.4}$$

and $\Theta = \{\Omega, \omega, i, e, T, \tau, K_1, \alpha_1\}$ have their traditional meaning.

Taking the derivative of Equation 4.3.3 with respect to time and recalling the orbit is periodic, we find the translational velocity equations:

$$\begin{aligned}
\dot{X}(\Theta, t_j) &= \frac{n\alpha}{1 - e\cos E}\left[\sqrt{1-e^2}L_2\cos(E) - L_1\sin(E)\right] \\
\dot{Y}(\Theta, t_j) &= \frac{n\alpha}{1 - e\cos E}\left[\sqrt{1-e^2}M_2\cos(E) - M_1\sin(E)\right] \\
\dot{Z}(\Theta, t_j) &= V(\Theta, t_j) \\
&= \frac{na}{1 - e\cos E}\left[\sqrt{1-e^2}N_2\cos E - N_1\sin E\right], \\
&= \frac{K_1}{1 - e\cos E}\left[(1-e^2)\cos\omega\cos E - \sqrt{1-e^2}\sin\omega\sin E\right].
\end{aligned} \tag{4.3.5}$$

The iterative nature of our model fitting process requires frequent evaluation of the above equations, therefore we have used the Eccentric anomaly, E, in our RV equations rather than the true anomaly, ν, to reduce the over all computational cost.

Note that Equations 4.3.5 can be used to determine the total semi-major $\alpha = \alpha_1 + \alpha_2$ from the translational motion $(\dot{X}, \dot{Y})$ if all of the other orbital parameters $(\Omega, \omega, i, e, T, \tau)$ are determined to sufficient accuracy. The translational motion can be revealed by two mechanisms: either direct observation (i.e. inteferometry) or by a model for the disk combined with a photometric light curve. Once α is known the mass ratio, q, may be computed as discussed in the introduction and the component masses derived via. the mass function, $f(M)$.

Using the computed tangential plane positions for ϵ Aur, $(\xi_{c,j}, \eta_{c,j})$, and the k^{th} RV data point, we fit the positions by finding parameters that yield the maximum likelihood of these expressions:

$$\begin{aligned}
\xi_{c,j} &= X'(\Theta, t_j) = X_0 + \mu_\alpha t_j + \pi P_{\alpha,j} + X(\Theta, t_j), \\
\eta_{c,j} &= Y'(\Theta, t_j) = Y_0 + \mu_\delta t_j + \pi P_{\delta,j} + Y(\Theta, t_j), \\
v_k &= V'(\Theta, t_k) = \gamma + V(\Theta, t_k),
\end{aligned} \tag{4.3.6}$$

wherein (X', Y', V') indicate inclusion of systematic motion, (X_0, Y_0) are zero points, (μ_α, μ_δ) are proper motions, π is the parallax, γ is the system radial velocity and (P_α, P_δ) are parallax factors computed using the *epv00* routine from the Standards of Fundamental Astronomy C-library (IUA SOFA Board 2010).

4.4 Bayesian evaluation

4.4.1 Likelihood functions

As discussed in Gregory (2007), the uncertainties in RV measurements follow a normal distribution. Therefore the likelihood function for RV data can be written as:

$$L_{V'}(\Theta) = \prod_k \frac{1}{\sqrt{2\pi(\sigma_{v_k}^2 + s^2)}} \exp\left(\frac{(V'(\Theta; t_k) - v_k)^2}{2(\sigma_{v_k}^2 + s^2)}\right) \tag{4.4.1}$$

where our model, V', is the RV equation defined above, D_i and σ_i are the i^{th} data and uncertainty respectively, and s is a Gaussian noise component which we ascribed to intrinsic stellar variability.

Similarly, if the uncertainties on the astrometric plates follow a normal distribution, then the bivariate normal distribution can be used as the likelihood function. If the uncertainties are uncorrelated, then the likelihood function simplifies to:

$$L_{X'Y'}(\Theta) = \prod_j \frac{1}{2\pi\sigma^2_{\xi_{c,j}}\sigma^2_{\eta_{c,j}}} \exp\left(-\frac{1}{2}\left[\frac{(X'(\Theta;t_j)-\xi_{c,j})^2}{\sigma^2_{\xi_{c,j}}} + \frac{(Y'(\Theta;t_j)-\eta_{c,j})^2}{\sigma^2_{\eta_{c,j}}}\right]\right), \tag{4.4.2}$$

In this work we take advantage of the conditional probability framework afforded by Bayesian statistics. This permits the different, yet complementary information from the astrometric and radial velocity data sets to be combined in a consistent manner. The conditional probability is formed by the product of the individual probabilities:

$$P(\Theta|D,H) = \frac{P(v|\Theta,V')}{P(v|V')}\frac{P(\xi_c,\eta_c|\Theta,X',Y')}{P(\xi_c,\eta_c|X',Y')}P(\Theta|V',X',Y'), \tag{4.4.3}$$

4.4.2 Choice of priors

Here we have elected to used three primary priors. The Uniform prior has equal probability over the parameter range. The Jeffreys prior has equal probability over the parameter range in logarithmic terms. The modified Jeffreys prior has similar behavior to the Jeffreys prior, but is modified to account for the functional form of the orbital semi-amplitude, K. Table 4.3 lists the priors used for our orbit fitting routines.

Table 4.3: Priors used in astrometric and RV modeling

Parameter	Prior	Mathematical Form	Lower Bound	Upper Bound
ω (deg)	Uniform	$\frac{1}{\omega_{min}-\omega_{max}}$	0	2 π
e	Uniform	$\frac{1}{e_{min}-e_{max}}$	0	1
τ (d)	Jeffreys	$\frac{1}{\tau \ln(\tau_{max}/\tau_{min})}$	2413932	2454878
T (d)	Jeffreys	$\frac{1}{T \ln(T_{max}/T_{min})}$	8000	12000
K_1 (km/s)	Mod. Jeffreys	$\frac{(K-K_0)^{-1}}{\ln(1+(K_{max}/K_0)(T_{min}/T)^{1/3}(1/\sqrt{1-e^2})}$	5	20
γ (km/s)	Uniform	$\frac{1}{\gamma_{min}-\gamma_{max}}$	-10	10
Ω (deg)	Uniform	$\frac{1}{\Omega_{min}-\Omega_{max}}$	116	118.5
i (deg)	Uniform	$\frac{1}{i_{min}-i_{max}}$	88	90
s_1 (km/s)	Jeffreys	$\frac{1}{s \ln(s_{max}/s_{min})}$	1	$K_{\max}$
α_1 (mas)	Uniform	$\frac{1}{\alpha_{min}-\alpha_{max}}$	1	70
x_0 (asec)	Uniform	$\frac{1}{x_{0_{min}}-x_{0_{max}}}$	-25	-23
y_0 (asec)	Uniform	$\frac{1}{y_{0_{min}}-y_{0_{max}}}$	74	76
μ_α (mas/yr)	Uniform	$\frac{1}{\mu_{\alpha_{min}}-\mu_{\alpha_{max}}}$	-36	36
μ_δ (mas/yr)	Uniform	$\frac{1}{\mu_{\delta_{min}}-\mu_{\delta_{max}}}$	-36	36
π (mas)	Uniform	$\frac{1}{\pi_{min}-\pi_{max}}$	-10	10

4.5 Results

Using these constraints we have conducted a Bayesian analysis of the orbital elements using both astrometric and radial velocity data. First we modeled the RV data under the assumption of purely Keplerian orbital motion yielding an $\log(Z) = -18192$ (log of Bayesian evidence factor, Z). Our second model extended this assumption by adding a Gaussian noise source, s, to represent the supposed variability in the atmosphere of the F-star. This solution yields a $\log(Z) = -3626$. The Bayes factor of 5.01 provides significant support favoring the inclusion of s in our models.

The results of the RV fitting routines are summarized in Table 4.4. In general our RV solutions are in excellent agreement with the solutions from Stefanik et al. (2010) and Chadima et al. (2010). We note that our time of periastron, τ is $150-270$ days earlier than the aforementioned publications, but in agreement with the purely Keplerian solution from Stefanik et al.. We suspect applying constraints from the photometry will resolve these discrepancies. Likewise, our period, T is also much less constrained, but still consistent with prior works.

Table 4.4: Current and prior spectroscopic orbital solutions for ϵ Aurigae. The last four sources are Wright (1970), Morris (1962), Kuiper et al. (1937), and Ludendorff (1924), respectively. * indicates the parameter was assumed from some outside source.

	This Work		Chadima et al. (2010)		Stefanik et al. (2010)					
	Keplerian	Kep. w/ Noise	PHOEBE	FOTEL	Keplerian	Combined	Wright	Morris	Kuiper	Ludendorff
ω (deg)	38.3 ± 0.3	36.1 ± 0.3	41.2 ± 3.1	43.3 ± 4.0	29.8 ± 3.1	39.2 ± 3.4	29.8 ± 3.1	347.8 ± 15.8	350	319.7
e	0.264 ± 0.003	0.276 ± 0.015	0.256 ± 0.012	0.249 ± 0.015	0.290 ± 0.016	0.227 ± 0.011	0.200 ± 0.034	0.172 ± 0.033	0.33	0.35
τ (HJD - 2.4E6)	44502 ± 15	44464 ± 77	44706 ± 24	44732 ± 98	44307 ± 77	44619 ± 80	43228 ± 279	43221 ± 0.42	43607	41492
T (day)	9869.09 ± 2.97	9884.06 ± 15.05	9890.26 ± 0.62	9890.98 ± 0.50	9882 ± 17	9896.0 ± 1.6	9882 ± 17	9890 *	9890 *	9090
K_1 (km/s)	14.29 ± 0.04	14.10 ± 0.22	14.40 ± 0.38	14.3 ±0.25	13.84 ± 0.23	14.43 ±0.27	15 ± 0.58	14.71 ± 0.53	15.7	14.8
γ (km/s)	-2.60 ± 0.03	-2.33 ± 0.14	...	...	-2.41 ± 0.15	-2.26 ± 0.15	-2.41 ± 0.15	-1.29 ± 0.39	-2.5	-1.8
s (km/s)	...	4.64 ± 0.01	4 - 6	4 - 6	4.63	4.59	...	...	...	...
$a_1 \sin i$ (1E6 km)	1870 ± 6	1842 ± 30	1897 ± 50	1883 ± 33	1876 ± 30	1835 ± 29	2000	1970	2014	1887
$f(M)$ $M_\odot$	2.68 ± 0.03	2.55 ± 0.12	3.05 ± 0.24	3.00 ± 0.16	2.69 ± 0.13	2.51 ± 0.12	2.69 ± 0.13	3.12	3.34	2.7
log(Z)	-18193	-3626	...	...	...	...	...	...	...	...

The astrometric data was reduced using the four parameter plate constant method described above with respect to the Tycho-2 and PPM-X reference frames, using both the catalog and refit proper motions. The residuals from the Tycho-2 catalog and refit proper motions appear more uniformly distributed and summarized here in Figures 4.2 and 4.3. Similar plots for the PPM-X catalog are found in Figures 4.4 and 4.5. The computed positions for ϵ Aur were equally weighted and given 40 mas uncertainties in accordance with the average scatter of 1-2 μm in the raw plate measurements. An initial, unconstrained fit using our routines yielded $i \sim 70$, Ω 90, and $\alpha_1 \sim 36$ *mas*. With these values of i and Ω the eclipse, as observed, cannot occur, therefore the interferometric constraints were applied. Additional constraints of $20 < \omega < 50$ and $0.2 < e < 0.35$ bounds were applied to enforce consistency with the radial velocity data.

These solutions, summarized in Table 4.5, yield semi-major axes that are smaller than and inconsistent with prior Sproul solutions at the 2σ-level. It is interesting to note that these revised solutions are within bounds of the Yerkes solution (Strand 1959). Take note that the time of periastron, τ, and orbital period, T, are very poorly constrained by the astrometric data alone. We take this to indicate the orbital signal we are attempting to find is near the limit of what can be done with the available data.

Table 4.5: Current and prior astrometric orbital solutions for ϵ Aurigae. * denotes the parameter was assumed and ‡ indicates the value is implied by references in the original text. The last three astrometric studies are Heintz and Cantor (1994), van de Kamp (1978), and Strand (1959) respectively.

	This Work (Sproul Data)				Sproul		Yerkes
	Tycho-2 Normal	Tycho-2 Refit	PPMX	PPMX Refit	H&C	VdK	Strand
ω (deg)	33.0 ± 2.6	36.4 ± 5.0	36.4 ± 5.0	36.4 ± 5.1	0 *	29.8 ‡	350 ‡
e	0.331 ± 0.018	0.324 ± 0.024	0.325 ± 0.023	0.324 ± 0.024	0.07 *	0.20 *	0.33 *
τ (HJD - 2.4E6)	42918 ± 65	43218 ± 196	43218 ± 196	43214 ± 197	43263	43244	...
T (day)	9916.24 ± 25.72	9915.53 ± 26.04	9916.21 ± 25.83	9915.13 ± 26.08	9891 *	9891 *	9891 *
Ω (deg)	118.00 ± 0.45	117.94 ± 0.49	117.95 ± 0.49	117.96 ± 0.49	264	92 ± 3	...
i (deg)	93.93 ± 1.05	94.09 ± 0.88	94.09 ± 0.90	94.08 ± 0.90	87	89 ± 3	72
α_1 (mas)	16.7 ± 1.5	17.0 ± 1.5	16.9 ± 1.5	16.9 ± 1.5	22.4 ± 1.8	22.7 ± 1	14 ± 4
X_0 (mas)	-24.1 ± 0.1	-24.0 ± 0.1	-24.0 ± 0.1	-24.0 ± 0.1	...	...	...
Y_0 (mas)	75.2 ± 0.1	74.8 ± 0.1	74.9 ± 0.1	74.8 ± 0.1	...	...	...
μ_x (mas/yr)	-5.99 ± 0.10	-5.92 ± 0.09	-5.99 ± 0.09	-5.85 ± 0.09	...	7.7 ± 0.1	...
μ_y (mas/yr)	13.27 ± 0.11	13.44 ± 0.11	13.27 ± 0.11	13.37 ± 0.11	...	20.2 ± 0.1	...
$\pi_{\rm rel}$ (mas)	6.21 ± 1.32	6.21 ± 1.33	6.25 ± 1.34	6.20 ± 1.32	3 ± 2	1 ± 1	6 ± 3
log(Z)	-5164	-5162	-5163	-5163	...	...	...

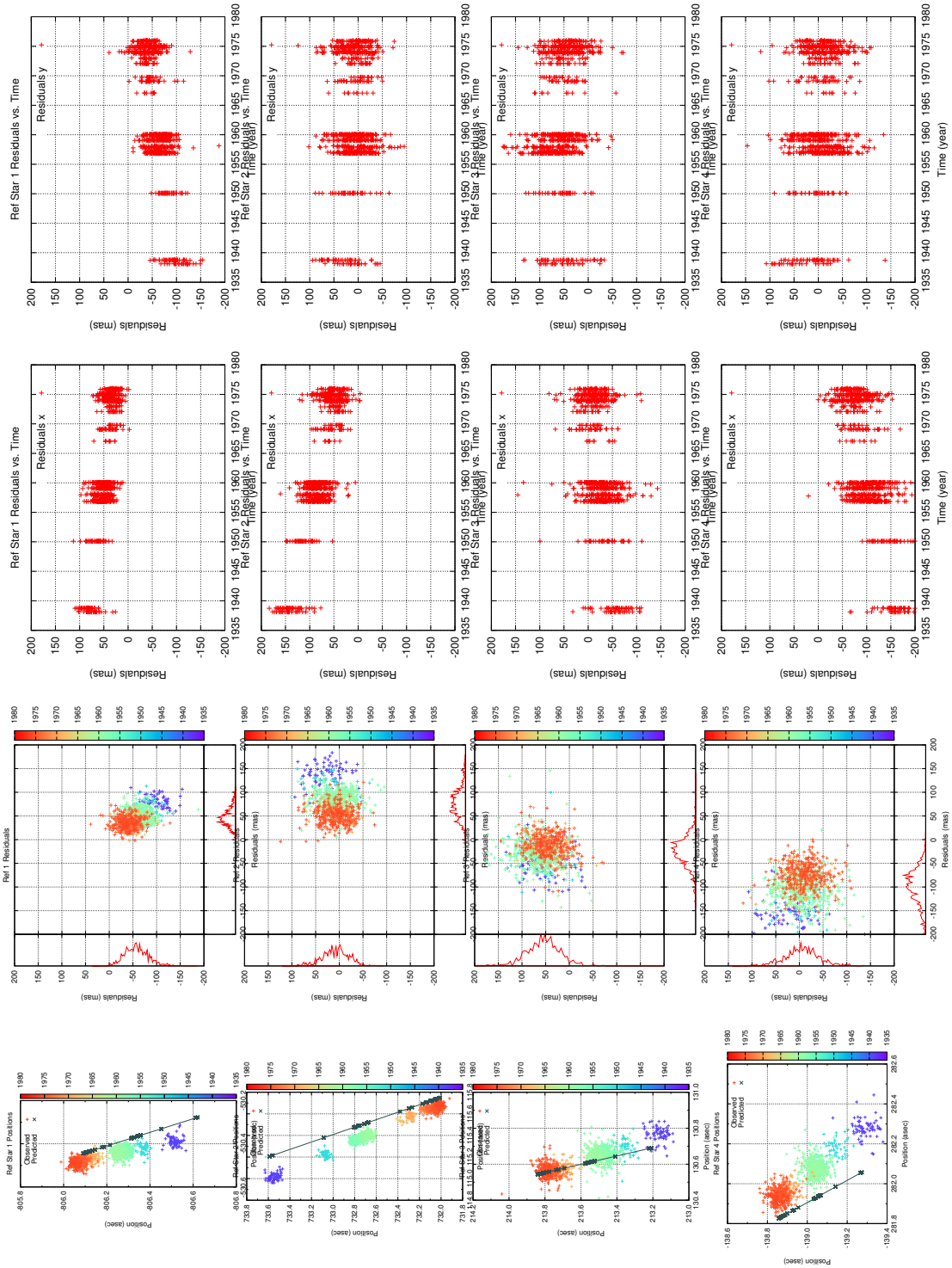

Figure 4.2: Fits and residuals for the reference stars in the Tycho2 reference frame.

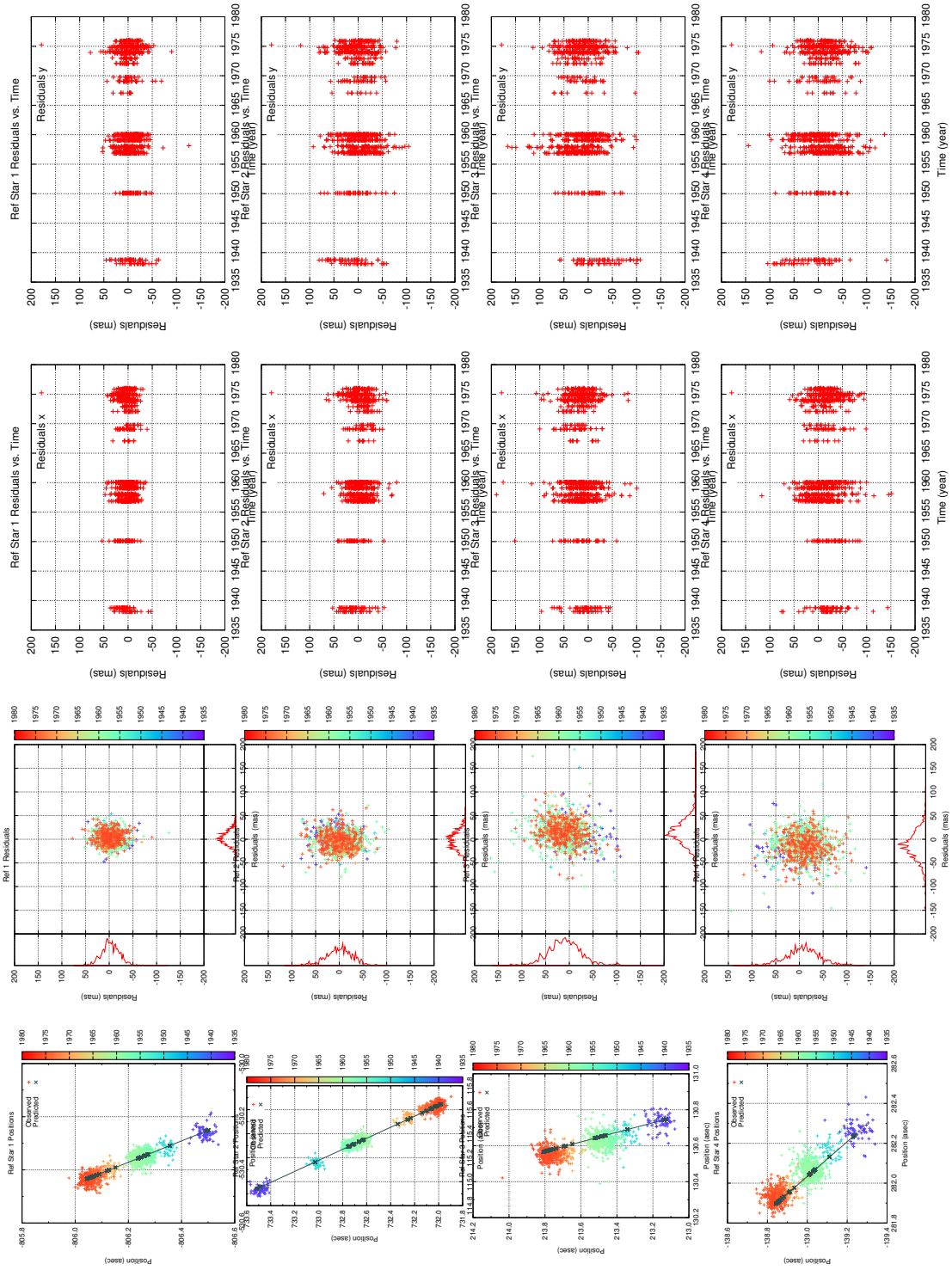

Figure 4.3: Fits and residuals for the reference stars in the refit Tycho2 reference frame.

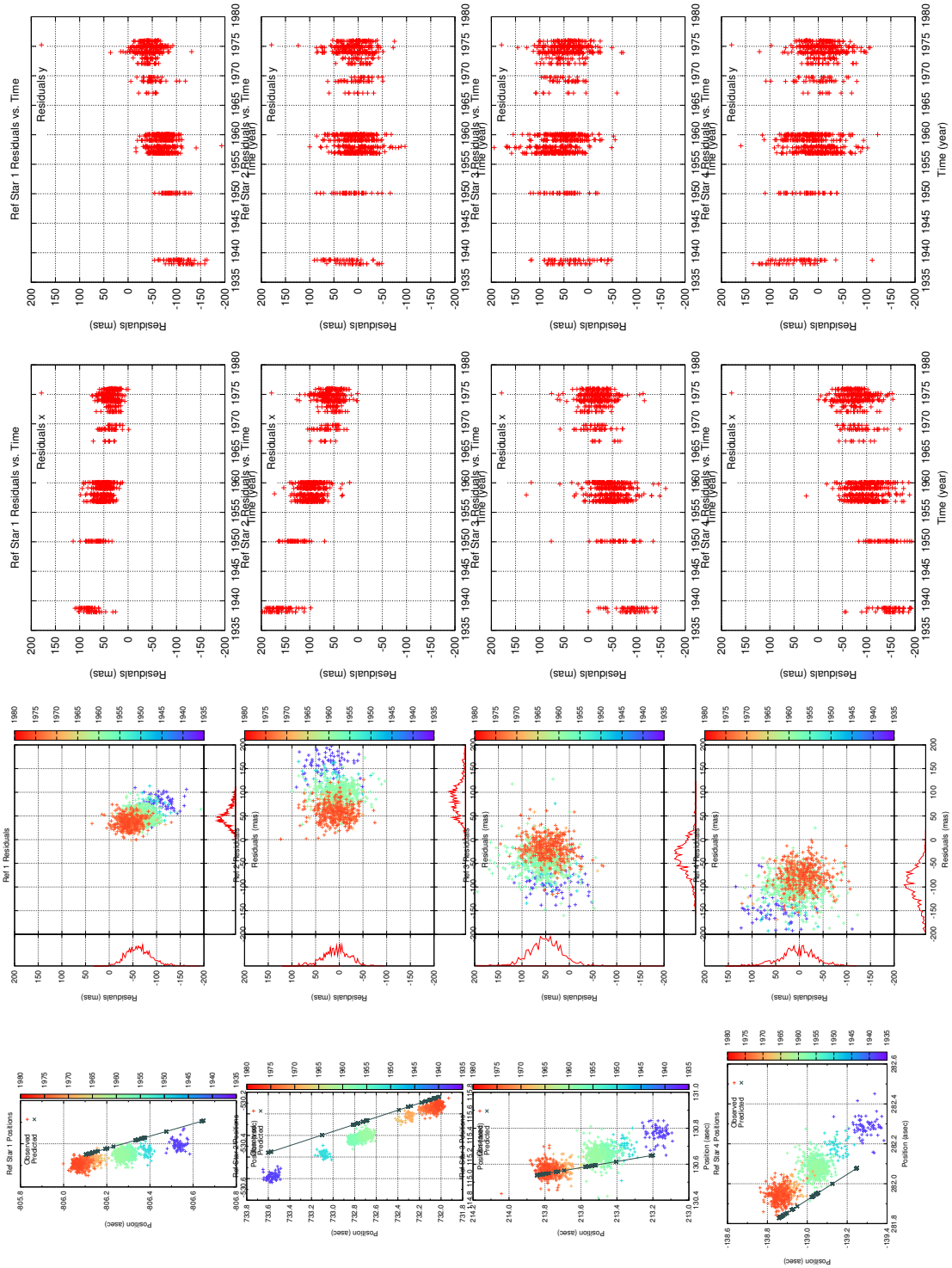

Figure 4.4: Fits and residuals for the reference stars in the PPM-X reference frame.

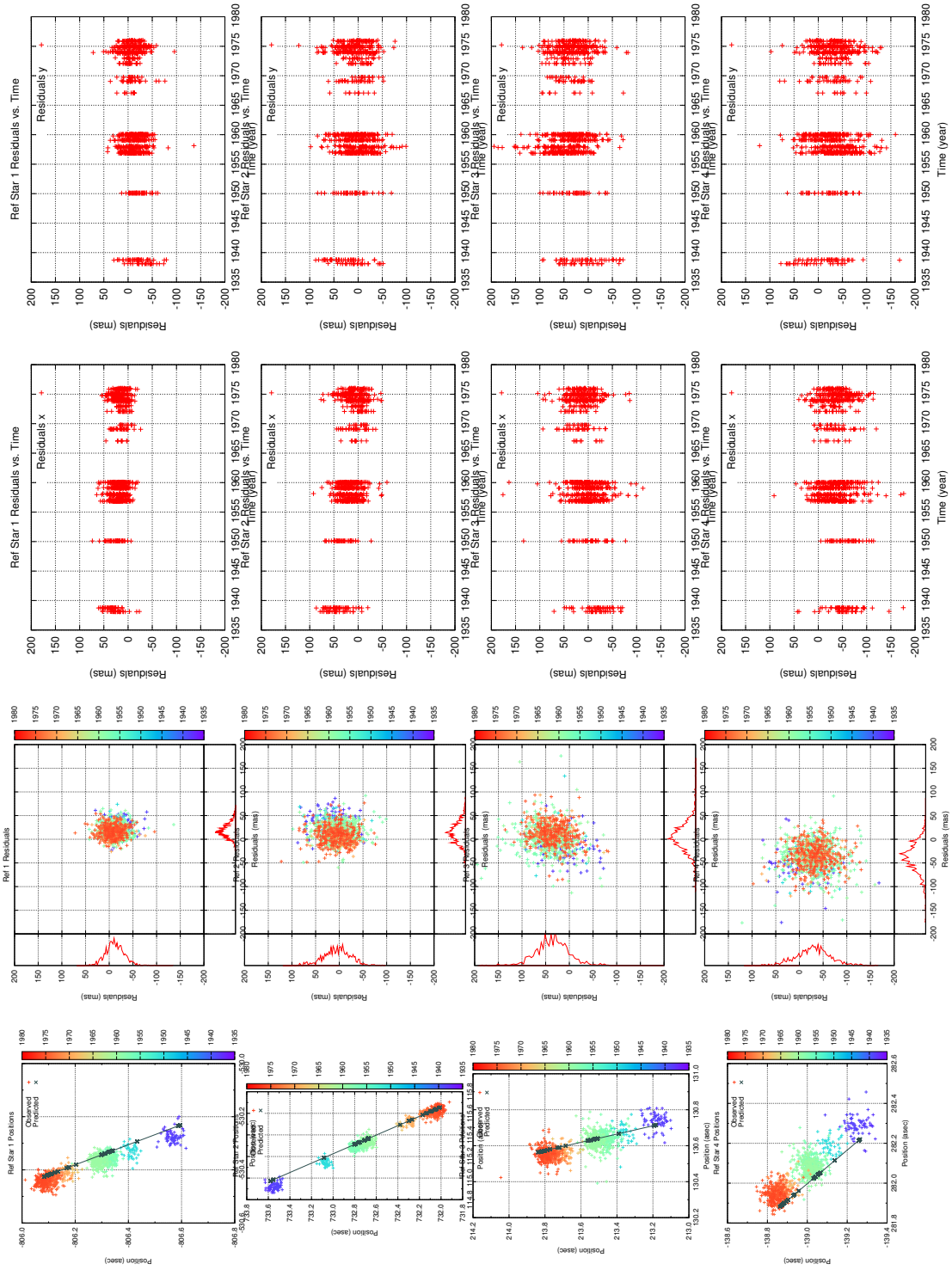

Figure 4.5: Fits and residuals for the reference stars in the refit PPM-X reference frame.

Lastly a joint astrometric and RV solution was found. The angular parameters i and Ω were again constrained to agree with the interferometric values and the RV noise parameter, s, was included. The resulting 12 orbital, one noise, and three derived parameters are indicated in Table 4.6. The best-fit orbital parameters and their corresponding orbit are over-plotted on the raw data in Figures 4.7 and 4.8. Of most importance for this work are the semi-major axes in angular and linear units. From the combined astrometry and RV fit, we obtain $\alpha_1 = 15 \pm 2$ mas and $a \sin i = 1953 \pm 28$ 1E6 km with a $\log Z \sim -9300$. By using the values from Tables 4.4, 4.5, we may form a disjoint solution which yields a distance of $d = 737 \pm 67$ pc with a $\log Z \sim -8800$. The evidence values would suggest the disjoint solution, being more positive, is more probable; however, the Bayes factor implies neither solution should be favored over the other. Notice the power of Bayesian statistics permits us to make this comparison, whereas within the frequentest framework there is no objective method for comparing the two fits, therefore the disjoint solution would likely be favored.

Inspection of the posterior probability distribution histograms in Figure 4.6 reveals that most of the orbital parameters follow near-normal distributions, implying that the model used is appropriate and the statistics on the values in Table 4.6 are well sampled. The exceptions to this are Ω and i which were been constrained by interferometric model fitting and permitted to freely float within 1σ limits of their nominal values. The dual peaks in τ, X_0, Y_0 are caused by the periodicity of the orbit.

Our values of ω and e are within 1σ and 1.5σ of the spectroscopic values. The orbital semi-amplitude, K_1 is 0.7 km/s higher than any previous estimate, pushing a 2σ limit. Like the RV-only solution, our estimate of τ is 300 days too early when compared with prior work. Likewise, T has greater uncertainties. We suspect these differences are caused by the quasi-periodic variations and large gaps in the RV curve around eclipses. Again applying photometric constraints would improve these values.

Inspection of the $\log Z$ Bayesian evidence values between Tables 4.4, 4.5, and 4.6 reveals that the evidence factor for the joint fit is lower than the individual fits by $\Delta \log Z = 200$. This would imply either (1) the model for the combined astrometry and RV data is not appropriate which we find implausible, or (2) or that one of the data sets is inconsistent or somehow less constraining than the other. We would argue that the astrometric data is of significantly lower quality when compared with the RV data. Without a considerable investment of time digitizing the plates and obtaining new observations, this situation is unlikely to change.

Figure 4.6: Posterior Probability distributions for the orbital parameters showing that all orbital parameters, except Ω and i are well determined by our modeling.

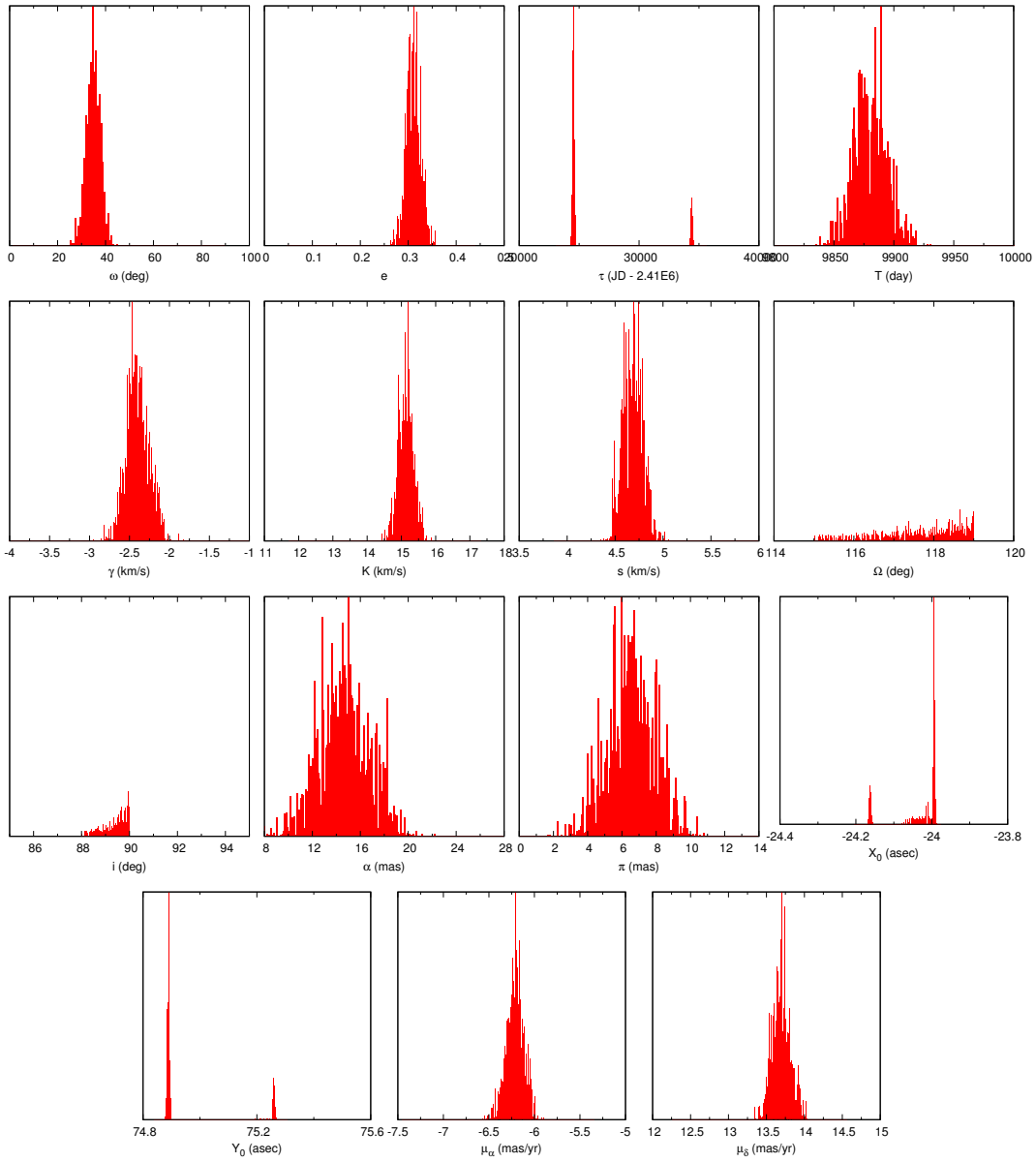

Figure 4.7: The raw astrometric data with the best-fit combined Tycho-2 refit solution overplotted. A standard error of 40 mas (not plotted) was adopted for each astrometric data point.

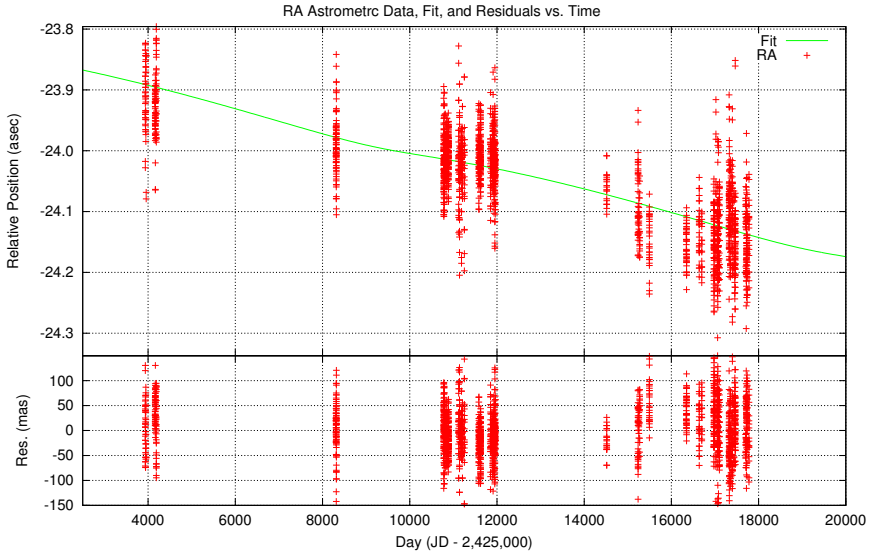

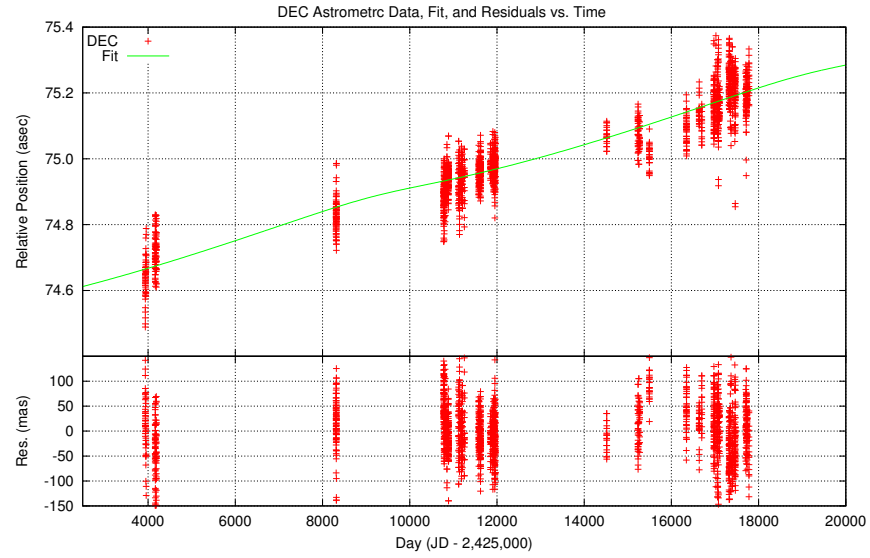

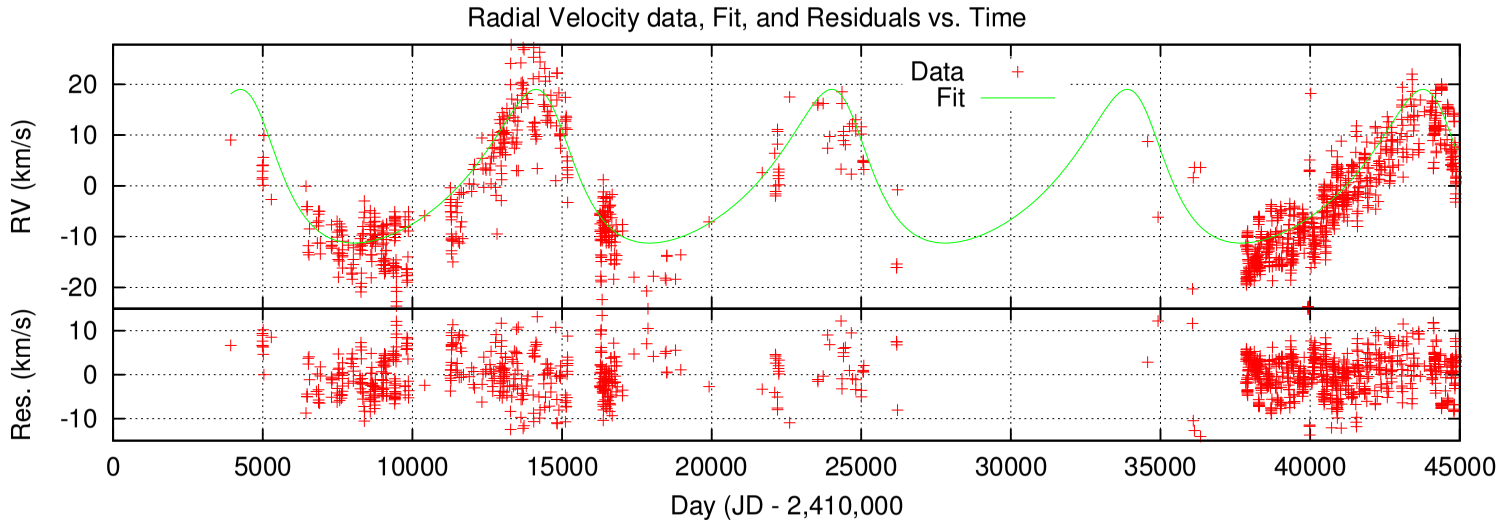

Figure 4.8: Results of the joint Astrometric and Radial Velocity fit for the Tycho2-refit data set. Uncertainties on the RV data are typically 1 km/s or less which is about the same size as the plotting symbol used. The residuals are are dominated by the ~ 4.6 km/s intrinsic variability of the F-star. See Section 4.6 concerning disagreement between $\pi_{\rm rel}$ and $d_{\rm dyn}$.

Table 4.6: New orbital solutions for ϵ Aurigae using both astrometric and RV data. Compare with Tables 4.4 and 4.5.

	Tycho-2 Normal	Tycho-2 Refit	PPMX	PPMX Refit
ω (deg)	34.7 ± 2.7	34.6 ± 2.8	34.6 ± 2.9	34.9 ± 3.0
e	0.309 ± 0.013	0.310 ± 0.014	0.310 ± 0.015	0.311 ± 0.015
τ (HJD - 2.4E6)	44383 ± 66	44377 ± 68	44379 ± 68	44385 ± 72
T (day)	9879.22 ± 14.36	9878.12 ± 13.03	9879.95 ± 13.75	9880.68 ± 13.88
K_1 (km/s)	15.12 ± 0.20	15.14 ± 0.21	15.13 ± 0.23	15.13 ± 0.21
γ (km/s)	-2.39 ± 0.14	-2.39 ± 0.14	-2.40 ± 0.15	-2.40 ± 0.14
Ω (deg)	117.73 ± 1.01	117.61 ± 1.05	117.69 ± 1.03	117.69 ± 1.02
i (deg)	89.52 ± 0.44	89.55 ± 0.40	89.51 ± 0.43	89.48 ± 0.46
α_1 (mas)	14.6 ± 1.9	14.5 ± 2.1	14.6 ± 2.0	14.7 ± 2.1
s (km/s)	4.68 ± 0.10	4.68 ± 0.10	4.68 ± 0.10	4.69 ± 0.10
X_0 (mas)	-24.2 ± 0.1	-24.0 ± 0.1	-24.2 ± 0.1	-24.0 ± 0.1
Y_0 (mas)	75.3 ± 0.1	74.9 ± 0.1	75.3 ± 0.1	74.9 ± 0.1
μ_x (mas/yr)	-6.15 ± 0.09	-6.21 ± 0.10	-6.08 ± 0.09	-6.22 ± 0.09
μ_y (mas/yr)	13.85 ± 0.10	13.67 ± 0.10	13.78 ± 0.10	13.69 ± 0.11
$\pi_{\rm rel}$ (mas)	6.49 ± 1.37	6.40 ± 1.23	6.39 ± 1.28	6.58 ± 1.37
$a_1 \sin i$ (1E6 km)	1953 ± 28	1955 ± 29	1954 ± 31	1954 ± 29
$f(M)$ $M_\odot$	3.04 ± 0.13	3.05 ± 0.14	3.05 ± 0.14	3.05 ± 0.13
$d_{\rm dyn}$ (pc)	896 ± 13	899 ± 13	894 ± 14	891 ± 13
$\log(Z)$	-9030	-9029	-9031	-9029

4.6 Discussion

For those not experienced with astrometry, the disagreement between $\pi_{\rm rel}$ and $d_{\rm dyn}$ in Table 4.6 may seem startling; however, these are fundamentally different quantities. The relative parallax, $\pi_{\rm rel}$, is a measurement of the parallax with respect to the parallax of the reference frame. As no detailed study of our reference frame has been conducted, we know very little about the reference stars. We believe reference star #2 (BD +43 1167) may have a parallax approaching 9 *mas* and #4 (BD +43 1170) may be at $3-6$ *mas*. Reference star #1 (BD + 43 1161) and #2 (BD +43 1168) likely have $\pi < 1$ *mas*. Because we do not correct for the parallax of the reference frame, the parallax solution for ϵ Aurigae is being pulled around by foreground reference stars.

Abruptly switching topics, the resulting semi-major axis from the combined solution is in excellent agreement with the published values from Strand (1959). This is not too surprising. The Yerkes observatory has a plate scale of nearly twice that of Sproul, therefore if α_1 had indeed been 21 *mas*, this should have been detected by Strand, even if the orbital parameters were incorrect. What is surprising is that in van de Kamp (1978), the author mentions a provisional value of $\alpha_1 = 17.6 \pm 1.3$ *mas* published in his 1974 conference poster. This value is in great agreement with our results and with Strand. We did not find any notes in the Sproul archives that indicate what may have been changed between the 1974 and 1978 publications.

We suspect our uncertainties could be significantly diminished if the astrometric plates on ϵ Aurigae at both Sproul and Yerkes could be digitized. We have been able to identify at least 24 potential reference stars from a print of a plate. These stars are sufficiently faint ($V \geq 9$) that ESA's GAIA satellite (planned launch date of August 2013) should be able to provide significantly improved positions and proper motions. The greater number of reference stars combined with 57 years (2.1 orbits) years of ground-based astrometry would vastly enhance the orbital solution described herein.

The $\pi = 1.53 \pm 1.29$ result from HIPPARCOS is particularly interesting considering the mean accuracy of the instrument has been shown to be ~ 0.2 *mas*. The orbital solution used in van Leeuwen (2007) is that of Heintz and Cantor (1994) which incorrectly assumed e and ω were zero which may have contributed to the large error. However, including more realistic orbital parameters or no orbit and just spurious acceleration terms does not significantly improve the fit (van Leeuwen 2010 priv. comm.). If the results in this work are indeed true, then the F-star would occupy a large fraction of Earth's orbit. Therefore the baseline of the HIPPARCOS measurements would be inadequate to accurately determine the parallax of the system.

It is instructive to check the validity of our solutions against theoretical models and observational constraints. First, from Chapter 3, the F-star has a limb-darkened angular diameter of ~ 2.3 *mas*. At a distance of 890 ± 13 pc, the star would have a radius of 223 ± 9 $R_{\odot}$. Although this is slightly larger than the the prediction of 200 $R_{\odot}$ derived in Pasinetti Fracassini et al. (2001) (by a direct applying eclipsing binary star theory), the radius appears too big to agree with standard evolutionary models. Indeed, a typical F-type supergiant of 7000-8000 K has a radius of $\sim 100 R_{\odot}$ (Cox 2000) making our diameter more than twice accepted values. If we assume the F-star is a supergiant and must confirm to this radius, the system would need to be located at ~ 400 pc. At this distance the system should have a parallax of 2.5 *mas* which is near the upper limit of the large HIPPARCOS uncertainties. Given the performance of HIPPARCOS, we argue this would probably have been detected, even accounting for photospheric variations.

Chapter 5

Conclusion and future prospects

In this chapter I summarize the key results from prior chapters and discuss how they determine the evolutionary state of the system. I present an updated set of system parameters and the first observationally determined mass ratio for the binary. I conclude by discussing remaining topics of research which I think should be explored in greater detail.

5.1 Results

The 27 years worth of inter-eclipse data from Lou Boyd and Jeffrey Hopkins portrayed an interesting picture of the system. The F-star appeared to exhibit one or more interfering modes that manifested as a coherent variational pattern every 3282 days. This was almost exactly 1/3 of the orbital period, suggesting the driving mechanism may be related to orbital motion. We found stable periods in two "tracks" that evolved at $\Delta P = -1.6$ day/year for the longer period case, whereas the shorter periods changed at a slightly slower rate of $\Delta P = -1.2$ day/year. The

trend towards shorter periods (higher frequencies) suggested that the F-star may be contracting. We have provided a list of dates and predicted periods that would manifest, if this trend continues, in Table 2.6.

At the time of this writing, no definitive asteroseismic theory for evolved, luminous objects existed. There we compared periods observed in ϵ Aurigae with photometric behavior seen in known supergiant and post-AGB stars. Post-AGBs have a clear correlation between effective temperature and period (Hrivnak et al. 2010) which, when interpolated to 7500 K, resulted in periods that are 2-3 times shorter than what we observe in ϵ Aurigae. The periods in supergiants with similar spectral type and luminosity to the F-star have periods in almost perfect agreement with what we have derived here (van Leeuwen et al. 1998). This suggests, but does not prove, that the F-star in ϵ Aurigae is a "normal" supergiant.

Our interferometric data provide model-independent images that confirmed the eclipse is caused by an opaque disk of material passing in front of the F-star. Figures 3.9 - 3.13 show that the disk is viewed almost entirely edge-on. The mid-eclipse image (2010-08) showed no evidence for the central clearing which has been used to explain the mid-eclipse brightening during prior eclipses. Inspection of the 1983 eclipse data revealed the mid-eclipse brightening feature is composed of three data points taken at very high airmasses. We have suggested these three points should be regarded as highly suspicious. If discarded, the eclipse appeared qualitatively similar to the 2009-2011 eclipse in Figure 2.2 in which no mid-eclipse brightening occurred. If it is later found that any additional flux existed in the system, we suggest scattering above and below the plane of the disk is a better explanation (see Budaj 2011) than a central clearing.

The interferometric images did not show a series of inclined concentric semi-transparent rings as suggested by Ferluga (1990). This is not to say the disk is not composed of rings of material (indeed, spectroscopic data from the current eclipse

argues for ring structures), but instead that the rings in the disk were not responsible for photometric variations seen during totality. We suggested the low-amplitude variations seen during the eclipse were instead a manifestation of the out-of-eclipse variations that happened to manifest in stable pulsations as we predicted in Chapter 2.

Our interferometric models revealed hitherto undiscussed features and effects. Foremost the data from PTI implied that the F-star was shrinking at a rate of -0.03 ± 0.01 *mas*/yr, or about 1% per year. This was corroborated, albeit poorly, by the CHARA data which attest there was a -0.03 ± 0.02 *mas*/yr radial change. The CHARA data were of much higher quality than the PTI data, and the large uncertainty was likely due to inadequacies in our model. These measurements were in agreement with claims of a 0.6% / year decrease in radius by Saitō and Kitamura (1986).

The disk, on the other hand, did not entirely conform to any of our disk models, even "Disk B" which has an outer rim that decreased in height following a scale-height distribution. The disk appeared to be significantly flared in 2010-02. This observation is corroborated with a minimum in flux (in all filters) at this time. This could represent a pile up of material from a sublimation zone on the F-star facing side of the disk (Takeuti 1986; 2011). After mid-eclipse, the interferometric data implied the disk was decreasing in thickness, which should manifest as in increase in H-band flux. Indeed, observed H-band photometry showed a slight increase in flux during this time period. Conversely, an inspection of the in-eclipse photometry (see Figure 2.2) shows the system is dimming in U-band.

To explain this disagreement, we suggested recently sublimated material in the form of small particles and/or molecules was causing additional absorption at shorter wavelengths along the line of sight. The appearance of CO shortly after mid-eclipse (Stencel et al. 2011) and increased neutral potassium (Leadbeater 2012 in prep) absorption between the first and second-half of the eclipse supports this interpretation.

In Table 5.1 we displayed the new orbital solution for ϵ Aurigae along with the derived distance, mass ratio, and component masses for the F-star (M_1) and secondary (disk + star, M_2) for both the joint and disjoint solutions discussed in Chapter 4. Here we see the F-star has $M > 6-10\ M_{\odot}$, which implied it cannot be a low-mass, post-AGB star. We caution the reader that this conclusion is dependent primarily on the calculated mass ratio, $q = \alpha/\alpha_1 - 1$. Although our work was in excellent agreement with prior literature discussing α_1, no prior work *could* have derived α without significant assumptions about the eclipsing object. We highly suggest the follow up studies we outline in the following section be pursued to confirm our conclusions.

Table 5.1: System and Orbital Parameters. * is computed by summing the disjoint $\log Z$ values.

	Solution Method	
	Joint	Disjoint
ω (deg)	34.6 ± 2.8	36.1 ± 0.3
e	0.310 ± 0.014	0.276 ± 0.015
τ (HJD - 2.4E6)	44377 ± 68	44464 ± 77
T (day)	9878.12 ± 13.03	9884.06 ± 15.05
K_1 (km/s)	15.14 ± 0.21	14.10 ± 0.22
γ (km/s)	-2.39 ± 0.14	-2.33 ± 0.14
Ω (deg)	117.61 ± 1.05	116.91 ± 0.02
i (deg)	89.55 ± 0.40	89.55 ± 0.40
α (mas)	36.277 ± 0.025	36.277 ± 0.025
α_1 (mas)	14.5 ± 2.1	17.0 ± 1.5
s (km/s)	4.68 ± 0.10	4.64 ± 0.01
μ_x (mas/yr)	-6.21 ± 0.10	-5.92 ± 0.09
μ_y (mas/yr)	13.67 ± 0.10	13.44 ± 0.11
$\pi_{\rm rel}$ (mas)	6.40 ± 1.23	6.21 ± 1.33
$a_1 \sin i$ (1E6 km)	1955 ± 29	1842 ± 30
$f(M)$ $M_\odot$	3.05 ± 0.14	2.55 ± 0.12
$d_{\rm dyn}$ (pc)	899 ± 13	737 ± 67
q	1.50 ± 0.36	1.13 ± 0.19
M_1 ($M_\odot$)	28.68 ± 15.29	13.17 ± 4.55
M_2 ($M_\odot$)	19.10 ± 5.60	11.62 ± 2.12
$\log(Z)$	-9029	-8788*

Lastly, we discussed the geometric properties of the disk and F-star as displayed in Table 5.2. The joint and disjoint solutions, bracket the 200 $R_\odot$ diameter for the

F-star derived by Pasinetti Fracassini et al. (2001) from application of binary star theory, although the underlying reference Plaut (1953) uses an older spectroscopic orbital solution. The opaque portion of disk has an aspect ratio of $\sim 12.3:1$.

Table 5.2: Disk and star parameters. *Note the disk diameter displayed here does not include the outer decay region.

	Model Values		Joint Solution		Disjoint Solution	
F-Star Radius	1.154 ± 0.0435	*mas*	223.15 ± 9.01	$R_\odot$	182.94 ± 18.00	$R_\odot$
LDD_α	0.673 ± 0.257		...		...	
H_{disk}	0.801 ± 0.037	*mas*	0.72 ± 0.03	AU	0.59 ± 0.06	AU
D_{disk}*	9.920 ± 0.025	*mas*	8.92 ± 0.13	AU	7.31 ± 0.66	AU
β_{disk}	$1.44 - 1.78$		...		...	

5.2 Future prospects

Although this work represents a considerable improvement in our understanding of ϵ Aurigae, there are still several studies that should be conducted. We divide our comments in terms of observational method.

On the astrometric front we suggest two courses of action. First, the F-star's orbital semi-major axis, α_1, can be determined in an independent method from above, providing a check on our results. Because the linear semi-major axis, a_1 is known to an accuracy of 1%, an accurate estimate for the system's parallax could be used to derive the angular orbital semi-major axis, α_1. The Fine Guidance Sensors on the Hubble Space Telescope, for example, are ideally suited for this work.

Even if a new parallax is obtained, we highly recommend the preservation and eventual digitization of the ϵ Aurigae plates at the Sproul and Yerkes observatories. Not only would these plates provide additional reference stars against which plate solutions could be computed, but they would also significantly expand the orbital

coverage of to 57 years (2.1 orbits). With the next generation of astrometric satellite, GAIA, set to launch in 2013, the improved positions, proper motions, and parallaxes for the reference stars could considerably improve upon the astrometric solution for ϵ Aurigae.

Photometry on this system will likely provide an excellent test case for any asteroseismic theory of evolved stellar objects that is developed in the coming years. Because of this, and our predictions in Chapter 2, we highly suggest this system be monitored over the long-term in at least UBV filters and, if possible, J- and H-bands. These data could become very important if the α Cyg nature of the F-star is to be tested interferometrically.

Additional photometric model fitting should be undertaken. When the F-star exhibits stable variations, they are not smooth, but instead have sharply defined peaks. Therefore we suggest the WWZ experiment described herein be repeated using a sawtooth-like wavelet rather than sinusoids. We also think that a new photometric disk model with wavelength-dependent extinction should be implemented to determine the size of the particles responsible for the additional absorption observed during the second half of the eclipse.

As interferometry has been a primary focus of my efforts, I have several suggestions on how this work could be improved. Foremost, more advanced models for the F-star and disk should be implemented and tested. As discussed in Chapter 3, we believe the minimizer "fuzzes" out the F-star to compensate for the hard edge of the current disk model. Any future modeling of this object needs to include a disk model with radially- and height-dependent opacity.

Any future interferometric modeling of the system should also include photometry as an additional constraint. Combined photometric and intererometric modeling can provide information on features below the formal resolution of the interferometer. Along with this, we suggest a non-radial pulsation model be implemented and

tested on the out-of-eclipse ϵ Aurigae data because our models show additional non-zero closure phase that remain after our limb-darkened models have been applied.

CHARA was not the only interferometer to observe the 2009-2011 eclipse of ϵ Aurigae. The Navy Optical Interferometer (NOI) also captured several epochs before the eclipse and during ingress. These optical data may reveal additional, wavelength-dependent features not captured in the H-band CHARA-MIRC data.

I suggest the polarimetric results from Kemp et al. (1986) should be revisited. Their model for the eclipse implies that (1) the orbital plane nearly bisects the F-star and that (2) the disk is tilted with respect to the orbital plane. The interferometric images and modeling disagree entirely with these claims. If someone were to undertake this project, the broadband UBV polarimetry data are readily available in Henson (1989).

Lastly, the Brackett α line at 4.05 μm is in emission (see Backman et al. 1985, Stencel et al. 2011). This is abnormal for an F-type supergiant. Given that the disk appears to show an emission spectrum in other hydrogen lines (Stencel et al. 2011), this may be a strong recombination line assoicated with the disk. If observed at sufficient resolution, this line may serve as a tracer for the orbital motion of the disk! With only a few data points, the orbital semi-amplitude, K_2 for the disk could be obtained. This may provide a significantly better estimate for the mass ratio then the work contained herein thereby further constraining the evolutionary scenario for the system.

Bibliography

Aerts, C., Christensen-Dalsgaard, J., and Kurtz, D. W. (2010). Asteroseismology. *Asteroseismology by C. Aerts*.

Albo, H. (1977). UBV photometry of epsilon Aurigae. *Publ. Tartu Astrofiz. Obs.*

Albo, H. and Sorgsepp, L. (1974). Photoelectric observations of epsilon Aurigae out of eclipses. *Tartu Astrofüüs. Obs. Publ.*

Arellano Ferro, A. (1985). Periodicity and pulsational mode of five bright yellow supergiants. *Royal Astronomical Society*, 216:571–587.

Armitage, P. (2010). *Astrophysics of Planet Formation*. Cambridge University Press, Cambridge, UK.

Backman, D. E., Becklin, E. E., Cruikshank, D. P., Joyce, R. R., Simon, T., and Tokunaga, A. (1984). Infrared observations of the eclipse of Epsilon Aurigae Direct measurement of the 500 K secondary at 5, 10, and 20 microns. *The Astrophysical Journal*, 284:799.

Backman, D. E., Simon, T., and Hinkle, K. H. (1985). Emission in the hydrogen-Brackett lines of Epsilon Aurigae during eclipse. *Publications of the Astronomical Society of the Pacific*, 97:1163.

Baron, F. and Kloppenborg, B. (2010). GPU-accelerated image reconstruction for

optical and infrared interferometry. In Danchi, W. C., Delplancke, F., and Rajagopal, J. K., editors, *Optical and Infrared Interferometry II*, volume 7734, pages 77344D–9, San Diego, California, USA. SPIE.

Baron, F., Monnier, J. D., and Kloppenborg, B. (2010). A novel image reconstruction software for optical/infrared interferometry. In Danchi, W. C., Delplancke, F., and Rajagopal, J. K., editors, *Optical and Infrared Interferometry II*, volume 7734, pages 77342I–8, San Diego, California, USA. SPIE.

Barsony, M., Mould, J. R., and Lutz, B. L. (1986). High-resolution spectroscopy of the unique eclipsing binary system - Epsilon Aurigae. *Publications of the Astronomical Society of the Pacific*, 98:637.

Berger, J. P., Malbet, F., Baron, F., Chiavassa, A., Duvert, G., Elitzur, M., Freytag, B., Gueth, F., Hönig, S., Hron, J., Jang-Condell, H., Bouquin, J. B. L., Monin, J. L., Monnier, J. D., Perrin, G., Plez, B., Ratzka, T., Renard, S., Stefl, S., Thiébaut, E., Tristram, K., Verhoelst, T., Wolf, S., and Young, J. (2012). Imaging the heart of astrophysical objects with optical long-baseline interferometry.

Bhatt, H. C., Ashok, N. M., and Chandrasekhar, T. (1984). Epsilon Aurigae: B V R I J H K Photometry. *Information Bulletin on Variable Stars*.

Billings, G. (2010). Rapid Cadence Monitoring of epsilon Aurigae. *Journal of the American Association of Variable Star Observers (JAAVSO)*, 38:142.

Blackwell, D. E. and Shallis, M. J. (1977). Stellar angular diameters from infrared photometry - Application to Arcturus and other stars; with effective temperatures. *Monthly Notices of the Royal Astronomical Society*, 180:177–191.

Bond, H. E. (1991). Chemical Composition of Post-Agb Stars. *Evolution of Stars: the Photospheric Abundance Connection*, 145:341.

Boyd, L. J., Genet, R. M., and Hall, D. S. (1984a). A Photometric Anomaly around Third Contact in epsilon Aurigae. *Information Bulletin on Variable Stars*.

Boyd, L. J., Genet, R. M., and Hall, D. S. (1984b). Automatic Photoelectric Telescope. *International Amateur-Professional Photoelectric Photometry Communication*.

Breger, M. (1982). IAU Archives of Unpublished Observations of Variable Stars. *Information Bulletin on Variable Stars*.

Breger, M. (1985). I.A.U. Archives of Unpublished Observations of Variable Stars - 1981-1984 Data. *Publications of the Astronomical Society of the Pacific*, 97:85.

Breger, M. (1988). IAU Archives of Unpublished Observations of Variable Stars: 1984-88 Data. *Publications of the Astronomical Society of the Pacific*, 100:751.

Brummelaar, T. (2012). CHARA Technical Report The CLASSIC / CLIMB Data Reduction Pipelines. *CHARA Technical Reports*, 96(96).

Budaj, J. (2011). Effects of dust on light-curves of Aurigae-type stars. *Astronomy & Astrophysics*, 532:L12.

Burns, K. (1932). Photographic Determinations of the Parallaxes of 70 Stars with the Thaw Refactor. *Publications of the Allegheny Observatory of the University of Pittsburgh ; v. 9*, 9:22–23.

Buscher, D. F. (1994). Direct maximum-entropy image reconstruction from the bispectrum. *Very high angular resolution imaging; Proceedings of the 158th International Astronomical Union (IAU) Symposium*.

Cameron, A. G. (1971a). Evidence for a collapsar in the binary system epsilon Aur. *Nature*, 229(5281):178–80.

Cameron, A. G. W. (1971b). Epsilon Aurigae-In support of the collapsar model. *Nature Physical Science*, 231.

Castelli, F. (1976). Fast Variations of epsilon Aurigae. *Information Bulletin on Variable Stars*, 1165:1.

Cha, G., Tan, H., Xu, J., and Li, Y. (1994). High-dispersion H alpha spectroscopy of epsilon Aurigae. *Astronomy and Astrophysics (ISSN 0004-6361)*, 284:874–882.

Chadima, P., Harmanec, P., Bennett, P. D., Kloppenborg, B., Stencel, R., Yang, S., Božić, H., Šlechta, M., Kotková, L., Wolf, M., Škoda, P., Votruba, V., Hopkins, J. L., Buil, C., and Sudar, D. (2011). Spectral and photometric analysis of the eclipsing binary Aurigae prior to and during the 20092011 eclipse. *Astronomy & Astrophysics*, 530:A146.

Chadima, P., Harmanec, P., Yang, S., Bennett, P. D., Bozic, H., Ruzdjak, D., Sudar, D., Skoda, P., Slechta, M., Wolf, M., Lehky, M., and Dubovsky, P. (2010). A new ephemeris and an orbital solution of epsilon Aurigae. *Information Bulletin on Variable Stars*, 5937:1.

Che, X., Monnier, J. D., and Webster, S. (2010). High precision interferometer: MIRC with photometric channels. In *Optical and Infrared Interferometry II. Edited by Danchi*, volume 7734, pages 77342V–77342V–9.

Chochol, D. and Žižovský, J. (1987). Photoelectric photometry of the eclipse of Epsilon Aurigae. *Contrib. Astron. Obs. Skalnaté Pleso*, 16.

Claret, A., Diaz-Cordoves, J., and Gimenez, A. (1995). Linear and non-linear limb-darkening coefficients for the photometric bands R I J H K. *Astronomy and Astrophysics Supplement.*

Colavita, M. M., Wallace, J. K., Hines, B. E., Gursel, Y., Malbet, F., Palmer, D. L., Pan, X. P., Shao, M., Yu, J. W., Boden, A. F., Dumont, P. J., Gubler, J., Koresko,

C. D., Kulkarni, S. R., Lane, B. F., Mobley, D. W., and van Belle, G. T. (1999). The Palomar Testbed Interferometer. *The Astrophysical Journal*, 510(1):505–521.

Cotton, W., Monnier, J., Baron, F., Hofmann, K.-H., Kraus, S., Weigelt, G., Rengaswamy, S., Thiebaut, E., Lawson, P., Jaffe, W., Hummel, C., Pauls, T., Schmitt, H., Tuthill, P., and Young, J. (2008). 2008 imaging beauty contest. In *Proceedings of SPIE*, volume 7013, pages 70131N–70131N–14. SPIE.

Cox, A. N. (2000). Allen's astrophysical quantities. *Allen's astrophysical quantities*.

Danjon, A. (1936). Observations photométriques de Aurigæ. *Journal des Observateurs*, 19.

Dubath, P., Rimoldini, L., Süveges, M., Blomme, J., López, M., Sarro, L. M., De Ridder, J., Cuypers, J., Guy, L., Lecoeur, I., Nienartowicz, K., Jan, A., Beck, M., Mowlavi, N., De Cat, P., Lebzelter, T., and Eyer, L. (2011). Random forest automated supervised classification of Hipparcos periodic variable stars. *Monthly Notices of the Royal Astronomical Society*, 414(3):2602–2617.

Eggleton, P. P. and Pringle, J. E. (1985). Possible evolution of a triple system into Epsilon Aurigae. *The Astrophysical Journal*, 288:275.

Eichhorn, H. (1974). *Astronomy of star positions - A critical investigation of star catalogues, the methods of their construction and their purpose.*

El Eid, M. F. and Champagne, A. E. (1995). Sodium Enrichment in A–F Type Supergiants. *The Astrophysical Journal*, 451:298.

Emberson, R. M., Lovinger, R., and Sterne, T. E. (1938). The Radiometric Magnitude of Epsilon Aurigae. *Harvard College Observatory Bulletin No. 908.*

Ferluga, S. (1990). Epsilon Aurigae. I - Multi-ring structure of the eclipsing body. *Astronomy and Astrophysics (ISSN 0004-6361)*, 238:270–278.

Feroz, F. and Hobson, M. P. (2008). Multimodal nested sampling: an efficient and robust alternative to Markov Chain Monte Carlo methods for astronomical data analyses. *Monthly Notices of the Royal Astronomical Society*, 384(2):449–463.

Feroz, F., Hobson, M. P., and Bridges, M. (2009). MultiNest: an efficient and robust Bayesian inference tool for cosmology and particle physics. *Monthly Notices of the Royal Astronomical Society*, 398(4):1601–1614.

Finsen, W. S. and Worley, C. E. (1970). Third catalogue of orbits of visual binary stars. *Republic Obs. Johannesburg Circ.*, 7.

Flin, P., Winiarski, M., and Zola, S. (1985). Photoelectric Photometry of epsilon Aurigae. *Information Bulletin on Variable Stars*.

Foster, G. (1996). Wavelets for period analysis of unevenly sampled time series. *The Astronomical Journal*, 112:1709.

Fredrick, L. W. (1960). Observations of epsilon Aurigae. *The Astronomical Journal*, 65:97.

Fritsch, J. M. (1824). No Title. *Astronomisches Jahrbuch*, page 252.

Glindemann, A. (2011). *Principles of Stellar Interferometry*. Astronomy and Astrophysics Library. Springer Berlin Heidelberg, Berlin, Heidelberg.

Gregory, P. C. (2007). A Bayesian Kepler periodogram detects a second planet in HD208487. *Monthly Notices of the Royal Astronomical Society*, 374(4):1321–1333.

Güssow, M. (1928). Aurigae. *Astronomische Nachrichten*, 232.

Güssow, M. (1933). Über die sekundären Schwankungen im Lichtwechsel von Aurigae. *Astronomische Nachrichten*, 250.

Güssow, M. (1936). Epsilon Auriage. *Veröffentlichungen Der Universitätssternwarte zu Berlin-Babelsberg*, 11(3):3–36.

Hall, D. S. and Henry, G. W. (1992). Performance Evaluation of Two Automatic Telescopes After Eight Years. *Automated Telescopes for Photometry and Imaging*, 28.

Hall, D. S., Kirkpatrick, J. D., and Seufert, E. R. (1986). The First Two Years of APT Data: Performance and Accuracy. *International Amateur-Professional Photoelectric Photometry Communication*.

Handbury, M. J. and Williams, I. P. (1976). The peculiar binary system epsilon Aurigae. *Astrophysics and Space Science*, 45(2):439–446.

Hansen, C. J., Kawaler, S. D., and Trimble, V. (2004). Stellar interiors : physical principles, structure, and evolution. *Stellar interiors : physical principles*.

Hartkopf, W. I. and McAlister, H. A. (1984). Binary stars unresolved by speckle interferometry. III. *Publications of the Astronomical Society of the Pacific*, 96:105.

Heintz, W. D. and Cantor, B. A. (1994). An astrometric study of four binary stars. *Publications of the Astronomical Society of the Pacific*, 106:363.

Henson, G. D. (1989). *Observation and analysis of variable linear polarization in the yellow supergiant star Epsilon Aurigae*. PhD thesis.

Hershey, J. L. (1973). Astrometric analysis of the field of AC +65 6955 from plates taken with the Sproul 24-inch refractor. *The Astronomical Journal*, 78:421.

Hestroffer, D. (1997). Centre to limb darkening of stars. New model and application to stellar interferometry. *Astronomy and Astrophysics*.

Hinkle, K. H. and Simon, T. (1987). Two micron CO absorption lines in the spectrum of Epsilon Aurigae during eclipse. *The Astrophysical Journal*, 315:296.

Høg, E., Fabricius, C., Makarov, V. V., Urban, S., Corbin, T., Wycoff, G., Bastian, U., Schwekendiek, P., Wicenec, A., Høg,E., Fabricius,C., Makarov,V.V., Urban,S., Corbin,T., Wycoff,G., Bastian,U., Schwekendiek,P., Wicenec,A., Hø g, E., Fabricius, C., Makarov, V. V., Urban, S., Corbin, T., Wycoff, G., Bastian, U., Schwekendiek, P., and Wicenec, A. (2000). (Erratum) Letter to the Editor - The Tycho-2 catalogue of the 2.5 million brightest stars. *Astronomy and Astrophysics*, 363.

Hoard, D. W., Howell, S. B., and Stencel, R. E. (2010). Taming the Invisible Monster: System Parameter Constraints for Aurigae From the Far-Ultraviolet To the Mid-Infrared. *The Astrophysical Journal*, 714(1):549–560.

Hoard, D. W., Ladjal, D., Stencel, R., and Howell, S. (2012). The Invisible Monster Has Two Faces: Observations of Aurigae with the Herschel Space Observatory. *The Astrophysical Journal Letters*, 748(2):L28.

Hopkins, J. L. (1985). Optical photometry of the 1982-1984 eclipse of Epsilon Aurigae. *In NASA*.

Hopkins, J. L. and Stencel, R. E. (2008). *Epsilon Auriage: A Mysterious Star System*. Hopkins Phoenix Observatory, Phoenix, AZ, 1 edition.

Hrivnak, B. J., Lu, W., Maupin, R. E., and Spitzbart, B. D. (2010). VARIABILITY IN PROTO-PLANETARY NEBULAE. I. LIGHT CURVE STUDIES OF 12 CARBON-RICH OBJECTS. *The Astrophysical Journal*, 709(2):1042–1066.

Huang, S.-S. (1965). An Interpretation of Aurigae. *The Astrophysical Journal*, 141:976.

Huang, S.-S. (1974). Interpretation of Epsilon Aurigae. 11. Infrared Excess, Secondary Light Variations, and Plausible Formation of a Planetary System. *The Astrophysical Journal*, 187:87.

Huffer, C. M. (1932). A Photo-Electric Study of ϵ Aurigae. *The Astrophysical Journal*, 76:1.

Husar, D. (2006). Peranso: Period Analysis Software. *BAV Rundbrief*.

Iben, I. (1967). Stellar Evolution within and off the Main Sequence. *Annual Review of Astronomy and Astrophysics*, 5(1):571–626.

Iben, I. (1991). Single and binary star evolution. *The Astrophysical Journal Supplement Series*, 76:55.

Iben, I. (1995). Planetary nebulae and their central stars - origin and evolution. *Phys. Rep.*, 250.

Iben, I. and Livio, M. (1993). Common envelopes in binary star evolution. *Publications of the Astronomical Society of the Pacific*, 105:1373.

Ireland, M. J. (2006). Monte-Carlo imaging for optical interferometry. In *Proceedings of SPIE*, volume 6268, pages 62681T–62681T–8. SPIE.

Isobe, S. (1991). Speckle observations of spectroscopic binaries. *Proceedings of the Astronomical Society of Australia*, 9:270–272.

Isobe, S., Norimoto, Y., Noguchi, M., Ohtsubo, J., and Baba, N. (1990). Speckle observations of visual and spectroscopic binaries. II. *Publications of the National Astronomical Observatory of Japan*, 1:381–392.

IUA SOFA Board (2010). IAU SOFA Software Collection.

Ivanov, N. and Scharbe, S. B. (1934). Observations of Variable Stars. I. Auriage. *Astronomische Nachrichten*, 251.

Japan Amateur Photoelectric Observers Association (1983). Photoelectric Observations of epsilon Aurigae during the Ingress. *Information Bulletin on Variable Stars*.

Jennison, R. (1958). A phase sensitive interferometer technique for the measurement of the Fourier transforms of spatial brightness distributions of small angular extent. *Monthly Notices of the Royal Astronomical Society*, 118.

Kemp, J. C., Henson, G. D., Kraus, D. J., Beardsley, I. S., Carroll, L. C., Ake, T. B., Simon, T., and Collins, G. W. (1986). Epsilon Aurigae - Polarization, light curves, and geometry of the 1982-1984 eclipse. *The Astrophysical Journal*, 300:L11.

Kim, H. (2008). PERIOD ANALYSIS FOR THE F COMPONENT OF THE AURIGAE SYSTEM USING WAVELETS. *Journal of Astronomy and Space Sciences*, 25(1):1–18.

Kloppenborg, B., Stencel, R., Monnier, J. D., Schaefer, G., Zhao, M., Baron, F., McAlister, H., Ten Brummelaar, T., Che, X., Farrington, C., Pedretti, E., Sallave-Goldfinger, P. J., Sturmann, J., Sturmann, L., Thureau, N., Turner, N., and Carroll, S. M. (2010). Infrared images of the transiting disk in the epsilon Aurigae system. *Nature*, 464(7290):870–2.

Kloppenborg, B. K., Stencel, R., Monnier, J. D., Schaefer, G., Zhao, M., Baron, F., McAlister, H., ten Brummelaar, T., Che, X., Farrington, C., Pedretti, E., Sallave-Goldfinger, P., Sturmann, J., Sturmann, L., Thureau, N., Turner, N., and Carroll, S. (2011). Interferometric Images Of The Transiting Disk In The Epsilon Aurigae System. In *American Astronomical Society*, volume 43.

Kopal, Z. (1954). The nature of the eclipses of epsilon Aurigae. *The Observatory*, 74:14–20.

Kopal, Z. (1971). The eclipsing system of epsilon Aurigae and its possible relevance to the formation of a planetary system. *Astrophysics and Space Science*, 10(2):332–339.

Kopylov, I. and Kumaigorodskaya, R. (1963). A Spectrophotometric Study of epsilon Auriage during the 1955-1957 eclipse. *Proceedings of the Crimean Astrophysical Observatory*, XXIX:251–266.

Kraft, R. P. (1954). The Atmosphere of the i Component of Epsilon Aurigae. *The Astrophysical Journal*, 120:391.

Kuiper, G. P., Struve, O., Strömgren, B., and Kuiper, G.P.; Struve, O. Stromgren, B. (1937). The Interpretation of ϵ Aurigae. *The Astrophysical Journal*, 86:570.

Labeyrie, A., Lipson, S. G., and Nisenson, P. (2006). *An Introduction to Optical Stellar Interferometry*. Cambridge University Press, Cambridge.

Lafrasse, S., Mella, G., Bonneau, D., Duvert, G., Delfosse, X., and Chelli, A. (2010). JMMC Stellar Diameters Catalogue - JSDC (Lafrasse+, 2010). *VizieR On-line Data Catalog: II/300. Originally published in: 2010SPIE.7734E.140L.*

Lambert, D. L. and Sawyer, S. R. (1986). Epsilon Aurigae in eclipse. II - Optical absorption lines from the secondary. *Publications of the Astronomical Society of the Pacific*, 98:389.

Larsson-Leander, G. (1959). Photoelectric observations of the 1955-1957 eclipse of Epsilon Aurigae. *Arkiv för Astronomii*, 2.

Larsson-Leander, G. (1962). Photoelectric observations of Epsilon Aurigae out of eclipse. *Arkiv för Astronomii*, 3.

Lawson, P. R. (2000). Principles of Long Baseline Stellar Interferometry. *Principles of Long Baseline Stellar Interferometry*, -1.

Lawson, P. R. (2006). 2006 interferometry imaging beauty contest. In *Proceedings of SPIE*, volume 6268, pages 62681U–62681U–12. SPIE.

Lawson, P. R., Cotton, W. D., Hummel, C. A., Monnier, J. D., Zhao, M., Young, J. S., Thorsteinsson, H., Meimon, S. C., Mugnier, L., Le Besnerais, G., Thiebaut, E., and Tuthill, P. G. (2004a). The 2004 Optical/IR Interferometry Imaging Beauty Contest. *American Astronomical Society Meeting 205*, 36.

Lawson, P. R., Cotton, W. D., Hummel, C. A., Monnier, J. D., Zhao, M., Young, J. S., Thorsteinsson, H., Meimon, S. C., Mugnier, L. M., Le Besnerais, G., Thiebaut, E. M., and Tuthill, P. G. (2004b). An interferometry imaging beauty contest. *New Frontiers in Stellar Interferometry*, 5491.

Lippincott, S. L. (1957). Accuracy of positions and parallaxes. *The Astronomical Journal*, 62:55.

Lourakis, M. I. A. (2005). levmar: Levenberg-Marquardt non-linear least squares algorithms in C/C++. [web page] \verb+http://www.ics.forth.gr/~lourakis/levmar/+.

Low, F. J. and Mitchell, R. I. (1965). New Infrared Photometry of Aurigae. *The Astrophysical Journal*, 141:327.

Ludendorff, H. (1903). Untersuchungen über den Lichtwechsel von ϵ Aurigae. *Astronomische Nachrichten*, 164(6-8):81–114.

Ludendorff, H. (1912). Bearbeitung derSchmidtschen Beobachtungen des Veränderlichen Aurigae. *Astronomische Nachrichten*, 192(22):389–406.

Ludendorff, H. (1924). Über die Radialgeschwindigket von epsilon Auriage. *Sitzungsber. der. Preuss. Akad. der Wissensch.*, pages 49–69.

Maeder, A. (1980). Supergiant variability - Amplitudes and pulsation constants in relation with mass loss and convection. *Astronomy and Astrophysics*, 90:311–317.

McAlister, H. A. (1976). Spectroscopic binaries as a source for astrometric and speckle interferometric studies. *Publications of the Astronomical Society of the Pacific*, 88:317.

McAlister, H. A. (1978). Binary stars unresolved by speckle interferometry. *Publications of the Astronomical Society of the Pacific*, 90:288.

Mitchell, R. I. (1964). Nine-Color Photometry of AUR, 0.35-9.5 μ. *The Astrophysical Journal*, 140:1607.

Mitchell, S. A., Reuyl, D., and al., E. (1940). The Trignometric Parallaxes of 650 Stars Determined by Photography with the 26-inch Visual Refractor of the Leander McCormick Observatory. *Publications of the Leander McCormick Observatory*, 8.

Monnier, J. (2007). Phases in interferometry. *New Astronomy Reviews*, 51(8-9):604–616.

Monnier, J. D. (2006). Michigan Infrared Combiner (MIRC): commissioning results at the CHARA Array. In *Proceedings of SPIE*, volume 6268, pages 62681P–62681P–11. SPIE.

Monnier, J. D., Anderson, M., Baron, F., Berger, D. H., Che, X., Eckhause, T., Kraus, S., Pedretti, E., Thureau, N., Millan-Gabet, R., ten Brummelaar, T., Irwin, P., and Zhao, M. (2010). MI-6: Michigan interferometry with six telescopes. In *Optical and Infrared Interferometry II. Edited by Danchi*, volume 7734, pages 77340G–77340G–12.

Monnier, J. D., Berger, J.-P., Millan-Gabet, R., and ten Brummelaar, T. A. (2004). The Michigan Infrared Combiner (MIRC): IR imaging with the CHARA Array. *New Frontiers in Stellar Interferometry*, 5491.

Monnier, J. D., Zhao, M., Pedretti, E., Thureau, N., Ireland, M., Muirhead, P., Berger, J.-P., Millan-Gabet, R., Van Belle, G., Ten Brummelaar, T., McAlister, H., Ridgway, S., Turner, N., Sturmann, L., Sturmann, J., and Berger, D. (2007). Imaging the surface of Altair. *Science (New York, N.Y.)*, 317(5836):342–5.

Morgan, W. W., Code, A. D., and Whitford, A. E. (1955). Studies in Galactic STRUCTURE.II.LUMINOSITY Classification for 1270 Blue Giant Stars. *The Astrophysical Journal Supplement Series*, 2:41.

Morris, S. C. (1962). R.A.S.C. Papers- The Spectroscopic Orbit of Epsilon Aurigae:. *Journal of the Royal Astronomical Society of Canada*, 56.

Mozurkewich, D., Armstrong, J. T., Hindsley, R. B., Quirrenbach, A., Hummel, C. A., Hutter, D. J., Johnston, K. J., Hajian, A. R., Elias II, N. M., Buscher, D. F., and Simon, R. S. (2003). Angular Diameters of Stars from the Mark III Optical Interferometer. *The Astronomical Journal*, 126(5):2502–2520.

Münch, G. (1957). Interstellar Absorption Lines in Distant Stars. I. Northern Milky way. *The Astrophysical Journal*, 125:42.

Nha, I. S. and Lee, S. J. (1983). Flare Activity of epsilon Aurigae? *Information Bulletin on Variable Stars*.

Nha, I. S., Lee, Y. S., Jeong, J. H., and Kim, H. I. (1993). Extreme Long-period Eclipsing Binary EPS Aurigae. *New frontiers in binary star research : a colloquium sponsored by the U.S. National Science Foundation and the Korean Science and Engineering Foundation*.

Nordgren, T. E., Sudol, J. J., and Mozurkewich, D. (2001). Comparison of Stellar Angular Diameters from the NPOI, the Mark III Optical Interferometer, and the Infrared Flux Method. *The Astronomical Journal*, 122(5):2707–2712.

Pan, X., Shao, M., and Colavita, M. M. (1994). High resolution interferometric observations of eclipsing binary stars. *Very high angular resolution imaging; Proceedings of the 158th International Astronomical Union (IAU) Symposium.*

Parthasarathy, M. and Frueh, M. L. (1986). Epsilon Aurigae in eclipse: The light and colour variations. *Astrophysics and Space Science*, 123(1):31–48.

Pasinetti Fracassini, L. E., Pastori, L., Covino, S., and Pozzi, A. (2001). Catalogue of Apparent Diameters and Absolute Radii of Stars (CADARS) - Third edition -Comments and statistics. *Astronomy and Astrophysics*, 367(2):521–524.

Pauls, T. A., Young, J. S., Cotton, W. D., and Monnier, J. D. (2005). A Data Exchange Standard for Optical (Visible/IR) Interferometry. *Publications of the Astronomical Society of the Pacific*, 117(837):1255–1262.

Plaut, L. (1953). An Investigation of the Eclipsing Binaries Brighter than Photographic Magnitude 8.50 at Maximum. *Publications of the Kapteyn Astronomical Laboratory Groningen*, 55.

Renard, S., Thiébaut, E., and Malbet, F. (2011). Image reconstruction in optical interferometry: benchmarking the regularization. *Astronomy & Astrophysics*, 533:A64.

Röser, S., Schilbach, E., Schwan, H., Kharchenko, N. V., Piskunov, A. E., and Scholz, R.-D. (2008). PPM-Extended (PPMX) a catalogue of positions and proper motions. *Astronomy and Astrophysics*, 488(1):401–408.

Roy, A. E. (2005). Orbital motion. *Orbital motion / A. E. Roy. Bristol (UK): Institute of Physics Publishing.*

Russell, H. N. (1912a). On the Determination of the Orbital Elements of Eclipsing Variable Stars. I. *The Astrophysical Journal*, 35:315.

Russell, H. N. (1912b). On the Determination of the Orbital Elements of Eclipsing Variable Stars. II. *The Astrophysical Journal*, 36:54.

Sadakane, D., Kambe, E., Sato, B., Honda, S., and Hashimoto, O. (2010). An Abundance Analysis of the Primary Star of the Peculiar Eclipsing Binary Aurigae out of the Eclipsing Phase. *Publications of the Astronomical Society of Japan*, 62:1381–1390.

Saitō, M. and Kitamura, M. (1986). Possible shrinking of the primary component of epsilon aurigae. *Astrophysics and Space Science*, 122(2):387–393.

Saselov, D. D. (1986). Normal supergiants and their imitations. I - Sodium as a mass indicator? *Publications of the Astronomical Society of the Pacific*, 98:561.

Schanne, L. (2007). Remarkable Absorption Strength Variability of the epsilon Aurigae Halpha Line outside Eclipse. *Information Bulletin on Variable Stars*, 5747:1.

Schmidtke, P. C. (1985). UBV photometry of the 1982 - 4 eclipse of Epsilon Aurigae - a discussion of the observed light curves. *NASA Conf. Publ.*

Schoenberg, E. and Jung, B. (1938). Über die Deutung der Lichtkurve von Aurigae. *Astronomische Nachrichten*, 265.

Shao, M., Colavita, M. M., Hines, B. E., Staelin, D. H., Hutter, D. J., Johnston, K. J., Mozurkewich, D., Simon, R. S., Hershey, J. L., Hughes, J. A., and Kaplan, G. H. (1988). The Mark III stellar interferometer. *Astronomy and Astrophysics (ISSN 0004-6361)*, 193:357–371.

Shapley, H. (1915). A Study of the Orbits of Eclipsing Binaries. *Contributions from the Princeton University Observatory*, 3.

Shapley, H. (1928). On the Variability of the Maximum Light of Epsilon Aurigae. *Harvard College Observatory Bulletin No. 858*.

Simnett, G. M., Eyles, C. J., Cooke, M. P., Waltham, N. R., King, J. M., Jackson, B. V., Buffington, A., Hick, P. P., Holladay, P. E., and Anderson, P. A. (2003). The Solar Mass Ejection Imager (SMEI). *American Geophysical Union*, (2):319–347.

Smith, R. L., Pontoppidan, K. M., Young, E. D., and Morris, M. R. (2010). Observations of High 12CO/13CO Toward Protostars and Implications for the Origin of the 12C/13C Ratio in the Solar System. *Lunar and Planetary Institute Science Conference Abstracts*, 41:2254.

Stefanik, R. P., Torres, G., Lovegrove, J., Pera, V. E., Latham, D. W., Zajac, J., and Mazeh, T. (2010). EPSILON AURIGAE: AN IMPROVED SPECTROSCOPIC ORBITAL SOLUTION. *The Astronomical Journal*, 139(3):1254–1260.

Stencel, R. E. (1985). 1982 - 1984 eclipse of Epsilon Aurigae. Summary of a working meeting held in Tucson, Arizona, 16 - 17 January 1985. *1982 - 1984 eclipse of Epsilon Aurigae. Summary of a working meeting held in Tucson.*

Stencel, R. E. (2007). Evidence for a Precessing Disk in the Extreme Binary Aurigae. *Proceedings of the International Astronomical Union*, 2(S240).

Stencel, R. E., Creech-Eakman, M., Hart, A., Hopkins, J. L., Kloppenborg, B. K., and Mais, D. E. (2008). Interferometric Studies of the Extreme Binary Aurigae: Pre-Eclipse Observations. *The Astrophysical Journal*, 689(2):L137–L140.

Stencel, R. E., Kloppenborg, B. K., Wall, R. E., Hopkins, J. L., Howell, S. B., Hoard, D. W., Rayner, J., Bus, S., Tokunaga, A., Sitko, M. L., Bradford, S., Russell, R. W., Lynch, D. K., Hammel, H., Whitney, B., Orton, G., Yanamandra-Fisher, P., Hora, J. L., Hinz, P., Hoffmann, W., and Skemer, A. (2011). INFRARED

STUDIES OF EPSILON AURIGAE IN ECLIPSE. *The Astronomical Journal*, 142(5):174.

Strand, K. A. (1959). The astrometric orbit of Epsilon Aurigae. *The Astronomical Journal*, 64:346.

Strassmeier, K. G. and Hall, D. S. (1988). Photometric variability in chromospherically active stars. I - The constant stars. *The Astrophysical Journal Supplement Series*, 67:439.

Strassmeier, K. G., Serkowitsch, E., and Granzer, T. (1999). Starspot photometry with robotic telescopes. UBV(RI) C and by light curves of 47 active stars in 1996/97. *Astronomy and Astrophysics Supplement Series*, 140(1):29–53.

Struve, O., Pillans, H., and Zebergs, V. (1958). The Radial Velocity of Epsilon Aurigae. *The Astrophysical Journal*, 128:287.

Stub, H. (1972). Secondary fluctuations in the light curve of epsilon Aur. *Astron. Astrophys.*, 20:161–162.

Sturmann, J., ten Brummelaar, T., Sturmann, L., and McAlister, H. A. (2010). Dual three-way infrared beam combiner at the CHARA Array. In *Optical and Infrared Interferometry II. Edited by Danchi*, volume 7734, pages 77343A–77343A–10.

Takeda, Y., Taguchi, H., Yoshioka, K., Hashimoto, O., Aikawa, T., and Kawanomoto, S. (2007). Abundances of Volatile Elements in Post-AGB Candidates. *Publications of the Astronomical Society of Japan*, 59:1127.

Takeuti, M. (1986). An accretion disc surrounding a component of epsilon aurigae. *Astrophysics and Space Science*, 121(1):127–135.

Takeuti, M. (2011). Effect of Irradiation on the Disk of the Epsilon Aurigae System. *Publications of the Astronomical Society of Japan*.

Tallon-Bosc, I., Tallon, M., Thiebaut, E., Bechet, C., Mella, G., Lafrasse, S., Chesneau, O., Domiciano de Souza, A., Duvert, G., Mourard, D., Petrov, R., and Vannier, M. (2008). LITpro: a model fitting software for optical interferometry. In *Proceedings of SPIE*, volume 7013, pages 70131J–70131J–9. SPIE.

Taranova, O. G. and Shenavrin, V. I. (2001). Infrared photometry of five long-period binaries. *Astronomy Letters*, 27(5):338–344.

ten Brummelaar, T. A., McAlister, H. A., Ridgway, S. T., Bagnuolo, J., Turner, N. H., Sturmann, L., Sturmann, J., Berger, D. H., Ogden, C. E., Cadman, R., Hartkopf, W. I., Hopper, C. H., and Shure, M. A. (2005). First Results from the CHARA Array. II. A Description of the Instrument. *The Astrophysical Journal*, 628(1):453–465.

Thiessen, G. (1957). Farbschwankungen des Systems Epsilon Aurigae. Mit 1 Textabbildungen. *Zeitschrift für Astrophysik*, 43.

van Belle, G. T., van Belle, G., CreechEakman, M. J., Coyne, J., Boden, A. F., Akeson, R. L., Ciardi, D. R., Rykoski, K. M., Thompson, R. R., Lane, B. F., and Collaboration, T. P. (2008). The Palomar Testbed Interferometer Calibrator Catalog. *The Astrophysical Journal Supplement Series*, 176(1):276–292.

van de Kamp, P. (1978). *Astrometric study of the eclipsing binary Epsilon Aurigae from plates taken with the Sproul 61-cm refractor*, volume 83. Cambridge University Press.

van de Kamp, P. (1981). *Stellar paths: Photographic astrometry with long-focus instruments*, volume 85. Dordrecht, D. Reidel Publishing Co, London, England, 1 edition.

van Leeuwen, F. (2007). Validation of the new Hipparcos reduction. *Astronomy and Astrophysics*, 474(2):653–664.

van Leeuwen, F., van Genderen, A. M., and Zegelaar, I. (1998). Hipparcos photometry of 24 variable massive stars (alpha Cygni variables). *Astronomy and Astrophysics Supplement Series*, 128(1):117–129.

Van Winckel, H. (2003). POST-AGB STARS. *Annual Review of Astronomy and Astrophysics*, 41(1):391–427.

Wendell, O. C. (1909). Photometric observations made with the fifteen inch east equatorial during the years 1892 to 1902. *Annals of Harvard College Observatory*, 69.

Wendell, O. C. (1913). Photometric observations made with the fifteen inch east equatorial during the years 1903 to 1912. *Annals of Harvard College Observatory*, 69.

Widorn, T. (1959). Lichtelektrische Beobachtungen von Epsilon und Eta Aurigae. *Mitt. Univ. Sternw. Wien.*

Wilson, R. E. (1971). A Model of Epsilon Aurigae. *The Astrophysical Journal*, 170:529.

Wolk, S. J., Pillitteri, I., Guinan, E., and Stencel, R. (2010). XMM-NEWTON OBSERVATIONS OF THE ENIGMATIC LONG PERIOD ECLIPSING BINARY EPSILON AURIGÆ: CONSTRAINING THE PHYSICAL MODELS. *The Astronomical Journal*, 140(2):595–601.

Wood, F. B. and Blitzstein, W. (1957). Observations of ZET AUR in the 1955-56 eclipse. *The Astronomical Journal*, 62:165.

Worley, C. E. and Heintz, W. D. (1983). Fourth catalog of orbits of visual binary stars. *Publications of the United States Naval Observatory ; 2nd ser.*

Wright, K. (1970). The Zeta Aurigae stars. *Vistas in Astronomy*, 12(1):147–182.